8-2019

Microextrusion 3D Printing of Optical Waveguides and Microheaters

Edidiong Nseowo Udofia
University of Arkansas, Fayetteville

Microextrusion 3D Printing of Optical Waveguides and Microheaters

A dissertation submitted in partial fulfillment
of the requirements for the degree of
Doctor of Philosophy in Mechanical Engineering

by

Edidiong Nseowo Udofia
University of Uyo
Bachelor of Engineering in Mechanical Engineering

August 2019
University of Arkansas

This dissertation is approved for recommendation to the Graduate Council.

_____
Wenchao Zhou, PhD
Dissertation Director

_____
Steve Tung, PhD
Committee Member

_____
James H. Leylek, PhD
Committee Member

_____
Uchechukwu C. Wejinya, PhD
Committee Member

_____
Hanna K. Jensen, PhD
Committee Member

ABSTRACT

The drive for smaller and more compact devices presents several challenges in materials and fabrication strategies. Although photolithography is a well-developed method for creating microdevices, the disparate requirements in fabrication strategies, material choices, equipment and process complexities have limited its applications. Microextrusion printing (μEP) provides a promising alternative for microfabrication. Compared to the traditional techniques, the attractions lie in the wide range of printable material choice, greater design freedom, fewer processing steps, lower cost for customized production, and the plurality of compatible substrates. However, while extrusion-based 3D printing processes have been successfully applied at the macroscale, this seeming simplicity belies the dynamic complexities needed for consistent, repeatable, and cost-effective printing at the microscale. The fundamental understanding of the microextrusion printing process is still lacking.

One primary goal of this dissertation, therefore, is to develop the fundamental understanding of μEP. This study elucidates the underlying principles of this printing technique, offering an overall roadmap - stepwise guide for successful printing based on both results in the literature and our experimental tests. The primary motivation is to provide users at both the research and industrial platforms with the requisite knowledge base needed for adapting μEP for microfabrication. Ultimately, this understanding, optimization of materials properties, and process parameters dictate the resolution and quality of the printed features.

Following the improved understanding of microextrusion printing, two complementary goals were set. First, in order to test and validate the applicability the framework, a high-resolution microextrusion 3D printer was designed and implemented to enable high precision printing of microdevices and microstructures. Second, taking advantage of the guiding framework and

printing platform, printing of novel materials and devices including flexible optics and a high-temperature microheater were explored and demonstrated. One common thread is observed throughout this work, that is, the development of the fundamental understanding of microextrusion 3D printing and its application for creating functional microdevices and structures. This work opens new possibilities and versatile approach for low-cost patterning of materials and functional devices.

ACKNOWLEDGMENTS

Great innovations are never accomplished in isolation. I am indebted to many people for their support toward the realization of this level of success. Time and space will fail me to mention everyone who has contributed (either directly or indirectly) to the accomplishment of this project. So, whether you are mentioned here or not, know this for sure, I will forever be grateful for your help and encouragement.

First, I am thankful to my research advisor, Dr. Wenchao Zhou for his financial support and offering me this unique opportunity (especially as his first Ph.D. student) to mature as a researcher and introducing me to the amazing field of additive manufacturing. These four years at AM^3 Lab has been a journey with many lessons. He has been very patient with me, providing positive criticism, suggestions, and timely feedback, no matter the hour of the day. His sense of dedication to excellence and undaunted scientific curiosity has and will always remain a constant source of inspiration. Thank you, Dr. Zhou.

Gratitude is owed to the array of excellent teachers I've had at various levels of my life. For their mentorship, support, and friendship I say, thank you.

I am heartily thankful to members of my dissertation committee, Dr. Steve Tung, Dr. Uchechukwu C. Wejinya, Dr. Hanna K. Jensen, and Dr. Jim Leylek for their invaluable advice, support, and mentorship that have made this research possible. Indeed, all the staff of the Mechanical Engineering Department deserve special kudos for making my time enjoyable, and smooth. I would also like to thank the amazing staff at the graduate school for creating a favorable environment for international students.

I extend a hearty thanks to my lab members at AM^3 Lab (past & present): Chao Sui, Nicholas Holt, Jiyu Cai, Lucas Galvan Marques, Mahsa Montazeri, Austin Van Horn, Casey Mullikin, John

C. Miers, and Christopher Schmitt for their supports and inspiration. Thank you for challenging my thoughts process and adding fun to my research experience. Thanks for sharing your culture and amazing cuisines with me. I was fortunate to spend countless hours with Chao Sui in and out of the lab, enjoying his friendship and support. Lucas Galvan Marques deserves special thanks for his assistance in photography, producing some of the amazing images in this work. His expertise in designing electronic circuit has been beneficial to all in the group.

Several companies and individuals have been instrumental to the success of this work. I acknowledge the immense help of Mr. Curt Colopy of I Squared R Element, Company, Inc. for kindly providing a proprietary sample of $MoSi_2$ powder used in making the microheater and sharing his expert knowledge regarding sintering of the microheater. Mr. Jon Guibor, the regional sales manager of CM Furnaces, Inc. was too kind in offering free firing of the microheater. I thank Mr. John J. Cannon of HiDEC at the University of Arkansas for providing the necessary training in using different equipment and his expert advice during the preliminary work on microheater sintering. Regarding 3D printed optics, I thank Clear Ballistics for kindly proving free samples of their gel. I was fortunate to mentor Khalil Wade during his 2016 NSF REU internship to develop the first prototype of the gel printhead. I am grateful to the team of four senior biomedical engineering students (Adeeb Haroon, Colton Tucker, Dakory Lee, and Perla Rocha) whom I worked with during their capstone project, and for giving me another mentorship experience and their assistance in developing the second version of the gel printhead.

My friends, both in Nigeria and the US deserve special thanks for being a big part of my story. You provided what was needed for a successful race. You cheered me to victory, in so many humbling ways. Thank you for believing in me.

Family is where love, support, and encouragement are found. I owe everything first to GOD, the next is to my family for their love, sacrifices, and unending encouragement. I am eternally grateful to my mother, Ekaette Nseowo Udofia and my late father, Joseph (Nseowo) Anderson Udofia for their love and the good foundation they laid for me. To my father, though I did not have the blessing of many days to feast from your well of love and wisdom, your exemplary leadership and commitment to excellence has had a profound drive in my life. You're my hero. I thank my amazing siblings: Idongesit, Anieiti, Uwem, and Ifreke who have always been there for me. I couldn't imagine going through these years without you. Getting through school (high school, college and graduate school) would have been very challenging without the unwavering support of my aunty Comfort Ettentia and her husband, Pastor Essien Ettentia. I thank my aunty, Deaconess Enobong Imeh Bassey and her husband, Elder Imeh Bassey for supporting me at various stages of life. Indeed, "If I have seen further, it is by standing on the shoulders of giants". I realize how blessed I am to have you all in my life. Thank you!

DEDICATION

"GOD delights in concealing things; scientists

delight in discovering things." – King Solomom

To GOD, the One from whom all wisdoms flow, and to the advancement of 3D printing technology, for here lies the future of manufacturing.

TABLE OF CONTENTS

LIST OF TABLES

LIST OF FIGURES

LIST OF PUBLISHED PAPERS

CHAPTER 2: Udofia, E., and Zhou, W., 2019, "A Guiding Framework for Microextrusion Additive Manufacturing," Journal of Manufacturing Science and Engineering-Transactions of the Asme, 141(5) pp. 50801. Published.

CHAPTER 4: Udofia, E., and Zhou, W., 2019, "3D Printed Optics with a Soft and Stretchable Optical Material," Additive Manufacturing. 2019. Submitted.

CHAPTER 1

Background and Objectives

The purpose of this chapter is to provide the general context, and structure of this work. This Ph.D. dissertation documents research advancements in the understanding and applications of microextruion based 3D printing technology.

1.1 Background and Motivation

The ability to fabricate microscale devices has enabled many scientific and technological advances in different areas including biomedical devices[1-3], self-healing materials [4], sensors [5, 6], microfluidic systems [7, 8], and microelectronics[9-11]. Miniature systems offer unique advantages in certain applications with high response time, reduced material waste, low power requirements, drastic cost reduction, and higher packing efficiency [1, 8]. Yet, fabricating microscale devices remains a grand challenge, and one that cannot be fully satisfied by a single fabrication strategy. Of all the manufacturing approaches the photolithography and soft lithography-based fabrication techniques have reached advanced stages for fabricating microdevices; but are burdened by long process cycles, high equipment cost and limited material choice. Therefore, in order to overcome these challenges, new innovations are crucial in the fabrication process.

There is a recent surge to embrace 3D printing technology as an alternative approach for making microdevices due to its cost effectiveness for fabricating complex customizable devices with relative ease. This is evidenced by the 2019 Wohlers reports (including printers, materials, services, and applications) which projects the global market for the 3D printing industry to reach $23.9 billion in 2022, and $35.6 billion in 2024. The report also saw many industrial giants (e.g.,

Airbus, Boeing, Honeywell Aerospace, and United Technologies Corp.) investing in the development of 3D printing technology[12].

This dissertation documents efforts aimed at advancing the understanding and adoption of microextrusion 3D printing technique for microfabrication. Although numerous applications and printing systems have been demonstrated over the years, the fundamental understanding of the printing process and how the various printing parameters can be optimized to accomplish high-resolution features and functional devices is still lacking. Here, the primary motivation is to develop a framework to provide an overall understanding needed for performing successful microextrusion printing for microfabrication. Given the multi-material printing ability and design freedom of microextrusion printing, two important applications were identified and demonstrated: 3D printed optics using a soft and stretchable polymer gel, and 3D printing of a high temperature material for microheaters. In the literature, these applications were identified as possessing great scientific value but are inhibited by fabrication challenges. It is hoped that the results realized herein will provide the scientific and engineering foundations for wider application of 3D printing as a microfabrication tool, with a broad industrial and societal impacts.

The success of the microextrusion printing depends strongly on the ability to dispense fluidic materials from very fine nozzles (e.g., 1 μm). This presents several challenges for the industry in finding suitable methods and materials for fabricating the nozzle, as well as controlling the nozzle size and its surface properties. Significant research efforts have been devoted to these areas and are outside the scope of this study[13, 14]. In this research, we will use pre-pulled glass nozzles, which is the most popular option due to its good surface finish, compatibility with a wide range of materials, and the established fabrication techniques for making fine nozzle tips down to 100 nm. The primary focus of this research is to establish the governing relationship between the various

printing parameters (e.g., nozzle size, printing speed, flow rate, etc.), the ink property and the printing outputs, which is demonstrated through our guiding framework and printing of functional devices.

1.2 Dissertation Objectives

The primary goal of this dissertation is to improve the fundamental understanding of the microextrusion 3D printing process, thereby enabling broader range of utilization for microfabrication. To showcase and validate the versatility of this printing method, two complementary goals of manufacturing system development, and creation of functional devices are proposed. The specific objectives are four-fold as discussed below.

Objective 1: Design, develop, and validate the performance of a high-resolution microextrusion 3D printer that can print both structural and functional devices with micron level precision.

As a first step towards achieving the overall goal, it is necessary to design and develop a 3D printing system for experimental validation of proposed hypothesis, and fabrication of microdevices. Because commercially available printers that can attain the target single digit micrometer resolution are expensive and not easily amendable to enable printing of different types materials, it is proposed to design and implement a low-cost printer. The performance of the printer is evaluated by printing high-resolution 3D PDMS structures in air for the first time.

Objective 2: To develop and experimentally validate a guiding framework for successful microexrusion 3D printing.

The central scientific hypothesis of this research is that improving the underlying principles of microextrusion 3D printing can lead to greater adoption for microfabrication. Therefore, a

comprehensive research is carried out on the various challenges of microextrusion printing. Based on the outcome of study, a guiding framework is proposed, and experimentally validated for successful microextrusion 3D printing.

Objective 3: To develop a low-cost printhead for continuous microextrusion gel printing of a soft and stretchable thermoplastic gel and demonstrate its use for a variety of optical applications.

To provide an inexpensive way for printing an optical grade polymer, a printhead is designed and retrofitted to the developed microxtrusion 3D printer. Next, to accomplish printing of the thermoplastic gel, the process-property relationship is studied. The gel viscosity is characterized as a function of temperature over a range of shear rate. The mechanical and optical properties of the gel are evaluated next to determine its suitability for use in optics. Finally, several exemplary 2D and 3D structures, and optical devices are demonstrated to show its feasibility for optics and applications requiring optically transparent materials.

Objective 4: To research approaches for fabricating a high temperature microheater that can achieve a 1000^{o}C target temperature using microextrusion 3D printing as low-cost manufacturing platform.

Using the microextrusion printer, the design and fabrication of a high temperature microheater that can attain temperatures up to 1000^{o}C is studied. To this end, compatible high-temperature resistive material and substrates are evaluated. The process presents several challenges including ink formulation, printing, sintering, and microheater testing.

1.3 Overview of Dissertation

This dissertation is organized into six chapters, following the chronological order of 3D printer development, development of a guiding framework for printing, and their utilization for fabricating functional microdevices and structures. As illustrated in Figure 1.1, one common theme runs through this dissertation, that is, the development of the fundamental understanding of microextrusion 3D printing and its application for microfabrication.

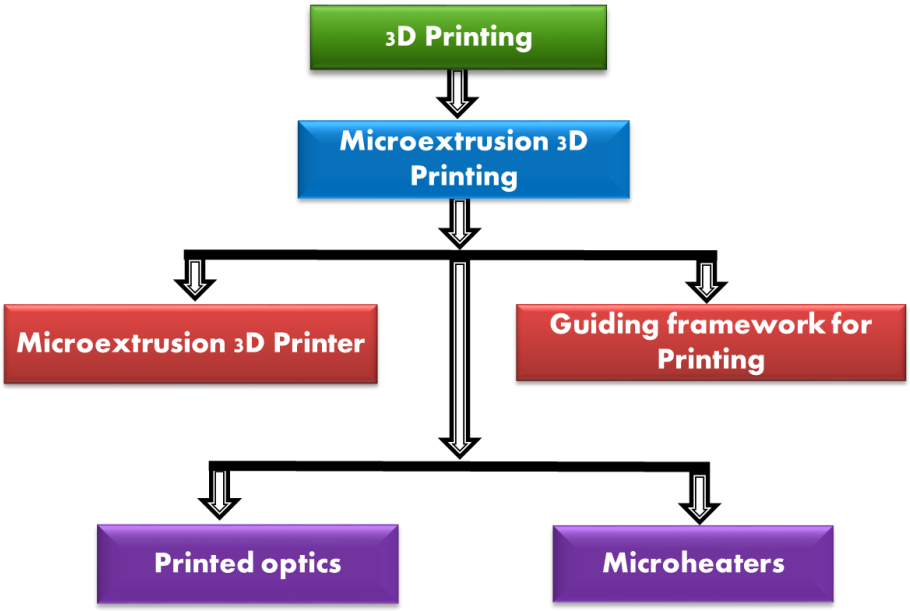

Figure 1.1: Overview of dissertation

First, an overview of this dissertation, including objectives and organization are described in Chapter 1. Chapter 2 documents the design and development of a high-resolution microextrusion 3D printing platform and addresses objective 1. Chapter 3 contains an article published in the Journal of Science and Manufacturing as "A Guiding Framework for Microextrusion Additive Manufacturing" [15], which serves to provide the literature review and guiding framework for successful microextrusion 3D printing. Some of the contents of this chapter were presented and published in the proceedings of the 2018 Solid Freeform Fabrication Symposium with the title,

"Microextrusion Based 3D Printing – A Review" [16]. This chapter directly addresses objective 2 of this dissertation.

In Chapter 4, 3D printed optics with a soft and stretchable material is presented, which addresses objective 3. This work explored the potential of 3D printing of a commercially available soft thermoplastic gel material with an interesting potential for creating optical devices. First, the design and fabrication of the printhead for continuous melt extrusion of thermoplastic materials is discussed. Second, the developed system is used to demonstrate 3D printing of optical waveguides. In Chapter 5, "3D Printing of a High-Temperature Microheater" presents the design and fabrication of molybdenum disilicide ($MoSi_2$) microheater with the goal of achieving a 1000^{o}C target temperature. It covers objective 4. Appendix B provides a short summary of the preliminary work on developing a microheater using silver as the resistive element.

Finally, chapter 6 presents the summary and main findings of this work and provides some potential directions for future research.

1.4 References

[1] Hsu, T., 2002, "Miniaturization–A paradigm shift in advanced manufacturing and education," International conference on Advanced Manufacturing Technologies and Education in the 21st Century, Anonymous .

[2] Chou, H. P., Spence, C., Scherer, A., 1999, "A Microfabricated Device for Sizing and Sorting DNA Molecules," Proceedings of the National Academy of Sciences of the United States of America, **96**(1) pp. 11-13.

[3] Dario, P., Carrozza, M. C., Benvenuto, A., 2000, "Micro-Systems in Biomedical Applications," Journal of Micromechanics and Microengineering, **10**(2) pp. 235.

[4] Hansen, C. J., Wu, W., Toohey, K. S., 2009, "Self-Healing Materials with Interpenetrating Microvascular Networks," Advanced Materials, **21**(41) pp. 4143-4147.

[5] Chabinyc, M. L., Chiu, D. T., McDonald, J. C., 2001, "An Integrated Fluorescence Detection System in Poly (Dimethylsiloxane) for Microfluidic Applications," Analytical Chemistry, **73**(18) pp. 4491-4498.

[6] Weigl, B. H., and Yager, P., 1999, "Microfluidic Diffusion-Based Separation and Detection," Science, **283**(5400) pp. 346-347.

[7] Anderson, J. R., Chiu, D. T., Jackman, R. J., 2000, "Fabrication of Topologically Complex Three-Dimensional Microfluidic Systems in PDMS by Rapid Prototyping," Analytical Chemistry, **72**(14) pp. 3158-3164.

[8] Ikuta, K., Hirowatari, K., and Ogata, T., 1994, "Three-dimensional micro integrated fluid systems (MIFS) fabricated by stereo lithography," Micro Electromechanical Systems, 1994, MEMS'94, Proceedings, IEEE Workshop on, Anonymous IEEE, pp. 1-6.

[9] Ahn, B. Y., Duoss, E. B., Motala, M. J., 2009, "Omnidirectional Printing of Flexible, Stretchable, and Spanning Silver Microelectrodes," Science (New York, N.Y.), **323**(5921) pp. 1590-1593.

[10] Kim, J. T., Seol, S. K., Pyo, J., 2011, "Three-Dimensional Writing of Conducting Polymer Nanowire Arrays by Meniscus-Guided Polymerization," Advanced Materials, **23**(17) pp. 1968-1970.

[11] Sirringhaus, H., Kawase, T., Friend, R. H., 2000, "High-Resolution Inkjet Printing of all-Polymer Transistor Circuits," Science (New York, N.Y.), **290**(5499) pp. 2123-2126.

[12] Forbes, "Signifncat 3D Printing Forecast
[Online] Available: https://Www.Forbes.Com/Sites/Tjmccue/2019/03/27/Wohlers-Report-2019-Forecasts-35-6-Billion-in-3d-Printing-Industry-Growth-by-2024/#2cfb1f817d8a
[Accessed 23 July 2019]," .

[13] Park, J., Hardy, M., Kang, S. J., 2007, "High-Resolution Electrohydrodynamic Jet Printing," Nature Materials, **6**(10) pp. 782-789.

[14] Mittman, S., Flaming, D. G., Copenhagen, D. R., 1987, "Bubble Pressure Measurement of Micropipet Tip Outer Diameter," Journal of Neuroscience Methods, **22**(2) pp. 161.

[15] Udofia, E., and Zhou, W., 2019, "A Guiding Framework for Microextrusion Additive Manufacturing," Journal of Manufacturing Science and Engineering-Transactions of the Asme, **141**(5) pp. 50801.

[16] Udofia, E. N., and Zhou, W., 2018, "Microextrusion Based 3D Printing – A Review," 29th Solid Freeform Fabrication Symposium, SFF 2018, pp. December 27, 2018-2033-2060.

CHAPTER 2

Design and Development of a Microextrusion 3D Printer

Due to its cost effectiveness for making complex and customizable products in simple steps, 3D printing technology has been increasingly embraced for fabricating microscale devices. This has led to investigations into various avenues for developing low-cost uEP platforms. This chapter discusses the successful advancement made in the design, and implementation of a μEP system. The system is designed based on first principles, and with the adaptability for future modifications to enable printing of other kinds of materials.

2.1 Introduction

The high cost of a typical high-resolution microextrusion 3D printers is one of the major factors limiting the access and applications of this printing technology. In this chapter, we address this challenge through the development of a low-cost microextrusion 3D printer. Low-cost commercially available printers are restricted to printing mesoscale structures (i.e., structures with resolution greater than 100 μm) due to their poor resolution. Meanwhile, higher printing resolution may be achieved by using higher precision 3D printers, yet this comes with considerable cost implications (>$200,000) and offer limited room for modification [1].

Previous researches have demonstrated the potential of developing low-cost and customizable printing systems using homemade parts to achieve cost effectiveness and high resolution printing [2, 3]. Motivated by the same objective, we report the design and development of a custom-made microextrusion 3D printer using commercially available off-the-shelf components, with printing resolution down to ~1um, but competitive in cost relative to most commercial 3D printers. The system was designed to satisfy the following requirement:

(1). The printhead system must withstand high pressure in order to dispense viscous materials (e.g., 2000 – 70,000 cP) through fine nozzles;

(2). The motion system must enable precise submicron (~1 μm or better) positional control of the printhead, with a range of adjustable speeds (e.g., 50 μm/s to 2.4 mm/s) to achieve precise disposition of the materials, and high throughput printing;

(3) A 40-50 mm travel range for all the three axes;

(3). The whole system must be fabricated using low-cost components to be economically efficient.

As will be revealed in Chapter 3, the print resolution is dependent on the nozzle size, ink viscosity, printing speed, and dispensing pressure. For instance, small nozzle diameters produce fine resolution prints. Here, Schott Duran borosilicate glass was selected for the deposition nozzle because nozzles down to ~0.1 μm can be made to deliver small quantities of fluids under high pressure (>150psi), and its fabrication technology is well-established [4, 5]. The typical pressure value required to extrude target materials vary from 1-120 psi depending on the nozzle size and the viscosity of the material [6]. An air powered extrusion system was chosen due to its simplicity. In order to overcome the delay in air compressibility in the ink reservoir, and to facilitate instant start/stop, a digitally controlled pressure valve with at 50-100 ms response time was used. The ink is housed in a 10 mL syringe barrel (Nordson EFD).

Finally, in selecting the motion stages, careful consideration was given to cost, resolution, travel range, and printing speed. For ultra-high resolution and repeatability, a piezo-based motor is the clear winner. However, this is expensive for a single digit micrometer resolution in 3-axes and does not offer the desired travel range[7]. A widely employed low-cost alternative is a stepper motor or DC motor coupled to a precision screw. Currently, Thorlabs has recorded a 50 nm

resolution, 50 mm travel range, 800 nm repeatability for their MTS50-Z8 motor. This motor specification readily satisfied the design specification and was therefore chosen for this work.

2.2 Microextrusion Printer Development

Based on the design requirements, a μEP system is developed, which consists of:

(1) The hardware system - printhead system (i.e., ink reservoir, nozzle and pressure regulator), a 3-axis motion stages, a vision system for visualization of the printing process, and;

(2) A software system to integrate and automate the entire printing process.

Most of the hardware components were commercially acquired as off-the-shelf components while the rest were fabricated using 3D printing or traditional subtractive manufacturing processes. Using 3D printed parts was a deliberate effort to limit weight and cost.

Table 2.1: List of printer components

Part	Manufacturer	Part number	Resolution	Cost ($)
X, Y, Z motors	Thorlabs	MTS50/Z8E	50 nm	4,998.31
Syringe	EFD Inc.	7012114	-	82.30
Micronozzles	WPI	TIP30TW1LS01	30±6 μm	145.00
Pressure regulator	Alicat Scientific	PCD-500PSIG	0.10-50 0 psi	1860.00
Aluminum plate	Online Metals	4533	-	459.99
Software	AM^3Lab	Custom-made	-	

2.2.1 Description of the Software System

As shown in Figure 2.1, the motion system consists of X, Y, and Z-axis motion stages. Depending whether the goal is to achieve design simplicity, reduced inertia, increased printing speed, or to maintain high accuracy, there are a variety of possible configurations for the motion system. For this work, the focus was to build a mechanically simple, robust and high-precision system. Hence, the XZ-axis-printhead and Y-axis -printbed arrangement was favored over the XY-axis-printhead and Z-axis printbed arrangement because it is mechanically simple to implement, and the Y-axis will hold less weight to enhance positional accuracy [8, 9]. For the printhead

system, 10 ml a plastic syringe barrel was utilized as the ink reservoir, while the mounting adaptor was fabricated from ABS using Stratasys µPrint SE Plus printer.

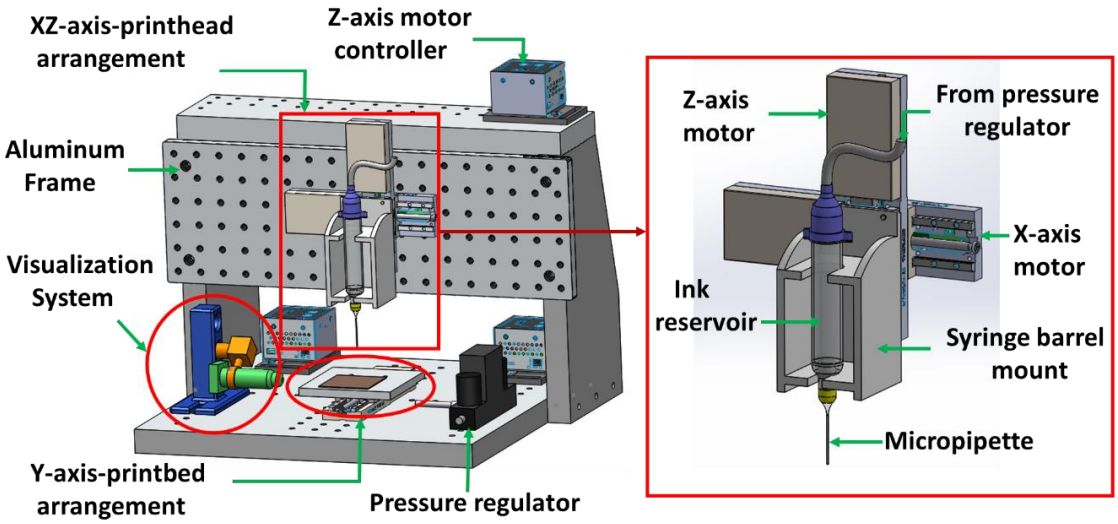

Figure 2.1: CAD model µEP hardware components showing the various sub-systems and their configurations.

A sturdy, modular and low-cost frame was needed to assemble the various hardware components. For this reason, the frame was fabricated using a 1-inch thick aluminum plate due to its low-cost, lightweight, ease of machinability, and corrosion resistance. A modular mounting frame was desired to ensure quick assembly, disassembling, and to enable future system modification as may be necessary.

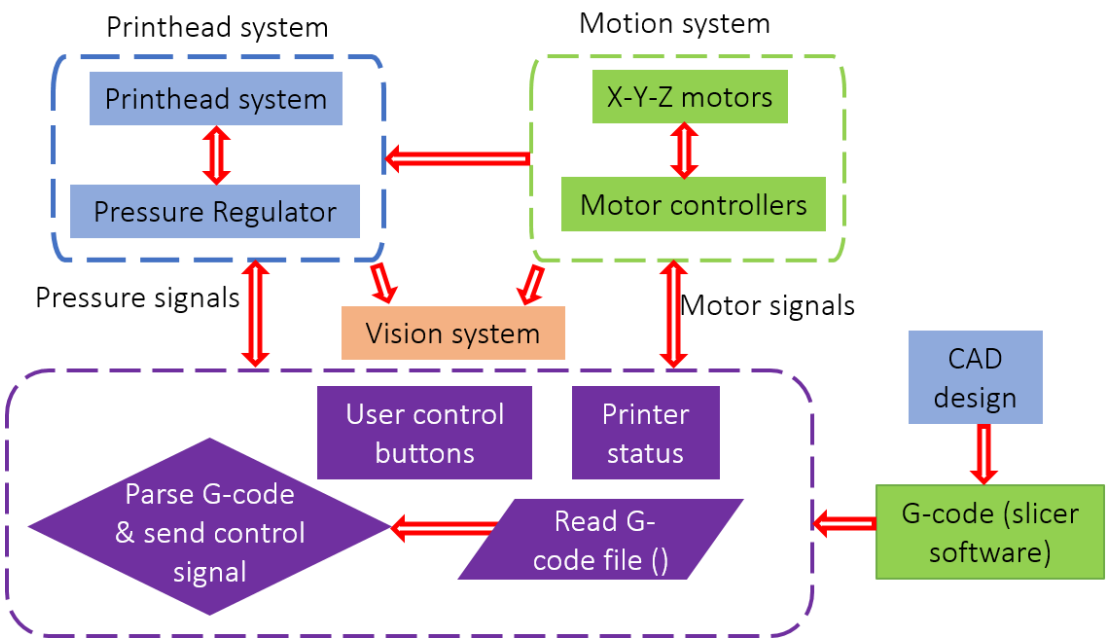

Figure 2.2: LabVIEW implementation of control software

2.2.2 Description of the Software System

For μEP, it is important to integrate and automate the various hardware subsystems. The entire system must by digitally controlled to enable automation and seamless control of tool pathways. Ideally, the μEP should read a standard G-code file, interpret, and convert it to control signals for precise regulation of the XYZ motion stages, and the printhead. In this work, the software was implemented in LabVIEW due to its graphical user interface, and ease of integration with the various subsystems.

Figure 2.2 provides an overview of the software implementation, which integrates the motion and printhead subsystems. The system can be operated in two modes – manual and automated. In the manual mode, the user can vary the printing parameters to determine the optimum printing condition (e.g., extrusion pressure, and standoff gap). When in the automated mode, the software reads a G-code file, generated from open source slicer software (e.g., Repetier Host), parses the

file, and sends control signals to the XYZ motors and pressure regulator. This process is repeated until all the G-codes are systematically executed.

One important part of the software is how we modified the standard RepRap G-code template (e.g., Gnn Xnnn Ynnn Znnn Ennn Fnnn) to suit our system. The "Enn" parameter regulates the dispensing pressure valve instead of motor speed, as used routinely by the fused deposition modeling (FDM) printers. Therefore, whenever the E parameter appears in the G-code line, the digital valve changes the magnitude of supplied pressure. For example, G01 E20 changes the pressure set point to 20 psi. The other parameters remain unchanged, performing the similar functions as the FDM printer. For example, Gnn is the G-code of interest, Xnnn, Ynnn, and Znnn are the positions in X, Y, and Z coordinate to be translated. F represents the translation speed (mm/s) to move between the starting point and ending point, and "nnn" is simply a numerical modifier, representing, in the quantitative sense, how each parameter is changing. Internally, we use LabVIEW's "Match Regular Expression Function" to parse through the G-code array.

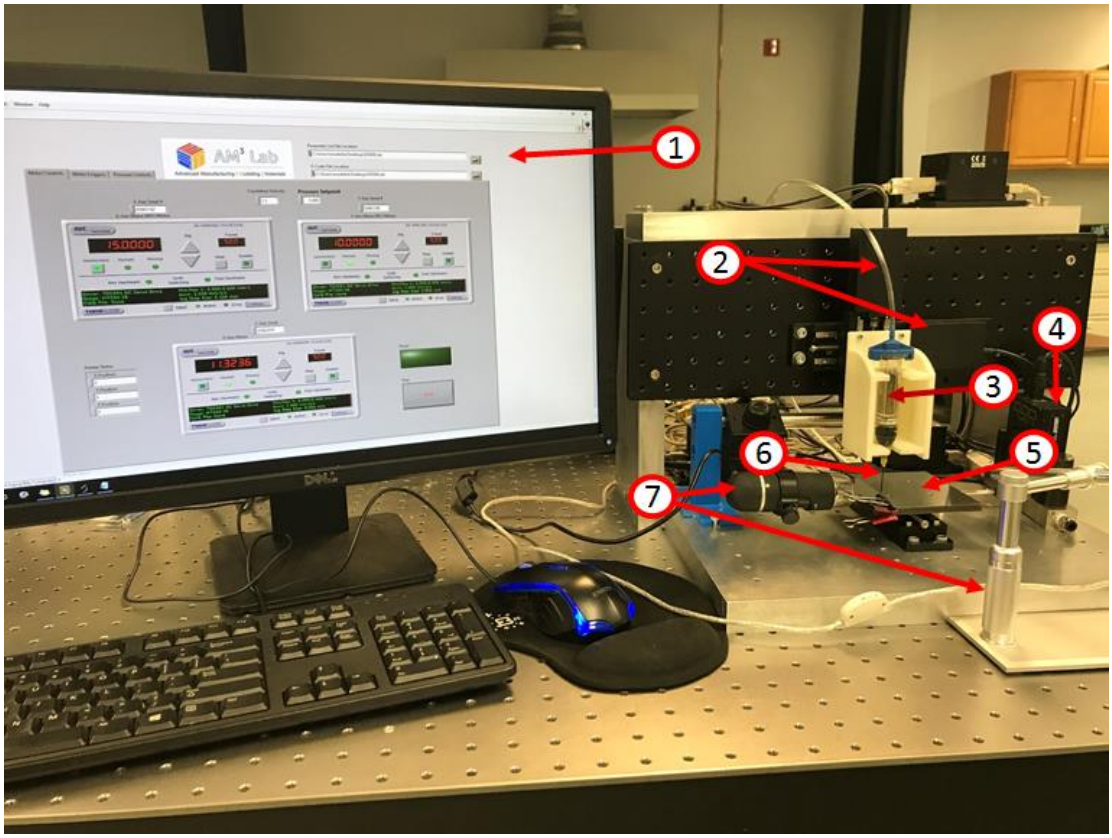

Figure 2.3: Assembly of microextrusion printer sub-systems. - (1) Control software, (2) XZ translation motors, (3) Syringe barrel, (4) Pressure regulator, (5) Printbed, (6) Micropipette, (7) vision systems. Total cost < $20,000.

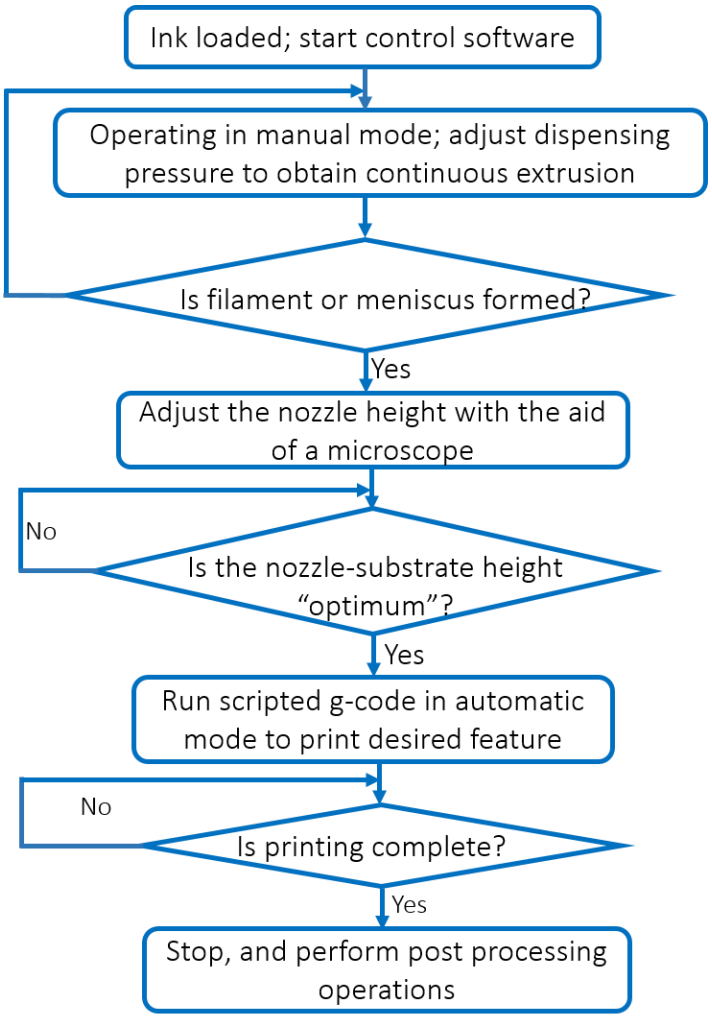

Figure 2.4: Microextrusion printing procedure

The completed microextrusion 3D printer can be seen in Figure 2.3. To successfully use the µEP for printing, a systematic procedure described in Figure 2.4 must be followed. To evaluate if the printer satisfies the target resolution, we printed a series of serpentine patterns using polydimethylsiloxane (PDMS) and achieved printed resolution of ~10 µm (see Figure 3.18 in chapter 3), which shows the printer works as intended.

Table 2.2: Comparison of developed microextruion 3D printer and nScrypt printer[10]

Printer	Minimum feature resolution (μm)	Printing speed (mm/s)	Cost ($)	Build volume (mm^3)	Multiple material printing capability
nScrypt 3Dn-Tabletop	20	300	Expensive (~198,000)	300 x 1500 x 100	Yes
This printer	10	2.4	Low (~20,000)	50 x 50 x 50	Yes

2.3 Conclusion

In this chapter, the design and development of a low-cost microextrusion 3D printer is presented. As will be revealed in the chapters 3 to 5, this multi-material additive manufacturing platform enables the creation of geometrically complex features with resolution down to 10 μm. It offers a low-cost alternative to patterning high-resolution features.

Overall, most of the design requirements set for the printer are met. In Table 2.2 performance of the printer is compared to that of nScrypt 3Dn printer in terms of cost, reported feature resolution, build volume, and the range of printable materials. The total cost of the printer is less than $20,000 (Table 2.1), achieved by using 3D printed parts and low-cost commercially available components (e.g.,10 mL syringe as the ink reservoir, and aluminum frame). This cost is about ten times less than that of nScrypt printer with comparable resolution. In addition, in designing the printer, we adopted a modular arrangement so that the system could be easily improved/modified when the demand for a new application necessitates. This is demonstrated in Chapter 4 of this dissertation, where the system was adapted for printing thermoplastic materials. Commercially available printers such as the nScrypt printer fall short in this area.

2.4 References

[1] Li, B., Clark, P. A., and Church, K., 2007, "Robust direct-write dispensing tool and solutions for micro/meso-scale manufacturing and packaging," ASME 2007 International Manufacturing Science and Engineering Conference, Anonymous American Society of Mechanical Engineers, pp. 715-721.

[2] Ahn, B. Y., Walker, S. B., Slimmer, S. C., 2011, "Planar and Three-Dimensional Printing of Conductive Inks," Journal of Visualized Experiments : JoVE, (58). pii: 3189. doi(58) pp. 10.3791/3189.

[3] Park, J., Hardy, M., Kang, S. J., 2007, "High-Resolution Electrohydrodynamic Jet Printing," Nature Materials, 6(10) pp. 782-789.

[4] Russo, A., Ahn, B. Y., Adams, J. J., 2011, "Pen-on-paper Flexible Electronics," Advanced Materials, 23(30) pp. 3426-3430.

[5] Kim, J. H., Chang, W. S., Kim, D., 2015, "3D Printing of Reduced Graphene Oxide Nanowires," Advanced Materials, 27(1) pp. 157-161.

[6] Dababneh, A. B., and Ozbolat, I. T., 2014, "Bioprinting Technology: A Current State-of-the-Art Review," Journal of Manufacturing Science and Engineering-Transactions of the Asme, 136(6) pp. 061016.

[7] Ouyang, P. R., Tjiptoprodjo, R. C., Zhang, W. J., 2008, "Micro-Motion Devices Technology: The State of Arts Review," International Journal of Advanced Manufacturing Technology, 38(5-6) pp. 463-478.

[8] 3D Printing.com, 2018, "Building a 3D Printer from Scratch (Https://3dprinting.Com/3dprinters/Building-a-3d-Printer-from-Scratch-Tips-Tricks/)," .

[9] Reprap, 2014, "Mechanical Arrangement (Http://Reprap.Org/Wiki/Category:Mechanical_arrangement)," .

[10] "nScrypt, Inc. 3Dn Series Brochure. Available Online: https://Www.Nscrypt.Com/Wp-Content/Uploads/2018/11/2018-3Dn-Brochure.Pdf (Accessed on 16 July 2019)." .

CHAPTER 3

A Guiding Framework for Microextrusion Additive Manufacturing

The creation of microscale devices and structures is a subject of broad scientific interest due to their many applications. This chapter presents a detailed overview and fundamental knowledge of the microextrusion 3D printing technology. The objective is to develop an understanding needed for optimizing the different material properties and control of the process parameters that dictate the resolution and quality of the printed features; thereby providing users at both the research and industrial platforms with the requisite knowledge for adapting microextrusion printing for microfabrication. The chapter is based on the journal paper article published in the Journal of Science and Manufacturing with the same title. While the content remains largely unchanged (although an appendix section has now been included), the layout is modified to suit the formatting of this dissertation.

3.0 Abstract

Although extrusion-based 3D printing processes have seen many successful applications at the macroscale, it has proven to be challenging for consistent, repeatable and cost-effective printing at the microscale due to its dynamic complexities. To fully tap into the promise of microextrusion printing (μEP) of fabricating fine resolution features, it is critical to establish an understanding of the fundamentals of ink flow, interface energy, drying, and the process-property relationship of the printing process. To date, a comprehensive and coherent organization of this knowledge from relevant literature in different fields is still lacking. In this paper, we present a framework of the underlying principles of the microextrusion process, offering an overall roadmap to guide successful printing based on both results in the literature and our own experimental tests. The impacts of various process parameters on the resolution of printed features are identified. Experiments are carried out to validate the developed framework. Key challenges and future directions of microextrusion 3D printing are also highlighted.

Keywords: Microextrusion, micro 3D printing

I. INTRODUCTION

3.1.1 Background and Motivation

Three dimensional (3D) printing has emerged as a relevant manufacturing technology, with the potential to revolutionize the microfabrication industry [1-4]. Microextrusion-based 3D printing (μE-3DP) stands out as a promising alternative for microfabrication with a broad range of applications in biomedical [1, 5-7], self-healing [8], sensors [9, 10], microfluidics [2, 11], and microelectronics[12-14] devices. As opposed to the classical manufacturing techniques, the attractions lie in the greater design freedom, fewer processing steps, lower cost for small

production quantity, and the ability to print on different substrates. Although extrusion-based 3D printing technique has been successfully applied for fabricating macroscale structures, it has proven to be challenging for consistent, repeatable and cost-effective application at the microscale due to its dynamic complexities. Another challenge of Microextrusion Printing (μEP) is extending the range of applicable materials, particularly materials with low viscosity and low surface energies. The fundamental understanding that may help overcome these challenges is still lacking. Herein, our primary motivation is to develop a framework that would provide an overall understanding needed for adapting microextrusion printing for microfabrication.

3.1.2 Overview of Microextrusion 3D Printing

Microextrusion 3D printing describes a material extrusion additive manufacturing (AM) process where material is selectively dispensed through a micronozzle (<50μm) to create 3D features, and the resulting features have at least one of the dimensions below 50μm [15, 16]. It involves the arrangement of a material dispensing system with a pneumatic or mechanical (piston or screw) drive and a computer-controlled robotic platform for extrusion and deposition onto compatible substrates (Figure 3.1) [17]. It usually produces continuous filaments, and is different from other material jetting techniques (e.g., inkjet [18] and electro-hydrodynamic jet (ejet) printing [19]) that produce droplets. This strategy is maskless, cost-effective, with a wide range of material choice, and high-resolution printing capability [20].

The design freedom availed by μEP opens new design possibilities and local material property modulation. To date, this approach has been applied to print a variety of materials including colloidal gels [21, 22], fugitive gel [23], biocompatible [24-29] and polymer-based inks [30-32]. For example, Lewis et al. demonstrated omnidirectional printing of flexible, stretchable, and spanning silver microelectrodes [12]. Dermanaki-Farahani et al.[33] used a combination of

nanoparticle infiltration and microextrusion printing to fabricate functionally graded structural beams with tailored local properties. Printing of functional devices, e.g., batteries [34-36], electronic components (e.g., transistors) [37-40], biomedical [41] and microfluidic devices [42-44], and smart materials [45, 46] are also reported. Ideally, inks for μEP must exhibit a pseudoplastic (or shear thinning) and viscoelastic properties to facilitate the printing of fine ink filament that can rapidly solidify upon deposition for shape retention [47]. However, this requirement constrains the range of usable materials. It often demands careful control of ink rheology, dynamics of fluid flow and deposition, and characteristics of shape retention on the substrate. The driving forces of the ink flow at the microscale are expected to be largely different from those at the macroscale.

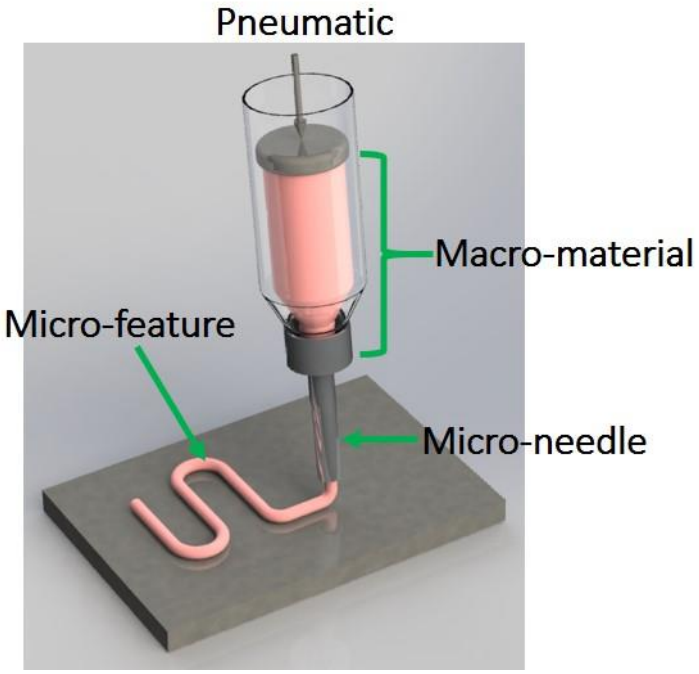

Figure 3.1: Schematic illustration of microextrusion printing.

To make successful prints, generally, there are two primary paths reported in the literature: (1) design of new ink with requisite properties [47], and (2) the development of empirical models

that quantify the effect of the various process parameters on the resolution of printed features [48-50]. For example, Lewis and coworkers have developed several inks, and have successfully printed features with a millimeter to a few micron resolutions [23, 39, 51, 52]. Darta reported quantification of the effects of ink rheology and printing parameters on the resolution of printed features [48]. Besides these, other researchers have also reported models for predicting printing resolution and quantifying the effects of various process parameters, such as extrusion pressure, nozzle size, substrate type and velocity, and standoff distance [24, 53-55]. Nevertheless, these approaches have not addressed the fundamental understanding of the μEP process. There is a high demand for high-resolution printing of traditionally low viscous materials and the understanding that may guide successful application is not fully established [30, 56].

3.1.3 Paper Overview

The interests in adapting microextrusion for different applications spurs the need to investigate and answer some of the fundamental questions: *(1) what are the ink properties that determine printability, and shape retention characteristics? (2) what are the dominant driving forces that govern ink extrusion at the microscale? (3) what are the major factors that determine the final resolution of printed filament? (4) how do we modulate these factors to meet the requirements of target applications?* The ability to understand and answer these questions will determine if one can perform a successful μEP or not. The goal of this paper is to answer these questions. To this end, first, we divided the μEP printing process into four different phases; developed a framework to systematically study all the critical factors that affecting successful printing. Existing knowledge related to the different phases are organized to support the discussions. In the case where sufficient discussion is lacking in the literature, we performed experiments to make the presented framework

more complete. Second, to validate the framework, we carried out experiments to demonstrate how the presented framework can be used to guide successful microextrusion 3D printing.

The rest of this paper is organized as follows. In section II, we first present a roadmap for successful printing – providing a general perspective into the critical parameters affecting the printing process. A guide to controlling each parameter, employing both analytical and experimental techniques to understand the process is offered. Next, in section III, guided by this framework, experimental results of successful printing are demonstrated. Finally, aided by this knowledge, challenges and future direction of microextrusion are discussed in section IV.

II. ROADMAP FOR SUCCESSFUL MICROEXTRUSION PRINTING

The factors influencing μEP are numerous and interrelated. Extruded ink filaments undergo varying static and dynamic phenomena, which bear significant influence on the printing resolution. For instance, the dynamics of the ink that has been deposited on the substrate is very different from the dynamics of the flowing ink at the nozzle tip. To understand the whole process, four phases of microextrusion printing have been identified (Figure 3.2) and will be discussed in this section:

a) Phase 1: Flow prediction inside the nozzle;

b) Phase 2: Extrusion from the nozzle tip;

c) Phase 3: Kinetics of deposition onto a moving substrate;

d) Phase 4: Time-dependent shape retention.

Herein, our objective is to capture the underlying physics of the different phases of the ink deposition process, explaining how the feature resolution is related to the processing conditions, and how this knowledge may be employed to achieve target resolution. The feature area (with width (W), and thickness (H)) can be expressed as a function of surface property (e.g., contact angle θ), printing speed (u), standoff distance (h) and flow rate(Q) (Eq.3.1). Flow rate is a function

of several variables, including pressure (P), ink viscosity (μ), nozzle diameter (D), nozzle length (L) and surface tension (σ).

$$(W, H) = f(\mathrm{Q}(\mathrm{P}, \mu, \mathrm{L}, \sigma, \mathrm{D}), \mathrm{u}, \mathrm{h}, \theta) \tag{3.1a}$$

which can be recast in a non-dimensional form,

$$\pi_1 = f(\pi_2, \pi_3, \pi_4, \pi_5, \pi_6) \rightarrow \frac{W}{D} = f\left(\frac{DP}{\sigma}, Ca, \frac{l}{D}, \frac{h,}{D}, \theta\right) \tag{3.1b}$$

$$\pi_1 = g(\pi_2, \pi_3, \pi_4, \pi_5, \pi_6) \rightarrow \frac{H}{D} = \mathrm{g}\left(\frac{DP}{\sigma}, Ca, \frac{l}{D}, \frac{h,}{D}, \theta\right) \tag{3.1c}$$

$$\mathrm{Ca} = \frac{u\mu}{\sigma}$$

The typical range of the process parameters reported in the literature and their relationships to the feature resolution are summarized in Table 3.1, which briefly explains how each input variable (e.g., printing speed, standoff distance, nozzle size), affects the printing process. Depending on the application, control over feature thickness may be desired at the expense of width and vice versa. For instance, if the desire is to print thin films, then control over layer thickness takes the priority.

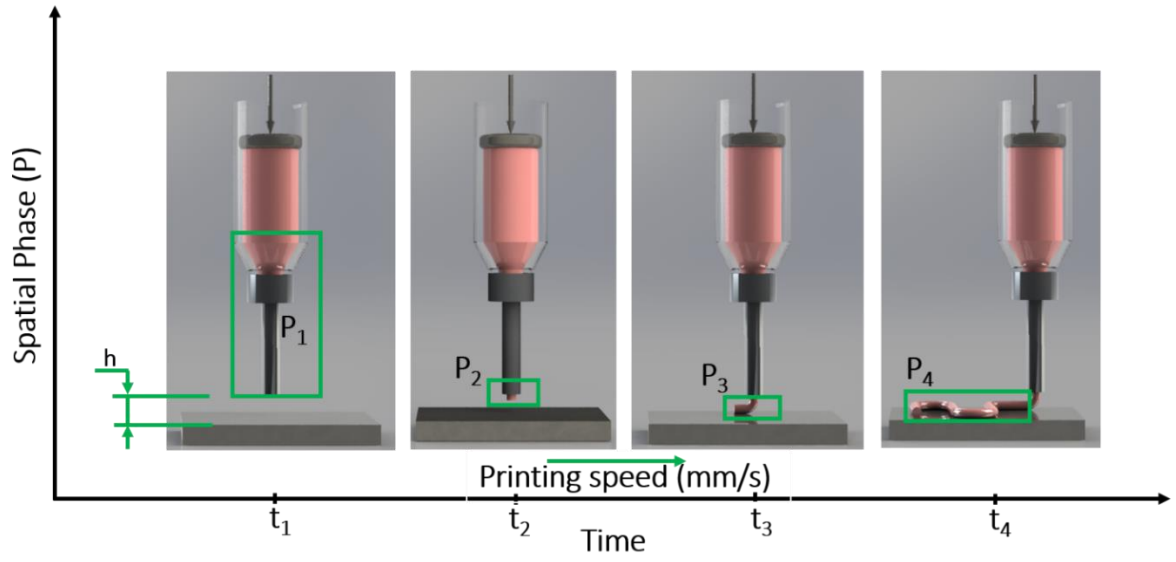

Figure 3.2: Schematic of printing dynamics in different phases (i.e., space and time).

3.2.1 Phase 1: (P1) Flow Prediction Inside the Nozzle

In phase 1, the ink is flowing inside the nozzle under external pressure. An optimal control of ink rheology and extrusion rate are essential to achieving continuous and fine prints resolution. Ink extrusion rate is influenced by three primary factors including ink properties, nozzle geometry and other user-imposed conditions such as temperature (Figure 3.3a). To examine these factors and how they may be optimized, in section 3.2.1.1 we present characterization of the various ink flow behaviors inside the nozzle. In section 3.2.1.2, we describe the effects of nozzle geometries on flow rates, and finally, in section 3.2.1.3, key predictive models for determining flow are presented.

3.2.1.1 Rheological Ink Properties for Microextrusion Printing

Rheology deals with the study of deformation and flow of "fluidic matter" under controlled shear conditions. During the dispensing process, ink is subjected to different deformation and transformational rates due either to the applied pressure, nozzle size, temperature or other processing conditions, which influence their final shape or cell survival (for biological constructs). Rheological characterization provides a means of measuring such changes (e.g., viscosity) since stability, ease of flow, and self-supportability can be directly correlated to the observed behaviors [53, 57-60]. The suitability of a material for μEP is governed by two important criteria: (1) ability to flow easily through fine needles upon application of force, and (2) set immediately after deposition to enable the creation of stable and high-fidelity structures.

In Figure 3.3b we illustrate the two types of flow responses commonly exhibited by 3D printable inks. The simplest case describes a Newtonian ink in which viscosity is independent of shear rate. In practice, most μEP inks are non-Newtonian and show a dependence on shear rate (and are typically shear thinning). The shear thinning behavior is characterized by a decrease in

viscosity as shear rate increases. This behavior is considered ideal for μEP since a decrease in viscosity facilitates flow through nozzles, and rapidly increases upon deposition to enable shape retention [47].

Table 3.1: A summary of important parametric relationships

Variable	Typical Range		Underlying Relationships
Nozzle size	[0.5-50um] • 0.5 μm (Polyelectrolyte inks, μ = 7.6 Pa.s) [61] • 50μm (solder paste, μ =30 Pa.s) [62]	1	Feature resolution is directly proportional to the nozzle size.
Contact angle	[$0^o \leq \theta \leq 180^o$] With 90^o considered as optimum [63]	1	Substrates with low surface energy prevent surface wetting and ink spreading.
		2	High surface energy nozzles and substrates result in a high degree of capillary rise and excessive spreading of printed filament respectively.
		3	The lower the contact angle, the higher the spreading.
Surface tension	11.91- 72.80mN/m [64]	1	As the printing scale goes down, the effect of surface tension increases, and provides additional resistance to ink flow.
Viscosity (μ)	$1.127 – 10^5$Pa.s [3, 55]	1	High viscosity materials require high pressures which make it difficult to extrude through very fine nozzles.
		2	Low viscosity materials flow easily but are plagued with surface wetting issues.
Printing speed	[~1 - 20-500μm/s][65]	1	Relative to the flow rate, a low printing speed results in more ink being deposited per unit time which culminates in poor lateral resolution.
		2	A high printing speed leads to fine features but if not matched with appropriate flow rate can lead to discontinuous filaments.
Deposition Pressure	[$\sim 10^{-4}$ – 7MPa][55, 65]	1	The flow rate is proportional to the applied pressure. Increased pressure translates to increased flow rate.
		2	Excessive pressure could damage ink reservoirs or microneedles and presents safety concerns, which sets an operational limit on the applicable pressure [66].
The Ratio of flow rate to printing speed (Q/u)	Optimal range [~0.7 -1m^2] [55]	1	The ratio of flow rate and printing speed directly affects the printing resolution due to mass conservation.
Standoff Distance	[~ size of the nozzle tip][62]	1	The standoff distance refers to the distance between the nozzle tip and the substrate or the preceding deposited filament layer. As the printing scale goes down (and by effect the standoff distance), flow rate becomes sensitive to the standoff distance. Flow rate decreases as standoff distance decreases [62].
		2	At high standoff distance (about 3 times the size of the nozzle diameter), the excess gap can lead to filament breakup due to the interaction of inertial and surface forces[67].

In general, material viscosity (μ) may be related to the applied shear stress (τ) and shear rate ($\dot{\gamma}$) by [68, 69]:

$$\tau = \mu\dot{\gamma}^{n} \tag{3.2}$$

where n is the flow index (for Newtonian inks, n =1). There are other aspects of ink formulation (e.g., interparticle bonds, pH value, nozzle-to-particles ratio needed to prevent clogging) that are important for different applications but beyond the scope of this paper. Nonetheless, there are already many excellent reviews on these subjects[21, 22, 47, 50, 70-72].

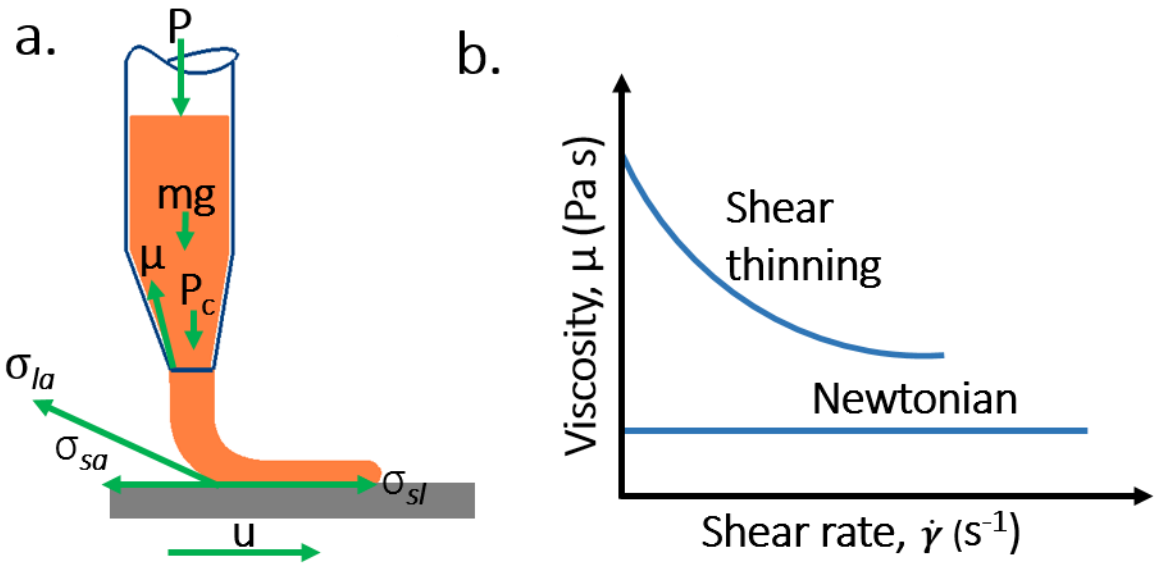

Figure 3.3: (a) Schematic illustration of the dynamics of microextrusion deposition process - applied pressure P; the weight of the ink in the syringe mg; σ_{sa}, σs_{l}, and σ_{la} are the interfacial energy interactions between substrate and air, the substrate and ink, and ink and air respectively; as well as the translating speed of the substrate u. (b) Flow behaviors exhibited by commonly used inks.

In summary, the viscoelastic property of the ink is critical for predicting its flow behavior to achieve fine feature resolution. Although both Newtonian and non-Newtonian inks have been used

for microextrusion, shear-thinning fluid holds an advantage because it reduces the requirement of the driving pressure and improves the shape retention after the ink is deposited on the substrate.

3.2.1.2 Effect of Nozzle Geometry on Fluid Flow

The size and geometry of the dispensing nozzle have significant impacts on the flow rates and need to be fine-tuned to achieve optimal flows. As can be inferred from our illustration in Figure 3.3a, there are three primary factors resisting ink flow inside the nozzle: (1) the nozzle geometry, (2) surface tension, and (3) viscosity. The role of nozzle geometry will be discussed in this section.

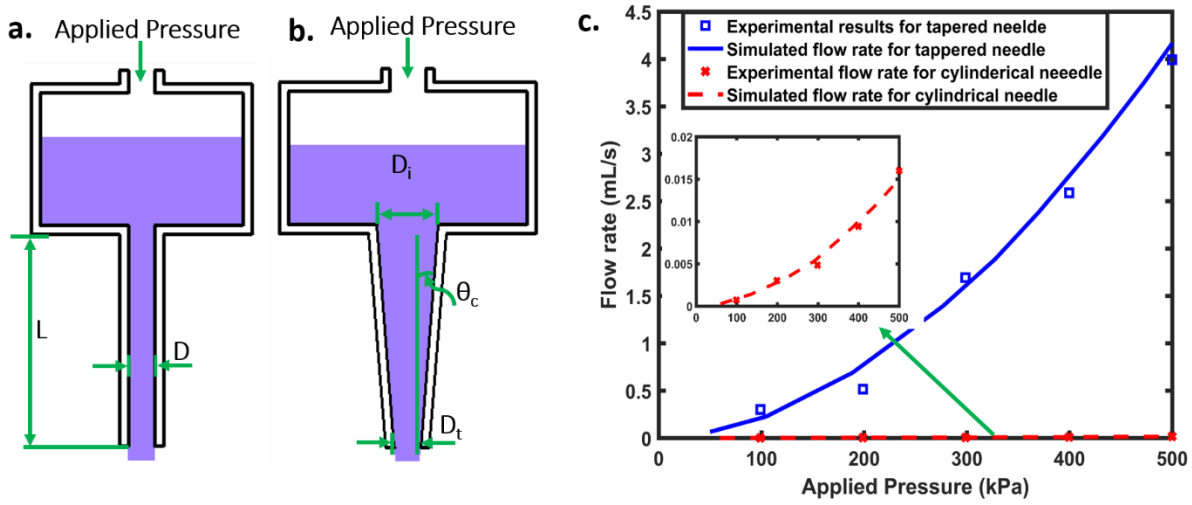

Figure 3.4: Effect of nozzle geometry on flow rates - (a) Cylindrical nozzle, (b) Tapered nozzle. Where θ_c is the cone-half angle, D_i is the inlet diameter, D_t is tip diameter and L is the length of the nozzle length. (c) Comparison of flow rate vs extrusion pressure for cylindrical and tapered needles. Embedded figures are enlargements of cylindrical needle data. Results for 250**µ**m tip diameter (Redrawn based on [69]).

The literature identified two popular nozzle types, cylindrical and tapered nozzles. Results show that under similar operating conditions, the tapered nozzle triggers a higher-pressure gradient (and flow rate) than achievable from a cylindrical nozzle [69, 73]. Figure 3.4c shows the experimental and numerical results carried out by Li et al. [69, 73] for verification of this influence. What they found was that the tapered needle triggered much higher flow rates (~200 times) than

the cylindrical nozzle under the same conditions (i.e., tip diameter is 250μm and extrusion pressure is 500kPa) [69]. A reasonable explanation to this result is that tapered needles typically have larger diameters at the entrance, and a smaller diameter at the tip; a feature which provides a more favorable pressure gradient, dictated by the cone-half angle and tip diameter (Figure 3.4b) [73]. The quantitative effects of the cone-half angle will be discussed in section 3.2.1.3.1 (see Eq. (3.5)). Thus, in situations where the extrusion pressure is limited, a tapered nozzle will be the best option for achieving a higher flow rate, especially when dispensing high viscosity materials.

3.2.1.3 Models for Predicting Flow Rates

Taking the discussions in sections 3.2.1.1 and 3.2.1.2 together, several quantitative models have been proposed for estimating the flow rates. Here, we examine some of these models and offer a discussion on their applicability in predicting flow rates for μEP. First, in

Table **3.2** we provide a summary of the typical flow rates (which are in the range of μ- pL/s), applicable nozzle size, extrusion pressure, and viscosity. One trend is observed in this table, that is, the extrusion of highly viscous materials through fine needles requires high pressures (i.e., pressure requirement increases with increase in viscosity or/ and a decrease in nozzle diameter). In the following sections, we describe equations for predicting flow rate due to external pressure and capillary pressure.

Table 3.2: Typical ink flow rate for microextrusion printing

Ink design	Viscosity (Pa.s)	Flow index (n)	Nozzle diameter (μm)	Applied Pressure (kPa)	Flow rate	References
Newtonian:						
PLLA solution	1.127	1	20	13.33-21.22	0.071-0.113nL/s	[55]
Non-Newtonian						
Polyelectrolyte	0.0076	-	0.5	170	0.00392pL/s	[61]
Cells suspension	-	0.54	250	200-500	0.3-4.0mL/s	[74]

3.2.1.3.1 Flow Due to Applied Pressure

To calculate the flow rate, the Hagen–Poiseuille equation can be used with the following assumptions: 1) laminar flow (due to small Reynolds number); 2) the diameter of the needle is much smaller than its length (D/L <<1); 3) the ink is incompressible; 4) the ink is Newtonian; 5) the applied pressure (P) is the primary driving force for ink flow [55]:

$$\mathrm{Q} = \frac{\pi \mathrm{D}^4 \Delta \mathrm{P}}{128 \mu \mathrm{L}} \tag{3.3}$$

Where ΔP is the pressure difference across the nozzle length (L), μ is dynamic ink viscosity, D is the nozzle diameter. Khalil & Sun developed a modified form of Eq. 3.3 to account for non-Newtonian flow behaviors [24]:

$$Q = \left(\frac{n}{3n+1}\right) \pi \dot{\gamma}_o^{\frac{n-1}{n}} \left(\frac{\partial P/\partial z}{2\mu_o}\right)^{1/n} R^{\frac{3n+1}{n}} \tag{3.4}$$

where R is the radius of the nozzle, μ_o is the viscosity at a low shear rate, $\dot{\gamma}_o$ is the shear rate, z is the direction of nozzle axis, n is the flow index, so that for Newtonian inks (where n =1), Eq.3.4 reduces to Eq.3.3. In constrast with Eq.3.3 and Eq.3.4 which are based on cylindrical nozzle assumptions, for a tapered nozzle geometry (Figure 3.4b), the flow rate may be described by [69]:

$$Q = \frac{\pi D_i^3 D_t^3}{32} \left[\frac{3n\Delta P \, tan\theta_c}{2\mu(D_i^{3n} - D_t^{3n})}\right]^{1/n} \tag{3.5}$$

where D_i and D_t are the diameters of the nozzle entrance and exit respectively as marked in Figure 3.4(a). Clearly, the effect of the nozzle geometry (cone-half angle) and the ink flow index is evident

from this equation. As revealed by Eq. 3.5, the larger the cone half-angle, and the smaller the flow index, the higher will be the flow rate.

3.2.1.3.2 Flow Due to Capillary Pressure

In addition to the influence of applied pressure and nozzle geometry, in micronozzles where the influence of gravity is negligible, ink flow becomes highly sensitive to surface forces (e.g., surface tension and surface roughness) [75, 76]. As the ink flows from the ink reservoir into the nozzle before the nozzle is fully filled with ink, the differential wetting of the internal nozzle surface creates a pressure gradient (known as capillary pressure, i.e., $P_c = P_{nw} - P_w$,) which drives the flow. Because the advancing liquid front can be approximated as quasi-equilibrium, the force balance may be expressed in terms of the dynamic contact angle, surface tension and nozzle diameter as follows (Figure 3.5a-b):

$$P_{nw}(\pi R^2) = \sigma \mathrm{Cos}\theta_D(2\pi \mathrm{R}) + P_w(\pi R^2) \tag{3.6}$$

$$P_c = (P_{nw} - P_w) = \frac{2\sigma \mathrm{Cos}\theta_D}{R} = \frac{4\sigma \mathrm{Cos}\theta_D}{D} \tag{3.7}$$

Where P_c is the capillary pressure, P_{nw} is pressure in nonwetting phase, P_w is pressure in the wetting phase, σ is the surface tension, and θ_D is the dynamic contact angle [77, 78]. As revealed by the above equation, the physics of capillary pressure is solely controlled by the dynamic contact angle and its strength increases as $D \rightarrow 0$, which means the smaller the radius, the higher the capillary pressure. And since $P_w > P_{nw}$, the net pressure is negative, this means the resulting pressure is acting in the downward direction.

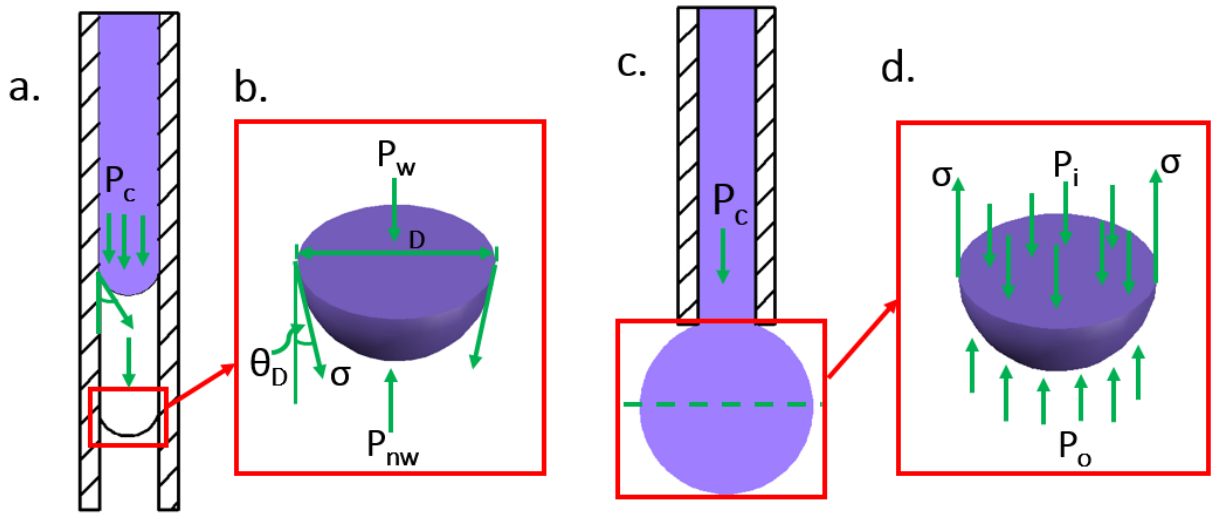

Figure 3.5: Overview of capillary pressure and surface tension effects. (a) Illustration of capillary driven flow due to the interfacial interaction between the ink, nozzle surface, and air. (b) Illustration of force balance between the wetting and non-wetting phase of the droplet in capillary flow, (c) Spherical ink droplet formed at the nozzle tip, (d) Force balance between the surface tension, internal and ambient pressure in the hemispherical droplet.

Under this condition, Washburn [75] showed that the flow velocity may be approximated by:

$$v = \frac{D\sigma}{8\mu L} cos\theta_D \tag{3.8}$$

Thus, the rate at which ink flows inside the nozzle under its capillary pressure is directly proportional to the capillary diameter *D*, surface tension σ, to the cosine of the contact angle, to the surface tension and inversely proportional to the ink viscosity and nozzle length. For high viscosity ink and small nozzle sizes, the capillary pressure may become an effective way to draw the ink to fill the nozzle. When the ink reaches the nozzle tip the flow behavior is rather complicated, and no longer due to the capillary pressure but driven by the interplay among the surface tension, surface wetting of the nozzle tip, and gravity (as the drop increases in magnitude at the tip) [79].

3.2.1.3.4 Surface Tension Resistance at the Nozzle Tip

As the ink progresses to the nozzle tip, the molecules at the interface between the ink and air experience different forces than the interior molecules. Consequently, the tendency is for the ink to assume a spherical shape in order to minimize the surface energy, and a pressure difference exists between the internal and external atmosphere (Laplace pressure), which can be described as below (see Figure 5c-d for the force balance relationship) [80].

$$(2\pi R)\sigma = \Delta P(\pi R^2) \tag{3.9}$$

So that,

$$\Delta P = \frac{2\sigma}{R} = \frac{4\sigma}{D} \tag{3.10}$$

This assumes that the filament (or droplet) radius r_d is much smaller than the capillary length, L_c (where $L_c = \sqrt{\frac{\sigma}{\rho g}}$, where g is gravity and ρ is ink density) and thus gravity effect is negligible, which is valid for the length scale of this work [81]. Unlike the capillary pressure that drives the flow to fill the nozzle, the surface tension at the nozzle exit resists the ink from exiting the nozzle. To underscore the significance of the surface tension pressure on the ink dispensing process, let us consider the variation of the surface tension pressure for two different nozzle sizes (1μm and 1nm) supposing water is being dispensed. At the stated condition, one must overcome a pressure ~288kPa and 288MPa respectively (i.e., $\Delta P = 4\sigma/D$, $\sigma_{water} = 71.97 mNm^{-1}$) due to surface tension which is present at the liquid-air interface. It is easy to see that the surface tension pressure increases significantly as the nozzle diameter decreases and represent a significant impediment to successful microextrusion.

In summary, the ink flow rate is: (i) inversely proportional to the viscosity (μ); (ii) directly proportional to the applied pressure (P); (iii) inversely proportional to the nozzle length (L); (iv)

directly proportional to the fourth power of nozzle diameter for a Newtonian ink. The strong dependence of the flow rate on nozzle diameter and the larger cone half-angle is apparent. For instance, based on Eq. 3.3, the desire is to increase flow rate, then increasing the nozzle diameter by a factor of 2, with other parameters fixed, the flow rate increases by a factor of 16 (i.e. $Q \sim D^4$). In the case of a shear thinning ink, Eq. 3.5 shows that the smaller the flow index, the higher will be the flow rate.

3.2.2 Phase Two (P_2): Extrusion from the Nozzle Tip

As the printing progresses to phase 2, there are many possible outcomes, including nozzle clogging, surface wetting, and a high degree of solvent evaporation. Each unique phenomenon is a function of the ink flow (e.g. ink velocity and viscosity at the nozzle exit) and interface properties (e.g., temperature and humidity of surrounding air, and surface energy of the nozzle tip). Our objective is to capture the underlying dynamics as the ink exits the nozzle into the air and interacts with the nozzle surface. This complex process will be discussed under two categories: capillary rise effect in section 3.2.2.1, and the evaporative effect in section 3.2.2.2.

3.2.2.1 Capillary Rise Effect

Capillary rise refers to the upward rise of dispensed ink at the nozzle tip-air interface due primarily to the interplay between inertial, viscous and surface forces. There are two possible causes of this observation. First, pneumatic dispensing systems suffer from a time lag between when the "stop printing" process is initiated, and when ink flow stops. This phenomenon can lead to ink still oozing out at a low velocity and subsequent build-up at the nozzle tip during translation from point to point where material extrusion is not required and may, therefore, impede smooth dispensing and lower the print resolution. Second, capillary rise is driven by ink wettability at the

nozzle tip, which describes the degree of affinity between a liquid and the nozzle surface [82], and this tendency is increased if the nozzle surface is hydrophilic [79], and if the ink is of low viscosity and flowing at low velocity. Here, we examine instances where capillary rise could become a significant challenge and understand how to control the process to achieve high-resolution printing.

In order to obtain a quantitative estimate when capillary rise may be significant, the capillary number (Ca), may be calculated to express the relative importance of the surface tension to viscous force:

$$Ca = \mu v/\sigma \tag{3.11}$$

As can be understood from this equation, the surface tension force tries to reduce surface area by maintaining a spherical shape, while the viscous force opposes any possible change in shape. A strong indication of capillary dominated flow occurs when Ca = 10^{-1}~10^{-3}, with high surface tension liquids being more likely to form droplets. Hence, as a rule of thumb, ***with a hydrophilic nozzle surface and Ca < 10^{-1}*** [81] ***then the ink may wet the nozzle surface, leading to capillary rise.*** To validate this theory, Figure 3.6 shows our experimental results, using 100 wt.% glycerol ink. According to results by Chang et al. [79] and buttressed here by the experimental results, at low flow velocity and low viscosity inks, the extrusion process is marked by low capillary number (Q =228pL/s, v =0.323mm/s, Ca =6.38x10^{-3}), and ink filament is pulled upward along the nozzle surface if the surface energy of the nozzle is greater than that of the ink ($\sigma_{e(glass)}$= 310mN/m, $\sigma_{e(glycerol)}$ = 70.9mN/m) (Figure 3.6b). Subsequently, the ink is observed to grow into a spherical shape which is about 9-fold greater than the nozzle diameter (Figure 3.6c). In contrast, as the capillary number increases, (i.e., by increasing the flow rate, Q =3.91.8nL/s, v =5.54mm/s, Ca

$=1.09x10^{-1}$), continuous ink filament is produced with a diameter equal to the nozzle diameter (Figure 3.6d).

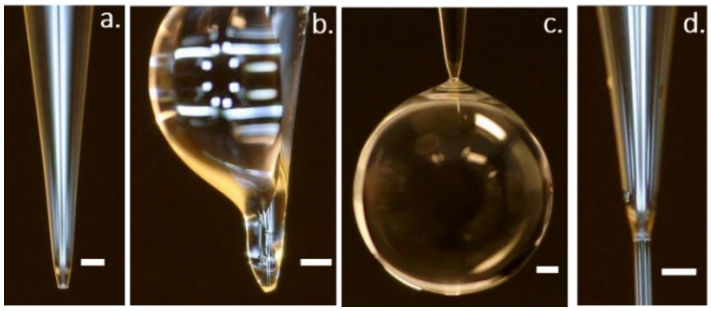

Figure 3.6: Illustration of capillary rise effect using 100% glycerol with 30um nozzle tip – (a) Unfilled nozzle tip, (b) At 7 psi extrusion pressure, capillary rise hinders formation of ink filament or droplet, (c) Droplet grows to ~9*D before pinching off, (d) At 120psi, continuous ink filament is produced, which is about the size of the nozzle tip. (Scale bars are 60μm).

Table 3.3: Required flow velocity to overcome capillary rise for typical ink properties (i.e., Ca >0.1)

Viscosity (μ)	Surface tension (σ)	Flow velocity (v)
$1.127 – 10^5$ Pa.s	11.91- 72.80mN/m	$1.2x10^{-6}$ - 6.54 mm/s

In summary, capillary rise effect tends to cause ink build-up at the nozzle tip and lowers print resolution. In the extreme case of high evaporative effect (see the next section for discussion) partial clogging of the nozzle may be observed. Nonetheless, to attain a successful extrusion under this condition, the standoff distance must be carefully adjusted by bringing the nozzle tip close to the substrate so that the ink meniscus directly contacts the substrate once it exits the nozzle tip and dragged along the substrate. In relation to the length scale, as the length scale goes down (if other factors remain the same) the tendency of capillary rise increases. To limit the effect of capillary rise, the literature reports the usage of high viscosity materials and nozzle surface coating [31, 83]. At different combinations of ink viscosity, surface tension, and ink flow velocity, Eq. 3.3 may be used to determine the appropriate working range such that capillary number Ca >0.1. For example,

in Table 3.3 for different values of surface tension and viscosity, we present the typical flow velocity required to keep the capillary number greater than 0.1.

3.2.2.2 Evaporative Effect

Evaporative effect describes the change in flow behaviors due to the rapid solvent loss in the extruded ink filament at the periphery of the nozzle tip-air interface. Significant moisture loss can alter ink rheology, and flow rates by causing partial or complete ink solidification at the nozzle tip [51, 71, 84]. On the other hand, accelerated solvent loss (Figure 3.7, due to the increased surface-area-to-volume ratio) have been employed for the creation of arbitrary free-standing structures [85, 86]. Under isothermal condition, the rate of solvent evaporation is enhanced by two primary factors: (1) the prevailing ambient condition (e.g., relative humidity), and (2) boiling point of the solvent (e.g., Isopropyl alcohol- boiling point 82.5^{o}C, water -boiling point 100^{o}C, ethylene glycol - boiling point 197.3^{o}C, and glycerol -boiling point 290^{o}C) [3].

To gain a perspective if evaporative effect would pose a printing challenge, we propose to compare the drying timescale and the extrusion time scale. For instance, if the drying timescale is much smaller than the flow timescale, a large amount of solvent evaporates affecting ink extrusion. Conversely, if the drying timescale is very large compared to the flow timescale, very little moisture is lost before it flows out, and this effect becomes insignificant. To this end, we performed a quantitative analysis of evaporation and flow rates, to estimate their relative significance. For the simple case of a stationary spherical droplet of a pure liquid, the rate of evaporation into the ambient air may be expressed by Eq.3.12:

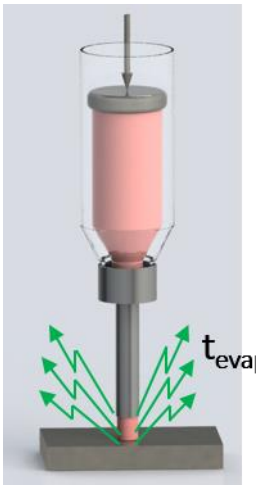

Figure 3.7: Illustration of solvent evaporation at the microscale.

$$I = \frac{-dm}{dt} = -\rho \frac{dV}{dt} \tag{3.12}$$

where I is the evaporation rate with a unit of g/s, m is the mass of drop, ρ is the density of the ink, and V is the volume of the drop. Birdi et al. [87] expressed Fick's law for the rate of evaporation as follows:

$$\mathrm{I} = 4\pi \mathrm{r_d J}(\mathrm{c_o} - \mathrm{c_\infty}) \tag{3.13}$$

where J (mm^2/s) is the diffusivity of the vapor and depends on the temperature, and c (g/mm^3) is the concentration of the vapor per unit volume of air ($c = c_\infty$, at $r = \infty$; $c = c_o$ at $r = r_d$, where r_d is the radius of the liquid drop). By combining Eq. 3.12 and 3.13, and integrating gives an expression for evaporation timescale:

$$t_{evap.} = \frac{V}{4\pi \mathrm{r_d}} \frac{\rho}{\mathrm{J}(\mathrm{c_o} - \mathrm{c_\infty})} \tag{3.14}$$

On the other hand, the flow timescale may be expressed as the ratio of the nozzle radius (R) and the average extrusion velocity (v).

$$t_{flow} = \frac{R}{v} \tag{3.15}$$

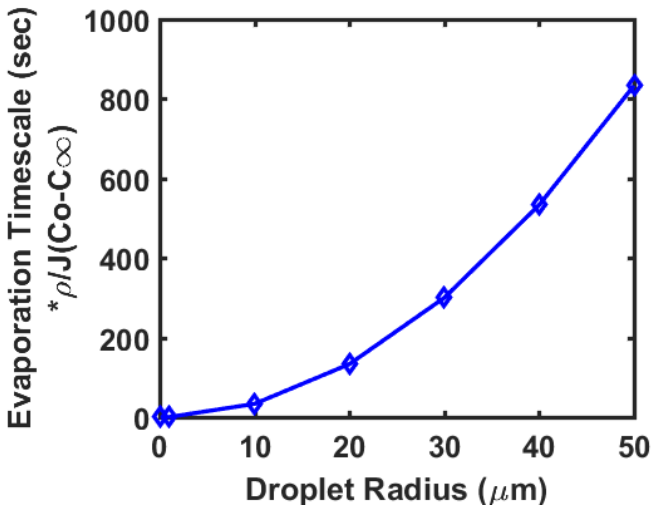

Figure 3.8: Plot of evaporation time as a function of droplet radius based on Eq. 3.14.

To understand how evaporation timescale changes with printing scale, we plotted the evaporation timescale against different values of droplet radius based on Eq. (3.14) (Figure 3.8). As revealed here, at a constant temperature and relative humidity, the volume-to-surface-area ratio ($V/4\pi r_d$) becomes the only variable in Eq. 14 and shows that the evaporation timescale decreases quadratically with a decrease in droplet radius. On the other hand, a linear relationship exists between the flow time and the droplet radius (Eq. 3.15). Therefore, for a given ink, if the filament geometry, flow rate, and diffusivity of solvent into ambient air are known, then evaporation and flow timescales can be calculated to estimate their relative effects.

For example, to compare these two timescales, we considered extrusion of water from a 30μm diameter nozzle and a flow rate of 0.358μL/s ($v = 5.08 \times 10^{-4}$mm/s). At 40% relative humidity, water vapor diffusivity J = 26.1mm^2/s [88], the flow and evaporation timescales are 1.97s and 5220s

respectively. The importance of this result is that under the stated conditions, flow happens ~2650 times faster than evaporation, and would therefore not affect printing significantly. On the hand, if printing was done using a 1μm nozzle and a flow rate of 0.443fL/s ($v = 5.65 \times 10^{-7}$mm/s) under the same conditions, the flow and evaporation timescales would be 1770s and 0.194s respectively. This means evaporation happens ~9123 times faster than flow and will, therefore, hinder successful printing. Towards limiting the high rate of evaporation, printing inside a non-wetting oil reservoir have been reported [51, 68]. Evidently, the need to overcome alterations in ink rheology and nozzle clogging arising from the rapid drying rate (at the microscale) presents several challenges to be overcome and hinders the drive to further improving the printing resolution. Some of these challenges include appropriate ink formulation [51, 68], and better control of the printing environment and innovative support materials formulation [89].

3.2.3 Phase 3 (P3): Kinetics of Deposition onto a Moving Substrate

In this phase, the ink filament makes the first contact with the translating substrate, and a plethora of experimental and numerical evidence from the literature demonstrate the critical influence of the substrate speed on the print resolution [21, 59]. However, little research has been reported on answering the critical question of whether *the substrate translating speed drive ink flow from the nozzle*. For instance, at very low flow rates, the substrate speed exerts a dominant influence on the flow rate and may, therefore drive ink flow. Herein, we take the experimental route to demonstrate and answer this question which may open a new avenue for patterning features from very fine nozzles where the demand for high pressure may prove challenging. To effectively capture this observation, the discussion in this section will be divided into two sections: the effect of standoff distance (section 3.2.3.1) and the effect of the translating substrate (section 3.2.3.2).

3.2.3.1 The Effect of Standoff Distance

There are two primary effects of the standoff distance on μEP which we now offer explanatory insights. The first relates to its influence on ink flow rates. It is found that if other parameters are held constant, decreasing the standoff distance to less than ~50% of the nozzle diameter leads to increased flow resistance. That is conceptually equivalent to reducing the effective nozzle diameter, which leads to a reduction of flow rate (Figure 3.9a & Figure 3.10a) [90, 91]. The need to reduce the standoff distance is a consequence of utilizing fine nozzles, in which case, the standoff distance must be finely tuned as well in order to produce continuous prints.

The second concerns the stability of the ink deposition process and filament geometry. Through an empirical study, Wang and Shaw [21] showed that for a given set of flow rate(Q), nozzle diameter, and printing speed (u), there is a critical standoff distance (h_c) that guarantees that just enough amount of material is available between the nozzle and the tip and the substrate expressed as:

$$h_c = \frac{Q}{uD} \tag{3.16}$$

At this instance, the standoff distance is equivalent to the filament height, H (Figure *3.9*b) and gives the proper contact angle without inducing forced ink spread. When $h < h_c$, a compression effect will be induced (forced spreading) and by effectively altering the contact angle (Figure *3.9*a). This contact angle is no longer the equilibrium contact angle determined by the surface property. In contrast, at a high standoff distance (i.e., $h > \pi D$) [67, 92] the ink filament can become unstable, leading to filament break up into discrete droplets due to the Plateau-Rayleigh instability [50], and poor adhesion to the substrate (Figure 3.9c, d).

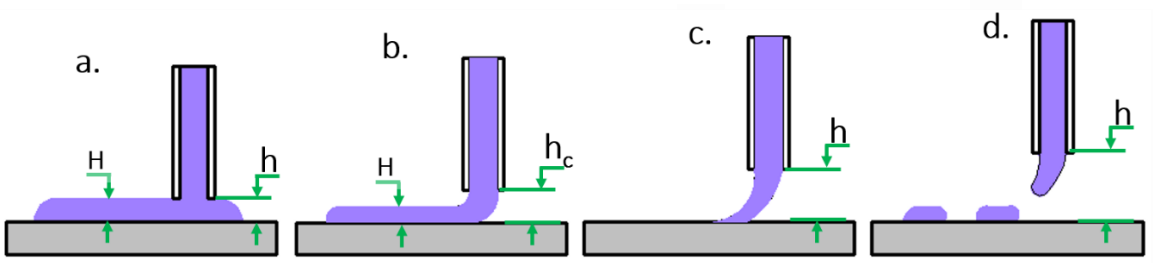

Figure 3.9: Schematic illustration of the effect of standoff distance – (a) Standoff distance too short, (b) Proper standoff distance, (c), (d) Standoff distance too large.

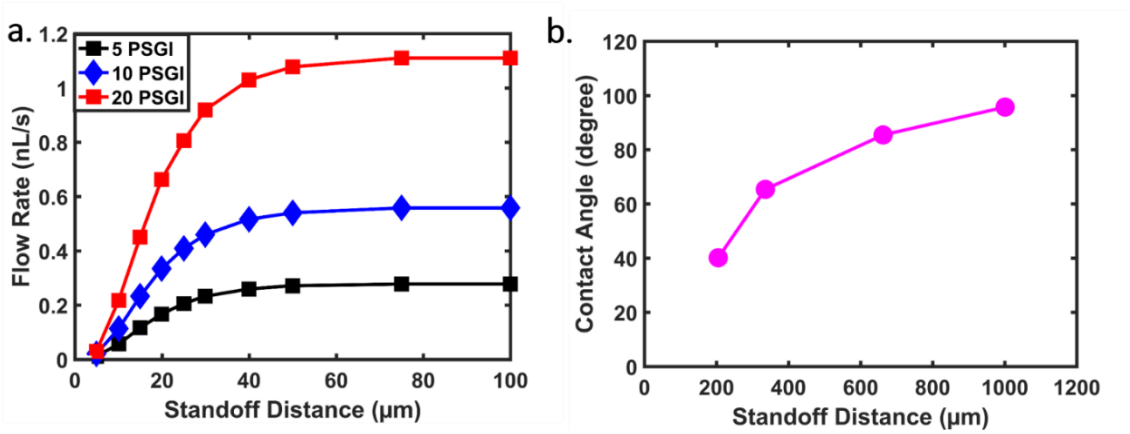

Figure 3.10: Illustration of the effect of standoff distance: (a) On flow rate using 50**μ**m nozzle tip (redrawn based on [62]), (b) On contact angle using 700**μ**m nozzle tip (redrawn based on [21]).

When h> h_c there is enough space for the ink to occupy, albeit, excessive gap can cause filament stretching and by effect altering the contact angle as well. This stretching effect has been attributed to surface tension force [93] and gravity[94].

By measuring the contact angle, Wang and Shaw [21] obtained a quantitative estimate of the degree of filament spreading due to low standoff distance. In their study, it was revealed that when standoff distance h is 670μm (which was near the critical value, h_c = 840μm), no spreading was observed, and the equilibrium contact angle at this point is ~85^o (Figure 3.10b). On the other hand, when the standoff distance was decreased from 670 to 335μm, the contact angle decreased from ~85^o to 65.3^o (~ 23.2% decrease). However, when the standoff distance was increased from

670 to 1000μm, very little change in contact angle was observed (~85 to 95.7^{o}, ~12.6% increase). As will be revealed in section 2.2.4, a low contact angle is indicative of ink spreading.

The current barriers to improving printing resolution due to the requirement of proper standoff distance are summarized as follows and illustrated in Figure 3.11. For example, if the nozzle tip is too close to the substrate, the nozzle can be damaged (Figure 3.11b), while large standoff gap results in discrete droplets (Figure 3.11c). Furthermore, a high standoff distance will increase the travel time of the filament through air relative to drying time, ink solidifies before reaching the substrate; hence poor adhesion to substrate and poor layer to layer bonds. In general, a standoff distance of about the same size as the nozzle diameter is recommended in order to achieve continuous ink filament, improve layer to layer bonds, as well as adhesion to the substrate, and avoid deposition time delay[62, 67, 94, 95]. To accurately control the standoff distance (e.g., <1μm), a high magnification telescopic lens is usually employed which also serves a secondary purpose of visualizing ink meniscus formed between the nozzle tip and the substrate [65]. Other systems incorporate a precision height sensor for the Z-stage. Here, the sensor scans the surface of the substrate prior to deposition and adjusts the nozzle tip to the set value without damaging it [62]. However, the downside of such advanced systems is that it increases the machine cost (~$200,000) and offer limited room for modification.

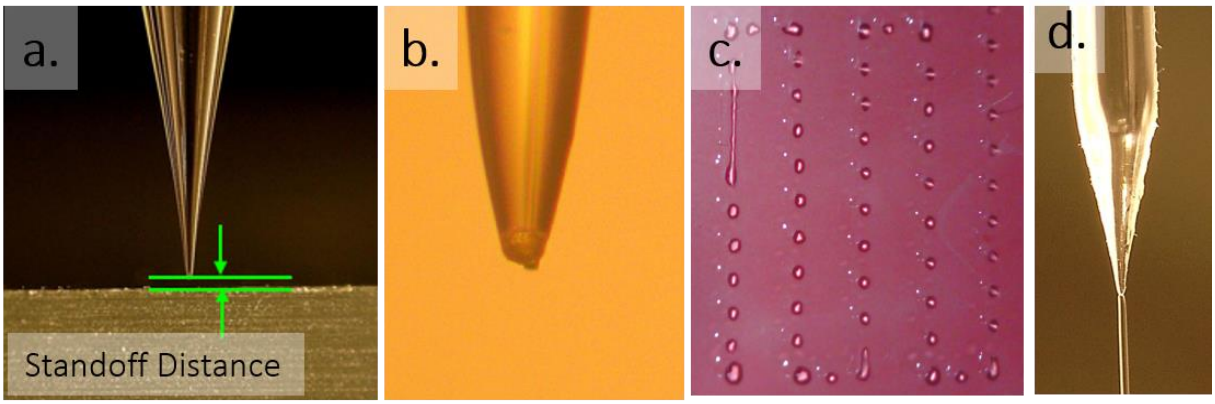

Figure 3.11: Illustration of standoff distance optimization - (a) Nozzle-substrate alignment to achieve optimum standoff distance, (b) Standoff distance too small leading to the broken nozzle; (d) Standoff distance too large leading to discrete droplets, (d) Proper standoff distance produces continuous ink filament.

3.2.3.2 Effect of a Translating Substrate

To address the question, *does the substrate translating speed drive ink flow from the nozzle*? Our guiding hypothesis is that, at low flow rates, if the substrate's speed exceeds the flow speed (v), then ink is drawn out of the nozzle by the translating substrate. As used here, low flow rate refers to creeping flows (or Stokes flow). Flows in which the Reynolds number (i.e., $Re = \rho v D/\mu$), $Re<10^{-1}$ are classified as Stokes flows, so that viscous forces dominate over inertial forces, which is a characteristic of very high viscosities, very low flow velocities, or flow in micro/nano length scales[96]. While low flow rates may give rise to dripping droplets and capillary effects (see section 3.2.1.), for high flow rates, inertial forces dominate, and the flow is characterized by high flow velocity which may cause unstable ink jetting and poor printing resolution[97]. Either way, the printing parameters must be carefully controlled in order to achieve high print resolution. The possibility of ink being drawn out by a translating plate was first demonstrated by Landau and Levich [98], who developed a theoretical model for predicting the liquid film thickness formed on a plate that is vertically withdrawn from a solution reservoir at a constant speed. Subsequent works

have detailed the application of this technique for controlled thin film deposition (in the case of horizontal plate motion), in a deposition technique termed “meniscus guided coating” [99, 100], as well the meniscus guided printing [85, 86] techniques. Of these techniques, the meniscus guided printing could be likened to the μEP printing technique. The major difference between μEP and meniscus guided printing is that meniscus guided printing works by “guided” vertical stretching of ink (typically low viscosity) meniscus from a micropipette and exploiting the rapid solvent evaporation to pattern freestanding structures. Here, contact is first established between the ink meniscus and the substrate by bringing the nozzle tip close to the substrate. This is followed by a vertical pulling of the nozzle to create fine features [101].

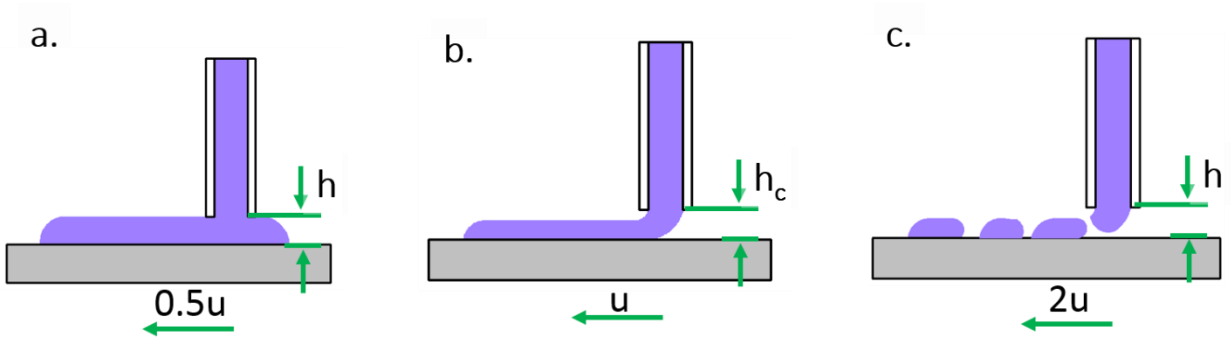

Figure 3.12: Schematic illustration of the effect of printing speed at a constant flow rate and standoff distance - (a) Printing speed too low, resulting in a smearing of the ink filament, (b) proper printing speed, (c) Printing speed too high resulting in discontinuous ink filament.

In general, similar to Eq. 3.16, the observed pattern is that, at a constant flow rate and standoff distance, there is critical printing speed at which the filament diameter equals the nozzle diameter, defined by Eq. 3.17 [21, 24].

$$u_c = \frac{Q}{Dh} \tag{3.17}$$

The physical meaning of this equation is that the ink flow rate (Q) determines the amount of material available for deposition within a given space and time. If the substrate speed is less than this value, the ink filament may become compressed resulting in forced flow (Figure 3.12a). On the other hand, while faster printing speed is usually preferred to reduce build time, if it is greater than the critical value, a stretching effect will be induced in the ink (Figure 3.12b). A further increase in speed may result in unstable and discontinuous prints (Figure 3.12c). Filament breakup process has been studied extensively and could be likened to uniaxial pulling of liquid sandwiched between two pistons. As the ink is being stretched, it undergoes a progressive necking (thinning) and subsequent breakup, but there is no clear-cut mark as to when discontinuity or breakup begins but is found to be a function of Webber number, Reynolds number and strain rate [21, 24, 93, 102-104].

In an attempt to model the ink deposition process, Vozzi et al. [55] only considered the applied pressure as the primary driving force, in which case the model failed to accurately predict feature resolution at low flow rates, where other factors like substrate velocity and surface forces may have been influential. One possible explanation for the reported result is that at low flow rates, the substrate may play a significant role in pulling ink out of the deposition nozzle. To validate this hypothesis, we adopt an experimental technique using PDMS ink. This was accomplished by measuring flow rates through a 10μm nozzle at different speeds of the substrate. The printing process was carried out using a custom-made 3D microextrusion printer, which has a 50nm resolution for the three axes (Figure 3.13). The experimental condition is presented in Table 3.4, while the printing process and the plot of flow rate as a function of printing speed are shown in Figure 3.14a,b. Each data point is an average of the measured flow rates from four trials. The flow

rate was measured by weighing the mass of printed ink using an electronic balance which has a 10^{-6}g resolution and dividing it by the printed time.

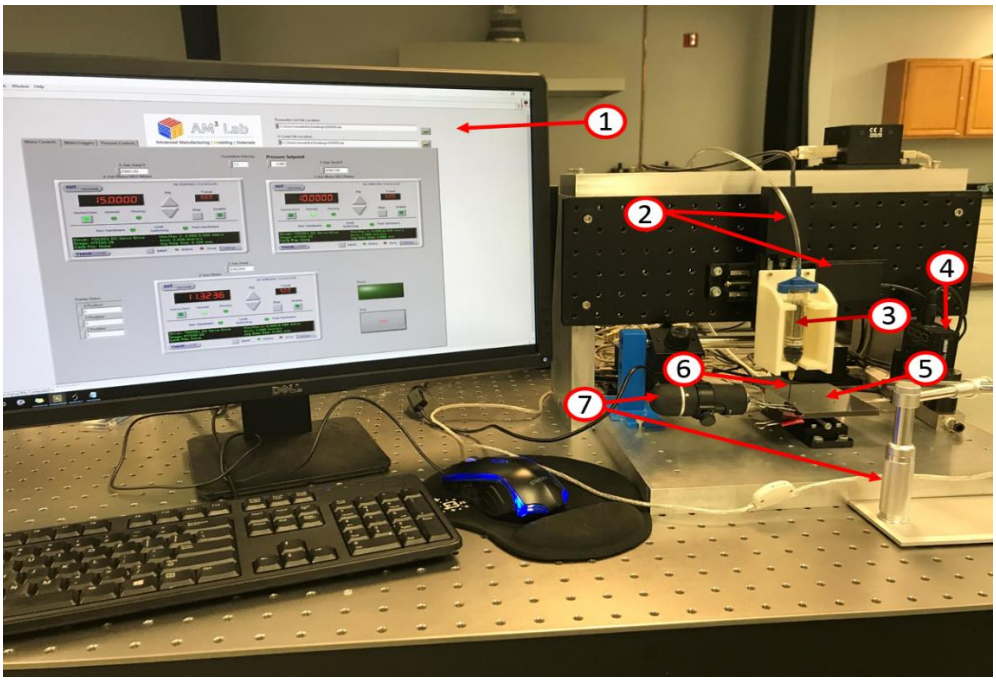

Figure 3.13: Microextrusion printer used for the experimental validation: (1) Control software, (2) XZ translation motors, (3) Syringe barrel, (4) Digital pressure regulator, (5) Printbed, (6) Micronozzle (7) Vision system.

Table 3.4: Experimental conditions for the effects of translating substrate experiment

Ink	Viscosity (cP)	Standoff distance	Applied pressure	Substrate speed
PDMS (part A)	5100	~10 µm	1 psi	0-0.075mm/s

The most important point revealed Figure 3.14c is the flow rate – substrate speed dependence. This validates our hypothesis that if the substrate's speed exceeds the ink flow rate, then ink is drawn out of the nozzle by the translating substrate. The dotted horizontal line represents experimentally determined flow rate at zero substrate speed. Clearly, the flow rate increased from 0.164 to 0.254pL/s (~55.1%) as the substrate speed was increased from 0 to 75µm/s, which agrees

with our hypothesis. The experimentally determined flow rate due to pressure alone (0.164pL/s) is also in close agreement with the theoretically predicted value based on Eq. 3.4 (0.166pL/s). The difference between the two values is 0.019pL/s (~1.2%), indicating the experimentally determined flow rates are reliable. A line of best fit applied to the result reveals the flow rate changes linearly with substrate speed. This result holds important implication for μEP, that is, if a very viscous material needs to be printed but the pressure is limited, the deposition process can be driven by a combination of the extrusion pressure and substrate speed.

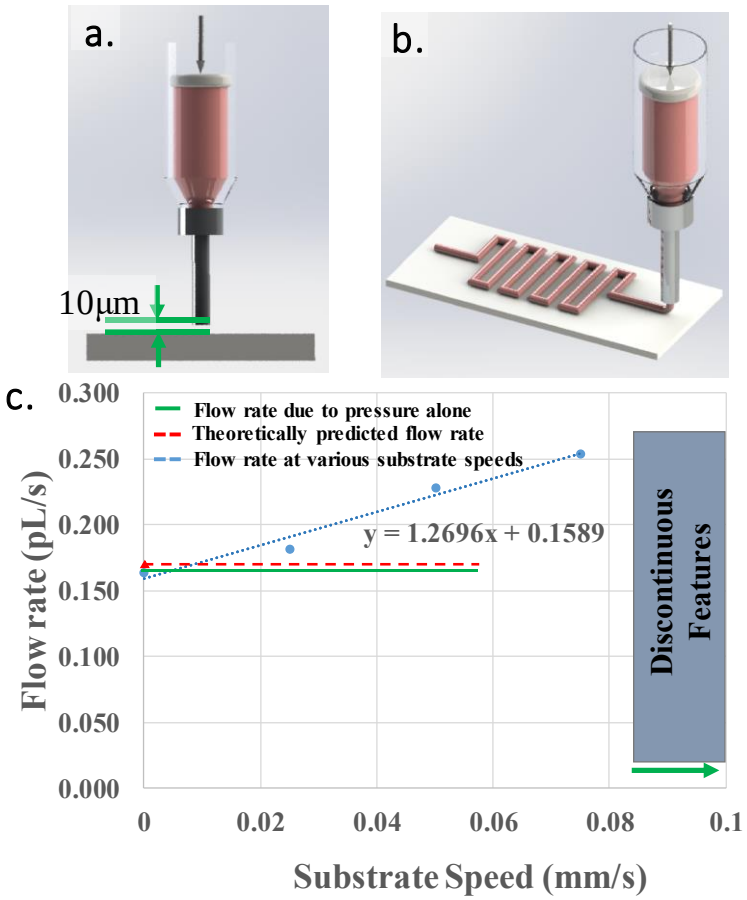

Figure 3.14: Schematic illustration of the microextrusion printing process (a) Standoff distance measurement, (b) Patterned hairpin structure on a glass substrate, and (c) Measured flow rate as a function of substrate speed. Each data point is the average of four different experimental tests.

3.2.4 Phase 4 (P_4): Time-Dependent Shape Retention

Our objective in this region is to capture the time-bound wetting and drying dynamics of the printed ink filament. It involves the transition from the time that the filament initially contacts the substrate to the time it hardens to maintain the final shape. Guided by the critical factors in Eq. 3.1, we examine the applicable models for predicting the final shape and resolution of the printed filament. First, in section 2.4.1, the contact angle, which provides a quantitative estimate of the interaction between the ink, the ambient air around it, and the surface properties of the substrate are discussed. Next, quantitative models for predicting the print resolution are presented in section 3.4.2.1.

3.2.4.1 Contact Angle

In μEP, feature dimensions, geometry, adhesion to the substrate, and the drying rate can be directly inferred from the surface energy interactions between the ink and the substrate, as well as the prevailing ambient condition. This relationship is usually characterized by the static contact angle.

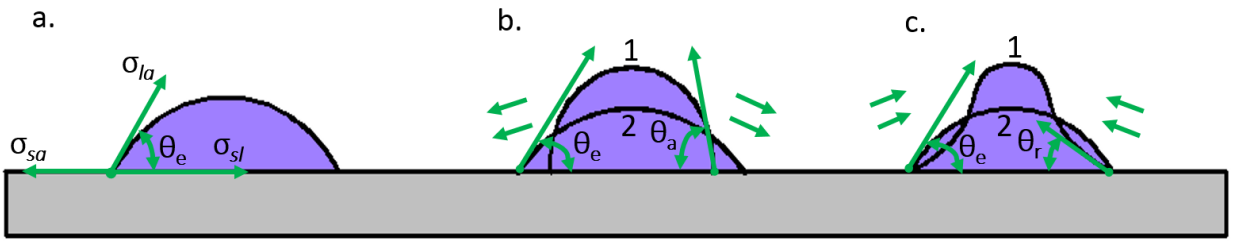

Figure 3.15: Schematic illustration of ink-substrate interaction – (a) Equilibrium contact angle, (b) Advancing contact angle, (c) Receding contact angle.

According to Young's equation (for an ideal surface), the wetting characteristics relating the surface energy to the equilibrium contact angle where the three phases are in mechanical equilibrium with each other is given by (Figure 3.15a) [105, 106]:

$$\sigma_{sa} = \sigma_{sl} + \sigma_{la}\cos\theta_e \tag{3.18}$$

Where σ_{sa}, σ_{sl}, and σ_{la} represents the interfacial energy between the substrate and air, the substrate and liquid, and liquid and air respectively. As a rule of thumb, for substrates with high surface energy relative to the ink (e.g., metal or ceramic substrates), there is usually extensive spreading. Conversely, low energy substrates (e.g., polymer substrates) usually experience less spreading [21, 57, 107].

Unlike on ideal surfaces, there exist many metastable states on real surfaces resulting from surface imperfections (e.g., surface roughness or inhomogeneity), which leads to contact angle hysteresis. Two additional contact angles are used to characterize this phenomenon, advancing contact angle θ_a and receding contact angle θ_r. Advancing contact angle θ_a, as illustrated in Figure 3.15(b), refers to the critical contact angle when the contact line starts to advance as the contact angle increases. Receding contact angle θ_r, as illustrated in Figure 3.15(c), refers to the critical contact angle when the contact line starts to recede as the contact angle decreases.

3.2.4.2 Feature Predictive Models

Models for predicting feature width (W) and height (H) are usually derived by assuming the extruded filament have a cylindrical diameter (D_f) comparable to the dispensing nozzle tip (D_t) (Figure 3.16a). On this path, several attempts have been made to develop a single model that incorporates all the significant variables for predicting feature dimensions [24, 94]. For example,

Khalil and Sun [24] developed a model to predict the diameter of non-Newtonian polymer ink expressed as:

$$D_f = \sqrt{\frac{4Q}{\pi u}} = 2\sqrt{\frac{\left(\frac{n}{3n+1}\right)\dot{\gamma}_o^{\frac{n+1}{n}}\left(\frac{\partial P}{2\mu_o}\right)^{1/n} R^{\frac{3n+1}{n}}}{u}} \tag{3.19}$$

The parameters in this equation were previously defined in Eq. 3.4. The major limitation of this model is that the surface energy interaction was not considered. To overcome this setback, Jin et al.[94] studied the extrudability of various concentration of biocompatible N-isopropylacrylamide (NIPAAm) ink and developed a model to predict the filament radius (Figure 3.16):

$$R_f = \sqrt{\frac{\pi v}{(4\theta - 2\sin 2\theta)u}} D_f \tag{3.20}$$

Where D_f is the initial filament diameter, and R_f describes the radius of the elliptical arc cross-sectional area after wetting has taken place.

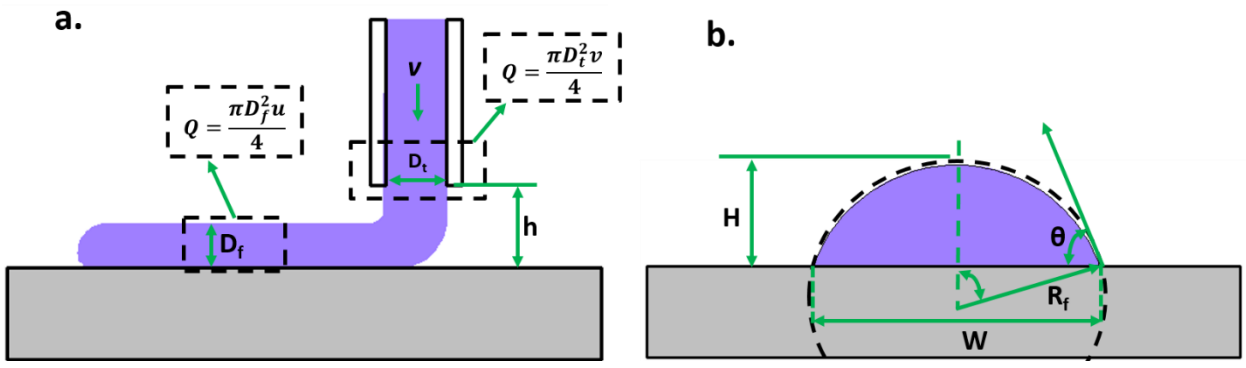

Figure 3.16: Schematic illustration of the ink deposition process- (a) Side view of the ink deposition process, (b) Front view showing time-dependent filament-substrate interaction and shape retention.

Holistically, as revealed in Eq. 3.20, the final filament radius increases with increased extrusion velocity and nozzle diameter and decreases as the contact angle and substrate velocity are increased. It is easily seen that if the substrate velocity is low relative to the extrusion velocity (i.e., *u/v*), this will result in over deposition, which will lead to the increase of the contact angle until it reaches the advancing contact angle θ_a. If the inertial energy of the spreading is not fully dissipated after the spreading has reached its maximum extent, the contact angle will start to reduce until it reaches the receding contact angle θ_r and the filament will start to recede. Receding may also be induced by volume shrinkage due to solvent evaporation [52, 108, 109]. Appropriate contact angle (i.e., θ_r, or θ, or θ_a) shall be used in Eq. 3.20 to determine the final printing resolution, depending on the scenario.

Towards limiting the excessive ink spreading, there are three primary methods of controlling the shape and resolution of the prints: (1) Treating the substrate with hydrophobic materials to create a low energy surface will limit excessive spreading of low surface energy inks; (2) As reported by Liang et al. [107] using highly viscous inks in place of surface modification of the substrate will generally yield better output than substrate treatment, as this will lower the ink spreading rate; (3) Faster drying rates (and by effect improved resolution) may be achieved by using a porous substrate to provide additional channels to drive out the solvent, or heating. However, heating the substrates should be done cautiously because a fast-drying rate can result in cracking, warping and delamination of the printed structures [57].

III. APPLICATION

To demonstrate the usefulness of the presented framework in section II, we will provide a case study of achieving µEP of high-resolution features using Sylgard 184, (hereafter referred to

as PDMS) ink based on knowledge gained from this framework. In section 3.1 we discuss the rationale for choosing PDMS as the material for this demonstration and present the results and discussions in section 3.2.

3.3.1 Materials and Methods

The biocompatibility, optical transparency, and tunable mechanical properties of polydimethylsiloxane (PDMS) have led to a growing demand for high-resolution, and low-cost patterning methods for PDMS based structures. Such structures have widespread applications including biosensors [110], general cell study (e.g., DNA and proteins) self-assembled monolayers (SAMs)[111, 112], and wearable electronics[113]. While soft lithography has been well-developed for creating patterns from this "mechanically soft materials", the need for making masks, usage of cleanroom equipment, and long process cycles make it costly. Extrusion-based printing technique provides an alternative solution for making PDMS structures. However, its adoption has been hindered due to: (1) the poor resolution of commercial 3D printers, and (2) the lack of ideal PDMS printing properties. To circumvent this second problem, several variants of this printing technique have been tested in order to improve print resolution and fidelity. For example, one approach prints PDMS within a support bath; thus, providing the needed mechanical support to hold the structure in place until it is cured and is subsequently removed. However, a drawback of this technique is that the interfacial interactions between the support bath materials and the PDMS could influence the morphology of the printed structures, and several difficulties are experienced during removal from the support material [114]. Using this approach, features resolution ~100-260μm have been achieved [31, 114]. To offer a low-cost PDMS printing platform, Structur3D Printing company came up with the Discov3ry Paste Extruder, as a universal add-on for commercial FDM printers, but this system is better suited for printing mesoscale

structures (~250μm)[115]. Still, several applications require PDMS patterns in the micrometer length scale, and to our knowledge, this is yet to be demonstrated by any 3D printing approach.

Herein, we demonstrate the viability of μEP to pattern microscale PDMS features with two objectives. First, to overcome the limitations arising from the non-ideal ink property, we developed an empirical model to predict viscosity-time relationship, which is used to adjust the printing process parameters in order to overcome capillary rise effect and surface wetting. Second, to improve printing resolution, alleviate the fabrication challenges, and lower the cost of patterning high-resolution PDMS, we employed a custom-made μEP developed in our group. We demonstrate this strategy using PDMS (Dow Corning), which is the commonly used PDMS for soft-lithography processes, and for making biomedical templates [116]. The PDMS ink was prepared by mixing a 10:1 ratio of part A (base) and B (curing agent) respectively; and subsequently degassed to eliminate air bubbles. The air-free mixture was then utilized for both the rheological characterization and microextrusion printing. In the sections following, we will discuss the stepwise approach to achieving a target feature resolution of ~10μm. Throughout this section, a 5μm nozzle size will be applied.

3.3.2 Results and Discussions

In this section, we present the results of the printing process guided by the four phases established in the presented framework. For this demonstrative application, simple planar, and 2D grid structures are printed.

3.3.2.1 Phase 1: Ink Flow Behavior

The PDMS is a two-part liquid that exhibits a modest viscosity at room temperature. However, once mixed it undergoes gelation over time (under ambient conditions), and viscosity

increases by several orders of magnitude, which dictates printability. In order to effectively use this material for μEP, we needed a means of predicting the rate at which viscosity changes over time. For this reason, we sought to develop a model to predict the viscosity-time relationship. We measured the rheological properties of this ink using a rheometer (Brookfield DV3T LV). First, to reveal any shear rate dependence, ink viscosity was characterized at a controlled shear rate mode ranging from 0.034 to 2.04s^{-1}. To reduce variability in the measurement results a single point averaged value for each set of condition was obtained over a 2-minute period. Second, to capture any possible time-dependent property, six different measurements, at each shear rate was performed at 30 minutes intervals. All measurements were done at 24.2°C. From this data, the ink flow behavior is identified and presented in Figure 3.17.

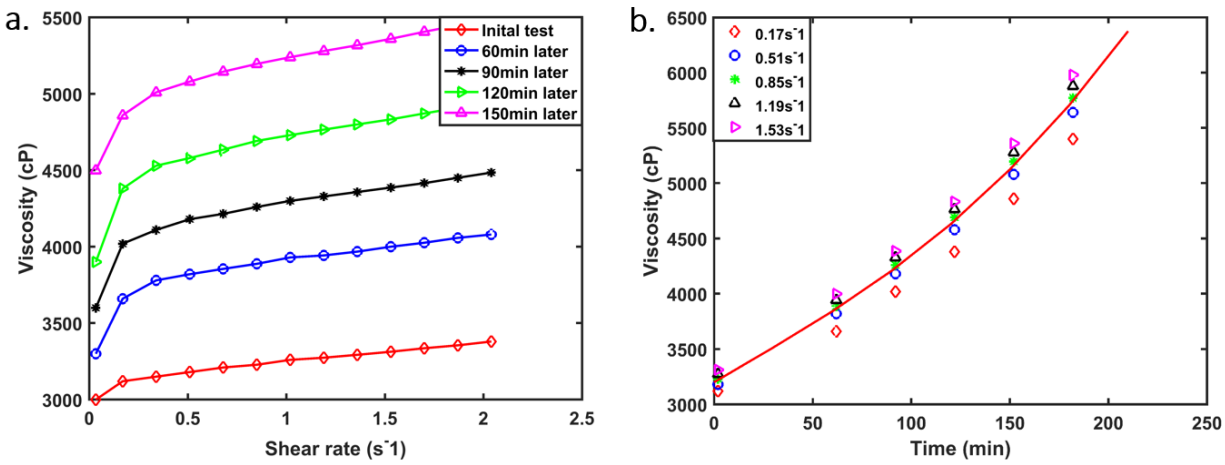

Figure 3.17: Viscosity of PDMS as a - (a) function of the shear rate for 30 minutes time steps (b) function of curing time for different shear rates, at Temp. of 24.2°C. The points refer to experimental data and the solid line represents the model.

As shown in Figure 3.17(a), the ink displays a slight increase in viscosity with increasing shear rate. For instance, as the shear rate increased from 0.17 to 1.53s^{-1}, the viscosity increased by 6.19%, as opposed to 800% increase in shear rate (Table 3.5). Interestingly, within the range of tested shear rate, the viscosity was observed to be almost independent of shear rate, implying a

Newtonian flow behavior (Figure 3.17a), which agrees with the finding by Schneider et al. [117]. Next, given the possibility of the dependence of viscosity on time, we then sought to quantify this relationship, and Figure 3.17(b) confirms a clear rheopectic behavior (i.e., a time-dependent shear thickening). For instance, at a shear rate of $0.170s^{-1}$, the viscosity increased by ~73% over 180 min., which is far greater than the influence due to shear rate (Table **3.6**).

This flow behavior has several implications for μEP: (1) the viscosity increases continuously throughout the printing process, (2) a constant value of viscosity cannot be used to predict flow rate, (and hence feature resolution), (3) for long printing times, the deposition pressure needs to be constantly increased in order to achieve a constant flow rate. Recognizing this significant viscosity-time dependence, and the prospect of achieving stable structures, we developed a model (based on Figure 3.17b) for predicting ink viscosity as a function of time. The 4th-degree polynomial interpolation below describes the viscosity-time relationship. A 4th degree polynomial was used since it provides a better fit for the data points.

$$\mu(t) = 3202 + 10.5t - 5.43x10^{-3}t^2 + 1.73x10^{-4}t^3 - 1.79x10^{-7}t^4 \qquad (2.21)$$

Table 3.5: The estimated increasing rate of viscosity as a function of shear rate

Shear	Viscosity (cP)	% increase in viscosity
0.17	3120	-
0.51	3180	1.9
1.19	3274	4.94
1.53	3313	6.19

Table 3.6: The estimated increasing rate of viscosity as a function of time

Time (min)	Viscosity (cP)	% increase in viscosity
2	3120	-
90	4020	28.84
120	4380	40.38
180	5400	73.08

This model based on averaged experimental data was found to accurately approximate ink viscosity, for the range of shear rates studied here. For very short printing times, the terms with higher powers of t tend to zero, and viscosity may be considered relatively constant. Under this condition using Eq.3.3 (with t= 5 min., D=5μm, L=3mm, ΔP =100psi) the flow rate was calculated to be (Q) ≈ 17.3pl/s.

3.3.2.2 Phase 2: Capillary Rise and Evaporative Effect

One of the primary objectives for viscosity pre-calibration carried out in section 3.2.1 was to increase the PDMS viscosity, and hence limit the degree of the capillary effect. To achieve this, we allowed ample time (7 hours) for the ink to cure, during which viscosity increased from 3202 to 13679cP (~4.3-fold increase). Under this condition, the ink rheology changed from liquid to gel-like behavior. The capillary number (Ca) was computed to be 9.1×10^{-6} (using σ =19.8 mN/m[118], v =1.31×10^{-7}mm/s, μ =13,679cP) which is far less than the threshold value predicted by our theory. As the theory predicts, with ink of low viscosity and low surface energy if the nozzle has a higher surface energy than the ink, and $Ca < 10^{-1}$ then the ink may wet the nozzle surface, giving rise to high capillary effect.

Evidently, the large increase in viscosity reduced excessive capillary effect but did not eliminate the effects as obvious from the capillary number. To overcome any possible capillary effect, it became clear that consistent and reproducible features could be obtained by carefully

bringing the nozzle tip close to the substrate (with a standoff distance of 5**µ**m) so that the dispensed ink directly contacts the substrate once it exits the nozzle tip and is drawn along the substrate. At the printing condition (i.e., T = 24^{o}) it took about 10 hours for the ink to not be extrudable while the flow timescale, t_{flow} is~18.6s. This means a small flow timescale relative to the curing timescale. Therefore, we do not expect rapid curing to become a problem. However, in the preliminary experiment it was realized that if a heated substrate was employed, ink curing time reduced drastically leading to clogging of the nozzle tip. Therefore, to avoid clogging, heating was not employed for this test since heating will shorten the evaporation timescale.

3.3.2.3 Phase 3: Standoff Distance and Printing Speed

Guided by our framework, we started out with the same standoff distance as the nozzle diameter (i.e., h =5µm) which was observed to give consistent extrusion. The nozzle-substrate alignment process was carried with the aid of a microscope. With an estimated flow rate of 2.63fL/s, using Eq.3.18 (i.e., u_c =Q/D*h), the theoretical critical printing speed was calculated to be ~0.126µms^{-1}. Using this value and 5µm standoff distance, the printer was then operated in an automatic mode to sequentially execute the scripted g-code, while varying the printing speed until the minimum line width was obtained.

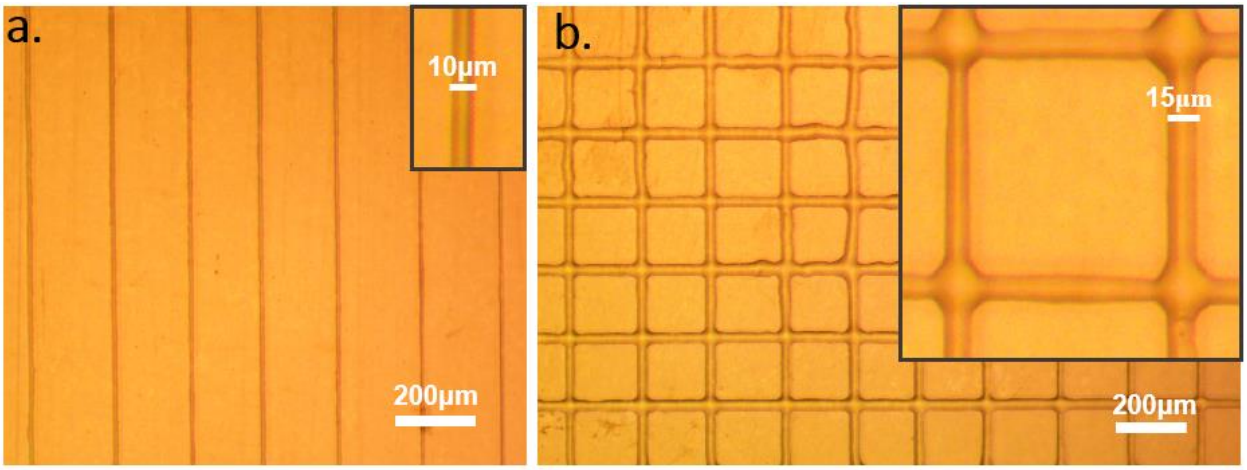

Figure 3.18: (a) Photomicrographs of micro-patterns patterns on PET substrate (a) Planar array of patterned PDMS with 200μm center-to-center spacing, (b) Square grids of patterned PDMS with a 200μm center-to-center spacing. Printing conditions: 5um nozzle at the 1psi and 0.1mm/s. The inserts show views at higher magnifications and widths of the printed features.

3.3.2.4 Phase 4: Substrate Choice

Based on the interaction between nozzle and substrate, it is known that a glass substrate has a high surface energy relative to the ink (i.e., $\sigma_{e(glass)}$= 310mN/m, $\sigma_{e(PDMS)}$ = 19.8 mN/m) and would therefore induce a large degree of spreading. For this reason, a PET with a lower surface energy substrate ($\sigma_{e(PET)}$= 41mN/m) was selected for the substrate. After the printing, we cured the samples at room temperature for 24 hours, and the representative results are presented in Figure 3.18.

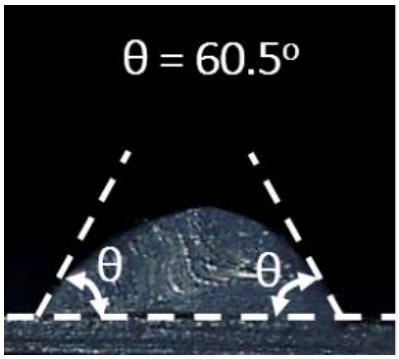

Figure 3.19: Measured contact angle of PDMS on PET substrate.

We patterned planar arrays of the PDMS filaments with a center-to-center spacing of 200μm (Figure 3.18a), 2D square grids (Figure 3.18b). The printed patterns have widths ~10μm (Figure 3.18a). To compare the results with the theoretically predicted value from Eq. 5.1, we measured the contact angle of a printed filament, and the average value is about 60.5^{o} (Figure 3.19). The theoretical filament width (W) was calculated to be 1.15μm, which is about an order of magnitude smaller than the experimental value. This was calculated by assuming that ink is driven by a combination of applied pressure and substrate speed (i.e., v =0.00131mm/s and u = 0.1mm/s). The difference between the theoretically predicted width and the experimental value is attributed to the model assumption that the initial filament geometry was cylindrical and equal to the nozzle diameter.

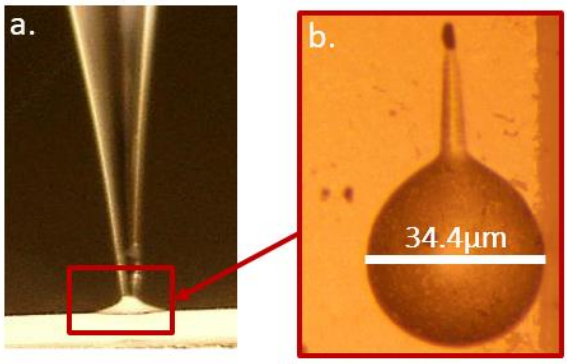

Figure 3.20: (a) Photomicrograph of meniscus formation at the nozzle tip, (b) Top view - high-resolution image showing the initial diameter of the meniscus formed the tip.

Contrary to this assumption, Figure 3.20 reveals that the initial ink meniscus is far from being cylindrical but in the shape of a spherical cap having a diameter several times bigger than the nozzle diameter (~34.4μm). Depending on the scenario, the diameter can increase significantly if there is a time delay between when the ink meniscus is formed and initiation of the printing process due to over deposition and forced flow. In the preliminary experiments, it became evident that consistent and reproducible features were obtained by carefully synchronizing the formation of the

ink meniscus and the start of the printing. Hence, by using the diameter of the ink meniscus (i.e., 34.4μm) in Eq. 5.1 gives the filament width to be ~7.92μm which is in close range to the experimental value (~10 μm). Therefore, once the geometric profile of the initial ink filament is known, this equation may be used to predict the filament resolution.

IV. CONCLUSIONS AND FUTURE OUTLOOK

This paper was motivated by the lack of comprehensive understanding of the dynamic intricacies that underscore successful microextrusion printing and was therefore aimed at providing the requisite knowledge base needed for adapting μEP for microfabrication. Ultimately, this understanding and control of the various materials and process parameters dictate the resolution and quality of the printed features. This printing techniques drastically simplifies the fabrication of arbitrary structures, and a wide range of choices in materials and substrates, when compared to the classical photolithography techniques. It is our hope that the developed framework will spur interests in adapting microextrusion printing for yet to be printed materials and applications.

Overall, we set out to investigate four important question:

(1) What are the ink properties that determine printability, and shape retention characteristics?

Figure 3b reveals that the ideal ink for μEP must satisfy several criteria including ability to flow easily through fine needles when subjected to a shear force, good shape retaining ability after extrusion and self-supportability, which are readily satisfied by shear thinning inks with high viscoelastic properties. This conclusion is important because shear thinning inks can be used to maximize flow rate through micronozzles and enable shape retention. Based on our experimental test in section 2.2.1, we demonstrated that a low viscosity ink printed at low flow rate is susceptible to nozzle wetting and capillary rise, and hence poor feature resolution.

Aided by the results of the test, we proposed that the capillary number (Eq. 11) may be used to determine the appropriate working range for a given ink viscosity, flow velocity, and surface tension.

(2) *What are the dominant driving forces that govern ink extrusion at the microscale?* Regarding this question, Eq.3.3 -Eq. 3.5 revealed that ink viscosity and nozzle geometric characteristics (particularly the tip diameter and cone-half angle) are the primary parameters affecting flow rates. Furthermore, evidence from the literature indicates that the capillary pressure may become an effective way to drive ink flow in micronozzles (Eq. 3.7), while the surface tension at the nozzle exit resists the ink from exiting the nozzle (Eq. 3.10) and represents a significant barrier to further improving print resolution.

(3) *What are the major factors that determine the final resolution of printed tracks?* The impacts of three significant process parameters (e.g., standoff distance, substrate speed, and substrate surface property) on feature resolution were identified in the literature. The finding is that high standoff distance or high substrate speed can result in discontinuous features, while a small standoff distance or low printing speed can result in forced spreading and over deposition respectively. Eq. 3.17 and 3.18 are proposed to guide the selection of the optimum standoff distance and substrate speed. The substrate surface property is characterized mainly by the advancing and receding contact angles, which play a significant role in determining the final printing resolution.

(4) *How do we modulate these factors to meet the requirements of target applications?* At each phase of the printing process, we provided tools which may be employed to circumvent the various barriers to successful printing. To buttress this point, the knowledge gained from the framework was employed in a case study to demonstrate a stepwise guide on how the various

parameters may be controlled to achieve high-resolution features. For example, in section 2.4 (see Figure 18) we showed, for the first time, high-resolution printing of PDMS features in ambient condition with resolution down to ~10μm. All the experiments were performed in ambient condition with no heating.

Despite the progress that has been made, there are many opportunities for improvements for μEP, including better understanding and control of tool pathways, the need for more precise ink flow prediction to fabricate more sophisticated geometries. The drive for finer feature sizes sacrifices the printing speeds and improving printing speed could facilitate widespread adoption of this patterning technique. Further development and exploration of novel materials with requisite properties are at the center of furthering this printing technology.

3.4 Acknowledgments

We are thankful to our colleagues at the AM^3 Lab for providing support and enabling environment for this work. We gratefully acknowledge the financial support from the University of Arkansas, through the startup fund provided by the Vice Provost Office for Research and Economic Development. Any opinions, findings, and conclusions or recommendations expressed in this publication are those of the authors and do not necessarily reflect the views of the University of Arkansas.

Nomenclature

A	Cross-sectional area of the filament	Re	Reynolds number
c	Vapor concentration	R_f	Filament radius
Ca	Capillary number	t	Time
D	Nozzle diameter	t_{evap}	Evaporation timescale
D_i	Nozzle inlet diameter	t_{flow}	Flow timescale
D_f	Filament diameter	T	Temperature
D_t	Nozzle tip diameter	u	Substrate velocity
h	Standoff distance	v	Ink flow velocity
h_c	Critical standoff distance	V	nk volume
H	Thickness of filament	W	Filament width
I	Evaporation rate	μ	Shear rate
J	Vapor diffusivity	$\boldsymbol{\mu}$	Ink viscosity
L	Nozzle length	$\boldsymbol{\rho}$	Fluid density
m	Mass of ink	$\boldsymbol{\sigma}$	Surface tension
n	Ink flow index	σ_{sa}	Surface energy between substrate & air
p	Externally applied pressure	σ_{sl}	Surface energy between substrate & ink
P_c	Capillary pressure	σ_{la}	Surface energy between ink & air
P_{nw}	Pressure in nonwetting phase	$\boldsymbol{\theta}$	Contact angle
P_w	Pressure in nonwetting phase	θ_a	Advancing contact angle
Q	Flow rate	θ_e	Equilibrium contact angle
r_d	Droplet radius	θ_r	Receding contact angle
R	Nozzle radius	$\boldsymbol{\tau}$	Shear stress

3.5 References

[1] Hsu, T., 2002, "Miniaturization–A paradigm shift in advanced manufacturing and education," International conference on Advanced Manufacturing Technologies and Education in the 21st Century, Anonymous .

[2] Ikuta, K., Hirowatari, K., and Ogata, T., 1994, "Three dimensional micro integrated fluid systems (MIFS) fabricated by stereo lithography," Micro Electromechanical Systems, 1994, MEMS'94, Proceedings, IEEE Workshop on, Anonymous IEEE, pp. 1-6.

[3] Sun, K., Wei, T., Ahn, B. Y., 2013, "3D Printing of Interdigitated Li-ion Microbattery Architectures," Advanced Materials, 25(33) pp. 4539-4543.

[4] Cohrs, N. H., Petrou, A., Loepfe, M., "A Soft Total Artificial Heart—First Concept Evaluation on a Hybrid Mock Circulation," Artificial Organs, pp. n/a-n/a.

[5] Chou, H. P., Spence, C., Scherer, A., 1999, "A Microfabricated Device for Sizing and Sorting DNA Molecules," Proceedings of the National Academy of Sciences of the United States of America, 96(1) pp. 11-13.

[6] Dario, P., Carrozza, M. C., Benvenuto, A., 2000, "Micro-Systems in Biomedical Applications," Journal of Micromechanics and Microengineering, 10(2) pp. 235.

[7] Kim, B., Lee, J., Gao, G., 2017, "Direct 3D Cell-Printing of Human Skin with Functional Transwell System," BIOFABRICATION, 9(2) pp. 025034.

[8] Hansen, C. J., Wu, W., Toohey, K. S., 2009, "Self-Healing Materials with Interpenetrating Microvascular Networks," Advanced Materials, 21(41) pp. 4143-4147.

[9] Chabinyc, M. L., Chiu, D. T., McDonald, J. C., 2001, "An Integrated Fluorescence Detection System in Poly (Dimethylsiloxane) for Microfluidic Applications," Analytical Chemistry, 73(18) pp. 4491-4498.

[10] Weigl, B. H., and Yager, P., 1999, "Microfluidic Diffusion-Based Separation and Detection," Science, 283(5400) pp. 346-347.

[11] Anderson, J. R., Chiu, D. T., Jackman, R. J., 2000, "Fabrication of Topologically Complex Three-Dimensional Microfluidic Systems in PDMS by Rapid Prototyping," Analytical Chemistry, 72(14) pp. 3158-3164.

[12] Ahn, B. Y., Duoss, E. B., Motala, M. J., 2009, "Omnidirectional Printing of Flexible, Stretchable, and Spanning Silver Microelectrodes," Science (New York, N.Y.), 323(5921) pp. 1590-1593.

[13] Kim, J. T., Seol, S. K., Pyo, J., 2011, "Three-Dimensional Writing of Conducting Polymer Nanowire Arrays by Meniscus-Guided Polymerization," Advanced Materials, 23(17) pp. 1968-1970.

[14] Sirringhaus, H., Kawase, T., Friend, R. H., 2000, "High-Resolution Inkjet Printing of all-Polymer Transistor Circuits," Science (New York, N.Y.), 290(5499) pp. 2123-2126.
[15] Gibson, I., Rosen, D.W., and Stucker, B., 2010, "Additive manufacturing technologies," Springer.

[16] ISO/ASTM 52900, "Https://www.Iso.org/obp/ui/#iso:Std:74514:En," .
[17] Murphy, S., and Atala, A., 2014, "3D Bioprinting of Tissues and Organs," Nature Biotechnology, 32(8) pp. 773-785.

[18] Sirringhaus, H., Kawase, T., Friend, R. H., 2000, "High-Resolution Inkjet Printing of all-Polymer Transistor Circuits," Science (New York, N.Y.), 290(5499) pp. 2123-2126.

[19] Barton, K., Mishra, S., Shorter, K. A., 2010, "A Desktop Electrohydrodynamic Jet Printing System," Mechatronics, 20(5) pp. 611-616.

[20] Kadara, R. O., Jenkinson, N., Li, B., 2008, "Manufacturing Electrochemical Platforms: Direct-Write Dispensing Versus Screen Printing," Electrochemistry Communications, 10(10) pp. 1517-1519.

[21] Wang, J., and Shaw, L. L., 2005, "Rheological and Extrusion Behavior of Dental Porcelain Slurries for Rapid Prototyping Applications," Materials Science and Engineering: A, 397(1) pp. 314-321.

[22] Lewis, J. A., and Gratson, G. M., 2004, "Direct Writing in Three Dimensions," Materials Today, 7(7) pp. 32-39.

[23] Therriault, D., Shepherd, R. F., White, S. R., 2005, "Fugitive Inks for Direct-Write Assembly of Three-Dimensional Microvascular Networks," Advanced Materials, 17(4) pp. 395-399.

[24] Khalil, S., and Sun, W., 2007, "Biopolymer Deposition for Freeform Fabrication of Hydrogel Tissue Constructs," Materials Science and Engineering: C, 27(3) pp. 469-478.

[25] Vozzi, G., Flaim, C., Ahluwalia, A., 2003, "Fabrication of PLGA Scaffolds using Soft Lithography and Microsyringe Deposition," Biomaterials, 24(14) pp. 2533-2540.

[26] Vozzi, G., Previti, A., De Rossi, D., 2002, "Microsyringe-Based Deposition of Two-Dimensional and Three-Dimensional Polymer Scaffolds with a Well-Defined Geometry for Application to Tissue Engineering," Tissue Engineering, 8(6) pp. 1089-1098.

[27] Schaffner, M., Ruhs, P. A., Coulter, F., 2017, "3D Printing of Bacteria into Functional Complex Materials," Science Advances, 3(12) .

[28] Schuurman, W., Levett, P., Pot, M., 2013, "Gelatin-Methacrylamide Hydrogels as Potential Biomaterials for Fabrication of Tissue-Engineered Cartilage Constructs," Macromolecular Bioscience, 13(5) pp. 551-561.

[29] Kang, H., Lee, S., Ko, I., 2016, "A 3D Bioprinting System to Produce Human-Scale Tissue Constructs with Structural Integrity," Nature Biotechnology, 34(3) pp. 312-312.

[30] Jin, Y., Plott, J., and Shih, A., 2015, "Extrusion-based additive manufacturing of the moisture-cured silicone elastomer," Proc. Solid Free. Fabr. Symp, pp. 308-318.

[31] Bhattacharjee, T., Zehnder, S. M., Rowe, K. G., 2015, "Writing in the Granular Gel Medium," Science Advances, 1(8) pp. e1500655.

[32] Hinton, T. J., Hudson, A., Pusch, K., 2016, "3D Printing PDMS Elastomer in a Hydrophilic Support Bath Via Freeform Reversible Embedding," Acs Biomaterials Science & Engineering, 2(10) pp. 1781-1786.

[33] Dermanaki-Farahani, R., Lebel, L. L., and Therriault, D., 2014, "Manufacturing of Three-Dimensionally Microstructured Nanocomposites through Microfluidic Infiltration," Journal of Visualized Experiments: JoVE, (85). doi(85) pp. 10.3791/51512.

[34] Sun, K., Wei, T., Ahn, B. Y., 2013, "3D Printing of Interdigitated Li-Ion Microbattery Architectures," Advanced Materials, 25(33) pp. 4539-4543.

[35] Malone, E., Rasa, K., Cohen, D., 2004, "Freeform Fabrication of Zinc-Air Batteries and Electromechanical Assemblies," Rapid Prototyping Journal, 10(1) pp. 58-69.

[36] Kuhn, M., Napporn, T., Meunier, M., 2008, "Direct-Write Microfabrication of Single-Chamber Micro Solid Oxide Fuel Cells," Journal of Micromechanics and Microengineering, 18(1) pp. 015005.

[37] Becerril, H. A., Roberts, M. E., Liu, Z., 2008, "High-Performance Organic Thin-Film Transistors through Solution-Sheared Deposition of Small-Molecule Organic Semiconductors," Advanced Materials, 20(13) pp. 2588-2594.

[38] Dimos, D., King, B., and Yang, P., 1999, "Direct-write fabrication of integrated, multilayer passive components," Advanced Packaging Materials: Processes, Properties and Interfaces, 1999. Proceedings. International Symposium on, Anonymous IEEE, pp. 186-190.

[39] Ahn, B. Y., Lorang, D. J., Duoss, E. B., 2010, "Direct-Write Assembly of Microperiodic Planar and Spanning ITO Microelectrodes," Chemical Communications, 46(38) pp. 7118-7120.

[40] Ahn, B. Y., Duoss, E. B., Motala, M. J., 2009, "Omnidirectional Printing of Flexible, Stretchable, and Spanning Silver Microelectrodes," Science (New York, N.Y.), 323(5921) pp. 1590-1593.

[41] Massa, S., Sakr, M. A., Seo, J., 2017, "Bioprinted 3D Vascularized Tissue Model for Drug Toxicity Analysis," Biomicrofluidics, 11(4) pp. 044109.

[42] Therriault, D., White, S. R., and Lewis, J. A., 2003, "Chaotic Mixing in Three-Dimensional Microvascular Networks Fabricated by Direct-Write Assembly," Nature Materials, 2(4) pp. 265-271.

[43] Wu, W., 2010, "Direct ink writing of microvascular networks," University of Illinois at Urbana-Champaign.

[44] Therriault, D., 2003, "Directed assembly of three-dimensional microvascular networks," .

[45] Risner, J., 2008, "Investigation of dielectric elastomer actuation for printable mechatronics," University of California, Berkeley, .

[46] Muth, J. T., Vogt, D. M., Truby, R. L., 2014, "Embedded 3D Printing of Strain Sensors within Highly Stretchable Elastomers," Advanced Materials, 26(36) pp. 6307-6312.

[47] Lewis, J. A., 2006, "Direct Ink Writing of 3D Functional Materials," Advanced Functional Materials, 16(17) pp. 2193-2204.

[48] Datar, A., 2012, "Micro-extrusion process parameter modeling," Rochester Institute of Technology.

[49] Gleadall, A., Ashcroft, I., and Segal, J., 2018, "VOLCO: A Predictive Model for 3D Printed Microarchitecture," Additive Manufacturing, 21pp. 605-618.

[50] Mason, M. S., Huang, T., Landers, R. G., 2006, "Freeform extrusion of high solids loading ceramic slurries, Part I: Extrusion process modeling," 17th Solid Freeform Fabrication Symposium, SFF 2006, August 14, 2006 - August 16, Anonymous University of Texas at Austin (freeform), Austin, TX, United States, pp. 316-328.

[51] Li, Q., and Lewis, J. A., 2003, "Nanoparticle Inks for Directed Assembly of Three-Dimensional Periodic Structures," Advanced Materials, 15(19) pp. 1639-1643.

[52] Smay, J. E., Cesarano, J., and Lewis, J. A., 2002, "Colloidal Inks for Directed Assembly of 3-D Periodic Structures," Langmuir, 18(14) pp. 5429-5437.

[53] Chang, R., Nam, J., and Sun, W., 2008, "Effects of Dispensing Pressure and Nozzle Diameter on Cell Survival from Solid Freeform fabrication–based Direct Cell Writing," Tissue Engineering Part A, 14(1) pp. 41-48.

[54] Cao, Y., Zhou, L., Wang, X., 2009, "MicroPen Direct-Write Deposition of Polyimide," Microelectronic Engineering, 86(10) pp. 1989-1993.

[55] Vozzi, G., Previti, A., De Rossi, D., 2002, "Microsyringe-Based Deposition of Two-Dimensional and Three-Dimensional Polymer Scaffolds with a Well-Defined Geometry for Application to Tissue Engineering," Tissue Engineering, 8(6) pp. 1089-1098.

[56] Crockett, R. S., and Calvert, P. D., 1996, "The Liquid-to-Solid Transition in Stereodeposition Techniques," Solid Freeform Fabrication Symposium, Anonymous pp. 257-264.

[57] Cesarano, J.,III, Segalman, R., and Calvert, P., 1998, "Robocasting Provides Moldless Fabrication from Slurry Deposition," Ceramic Industry, 148(4) pp. 94-94.

[58] King, B. H., Morissette, S., Denham, H., 1998, "Influence of rheology on deposition behavior of ceramic pastes in direct fabrication systems," Solid Freeform Fabrication Symposium, Anonymous pp. 391-398.

[59] Morissette, S. L., Lewis, J. A., Cesarano, J., 2000, "Solid Freeform Fabrication of Aqueous alumina–poly (Vinyl Alcohol) Gelcasting Suspensions," Journal of the American Ceramic Society, 83(10) pp. 2409-2416.

[60] Vickroy, B., Lorenz, K., and Kelly, W., 2007, "Modeling Shear Damage to Suspended CHO Cells during Cross-Flow Filtration," Biotechnology Progress, 23(1) pp. 194-199.

[61] Gratson, G., and Lewis, J., 2005, "Phase Behavior and Rheological Properties of Polyelectrolyte Inks for Direct-Write Assembly," Langmuir, 21(1) pp. 457-464.

[62] Li, B., Clark, P. A., and Church, K., 2007, "Robust direct-write dispensing tool and solutions for micro/meso-scale manufacturing and packaging," ASME 2007 International Manufacturing Science and Engineering Conference, Anonymous American Society of Mechanical Engineers, pp. 715-721.

[63] Piqué, A., and Chrisey, D.B., 2001, "Direct-write technologies for rapid prototyping applications: sensors, electronics, and integrated power sources," Academic press, .

[64] 2018, "Surface Tension Values of some Common Test Liquids for Surface Energy Analysis Available: ttp://www.Surface-Tension.De/," .

[65] Ahn, B. Y., Walker, S. B., Slimmer, S. C., 2011, "Planar and Three-Dimensional Printing of Conductive Inks," Journal of Visualized Experiments : JoVE, (58). pii: 3189. doi(58) pp. 10.3791/3189.

[66] Nordson EFD, 2017, "Important Safety Information,".

[67] Cao, Y., Zhou, L., Wang, X., 2009, "MicroPen Direct-Write Deposition of Polyimide," Microelectronic Engineering, 86(10) pp. 1989-1993.

[68] Smay, J. E., Cesarano, J., and Lewis, J. A., 2002, "Colloidal Inks for Directed Assembly of 3-D Periodic Structures," Langmuir, 18(14) pp. 5429-5437.

[69] Li, M., Tian, X., Schreyer, D. J., 2011, "Effect of Needle Geometry on Flow Rate and Cell Damage in the dispensing-based Biofabrication Process," Biotechnology Progress, 27(6) pp. 1777-1784.

[70] Lewis, J. A., 2000, "Colloidal Processing of Ceramics," Journal of the American Ceramic Society, 83(10) pp. 2341-2359.

[71] Smay, J. E., Gratson, G. M., Shepherd, R. F., 2002, "Directed Colloidal Assembly of 3D Periodic Structures," Advanced Materials, 14(18) pp. 1279-1283.

[72] Malda, J., Visser, J., Melchels, F. P., 2013, "25th Anniversary Article: Engineering Hydrogels for Biofabrication," Advanced Materials, 25(36) pp. 5011-5028.

[73] Martanto, W., Baisch, S. M., Costner, E. A., 2005, "Fluid Dynamics in Conically Tapered Microneedles," AIChE Journal, 51(6) pp. 1599-1607.

[74] Li, M.,2010, "Modeling of the Dispensing-Based Tissue Scaffold Fabrication Processes".

[75] Washburn, E. W., 1921, "The Dynamics of Capillary Flow," Physical Review, 17(3) pp. 273.

[76] Stone, H. A., and Kim, S., 2001, "Microfluidics: Basic Issues, Applications, and Challenges," AIChE Journal, 47(6) pp. 1250-1254.

[77] Weislogel, M.M., Feb 01, 1996, "Steady Capillary Driven Flow," NASA Lewis Research Center, OH, United States.

[78] Fanchi, J.R., 2000, "Integrated flow modeling," Elsevier, New York; Amsterdam, .

[79] Chang, B., Nave, G., and Jung, S., 2012, "Drop Formation from a Wettable Nozzle," Communications in Nonlinear Science and Numerical Simulation, 17(5) pp. 2045-2051.

[80] Chen, X., Li, M., and Ke, H., 2008, "Modeling of the Flow Rate in the Dispensing-Based Process for Fabricating Tissue Scaffolds," Journal of Manufacturing Science and Engineering-Transactions of the ASME, 130(2) pp. 21003.

[81] Wang, Y., 2016, "Capillarity and Wetting of Non-Newtonian Droplets. Available at: http://urn.Kb.se/resolve?urn=urn:Nbn:Se:Kth:Diva-184146,".

[82] Osti, G., Wolf, F., and Philippi, P., 2009, "Spreading of liquid drops on acrylic surfaces," Proceedings of the 20th International Congress of Mechanical Engineering, International Congress of Mechanical Engineering, Gramado, RS, Brazil, Anonymous .

[83] Duez, C., Ybert, C., Clanet, C., 2009, "Beating the Teapot Effect," ArXiv Preprint arXiv:0910.3306.

[84] Vozzi, G., Previti, A., De Rossi, D., 2002, "Microsyringe-Based Deposition of Two-Dimensional and Three-Dimensional Polymer Scaffolds with a Well-Defined Geometry for Application to Tissue Engineering," Tissue Engineering, 8(6) pp. 1089-1098.

[85] Kim, J. H., Chang, W. S., Kim, D., 2015, "3D Printing of Reduced Graphene Oxide Nanowires," Advanced Materials, 27(1) pp. 157-161.

[86] Kim, J. T., Seol, S. K., Pyo, J., 2011, "Three-Dimensional Writing of Conducting Polymer Nanowire Arrays by Meniscus-Guided Polymerization," Advanced Materials, 23(17) pp. 1968-1970.

[87] Birdi, K., VU, D., and Winter, A., 1989, "A Study of the Evaporation Rates of Small Water Drops Placed on a Solid-Surface," Journal of Physical Chemistry, 93(9) pp. 3702-3703.

[88] Hu, H., and Larson, R. G., 2002, "Evaporation of a Sessile Droplet on a Substrate," The Journal of Physical Chemistry B, 106(6) pp. 1334-1344.

[89] Jin, Y., Compaan, A., Bhattacharjee, T., 2016, "Granular Gel Support-Enabled Extrusion of Three-Dimensional Alginate and Cellular Structures," Biofabrication, 8(2) pp. 025016.

[90] Li, B., Clark, P. A., and Church, K., 2007, "Robust direct-write dispensing tool and solutions for micro/meso-scale manufacturing and packaging," ASME 2007 International Manufacturing Science and Engineering Conference, Anonymous American Society of Mechanical Engineers, pp. 715-721.

[91] Church, K. H., Chen, X., Goldfarb, J. M., 2014, "Advanced Printing for Microelectronic Packaging," Submitted for Publication in IPC APEX Expo.

[92] Stanley, M., 1995, "Modeling Axisymmetric Flows Dynamics of Films, Jets, and Drops," Academic Press, San Diego.

[93] Liang, R., and Mackley, M., 1994, "Rheological Characterization of the Time and Strain Dependence for Polyisobutylene Solutions," Journal of Non-Newtonian Fluid Mechanics, 52(3) pp. 387-405.

[94] Jin, Y., Zhao, Z., Danyang, and Huang, Y., 2018, "Study of Extrudability and Standoff Distance Effect during Nanoclay-Enabled Direct Printing," 1(2) pp. 123-134.

[95] Bos, F., Wolfs, R., Ahmed, Z., 2016, "Additive Manufacturing of Concrete in Construction: Potentials and Challenges of 3D Concrete Printing," Virtual and Physical Prototyping, 11(3) pp. 209-225.

[96] Kirby, B.J., 2010, "Micro-and Naonoscale Fluid Mechanics: Transport in Microfluidic Devices," Cambridge University Press, United States of America.

[97] He, Y., Yang, F., Zhao, H., 2016, "Research on the Printability of Hydrogels in 3D Bioprinting," SCIENTIFIC REPORTS, 6pp. 29977.

[98] Landau L., L. B., 1942, "Dragging of a Liquid by a Mvoing Plate," Acta Physcicochimica U.R.S.S., 17(42) pp. 42-54.

[99] Le Berre, M., Chen, Y., and Baigl, D., 2009, "From Convective Assembly to Landau−Levich Deposition of Multilayered Phospholipid Films of Controlled Thickness," Langmuir, 25(5) pp. 2554-2557.

[100] Janneck, R., Vercesi, F., Heremans, P., 2016, "Predictive Model for the Meniscus-Guided Coating of High-Quality Organic Single-Crystalline Thin Films," Advanced Materials, 28(36) pp. 8007-8013.

[101] Kim, J., Lee, S., Wajahat, M., 2016, "Three-Dimensional Printing of Highly Conductive Carbon Nanotube Microarchitectures with Fluid Ink," ACS NANO, 10(9) pp. 8879-8887.

[102] Crockett, R. S., 1997, "The Liquid-to-Solid Transition in Stereodeposition Techniques,".

[103] McKinley, G.H., 2005, "Visco-Elasto-Capillary Thinning and Break-Up of Complex Fluids," Massachusetts Institute of Technology, USA.

[104] Tuladhar, T., and Mackley, M., 2008, "Filament Stretching Rheometry and Break-Up Behaviour of Low Viscosity Polymer Solutions and Inkjet Fluids," Journal of Non-Newtonian Fluid Mechanics, 148(1-3) pp. 97-108.

[105] Kinloch, A., 2012, "Adhesion and adhesives: science and technology," Springer Science & Business Media, .

[106] Bonn, D., Eggers, J., Indekeu, J., 2009, "Wetting and Spreading," Reviews of Modern Physics, 81(2) pp. 739.

[107] Liang, T., Sun, W., Wang, L., 1996, "Effect of Surface Energies on Screen Printing Resolution," IEEE Transactions on Components, Packaging, and Manufacturing Technology: Part B, 19(2) pp. 423-426.

[108] Stauber, J., Wilson, S., Duffy, B., 2014, "On the Lifetimes of Evaporating Droplets," Journal of Fluid Mechanics, 744.

[109] King, B., Dimos, D., Yang, P., 1999, "Direct-Write Fabrication of Integrated, Multilayer Ceramic Components," Journal of Electroceramics, 3(2) pp. 173-178.

[110] Gross, G. W., Rhoades, B. K., Azzazy, H. M. E., 1995, "The use of Neuronal Networks on Multielectrode Arrays as Biosensors," Biosensors and Bioelectronics, 10(6) pp. 553-567.

[111] Mrksich, M., Dike, L. E., Tien, J., 1997, "Using Microcontact Printing to Pattern the Attachment of Mammalian Cells to Self-Assembled Monolayers of Alkanethiolates on Transparent Films of Gold and Silver," Experimental Cell Research, 235(2) pp. 305-313.

[112] Palchesko, R. N., Zhang, L., Sun, Y., 2012, "Development of Polydimethylsiloxane Substrates with Tunable Elastic Modulus to Study Cell Mechanobiology in Muscle and Nerve," Plos One, 7(12) pp. e51499.

[113] Muth, J. T., Vogt, D. M., Truby, R. L., 2014, "3D Printing: Embedded 3D Printing of Strain Sensors within Highly Stretchable Elastomers (Adv. Mater. 36/2014)," Advanced Materials, 26(36) pp. 6202-6202.

[114] Hinton, T. J., Jallerat, Q., Palchesko, R. N., 2015, "Three-Dimensional Printing of Complex Biological Structures by Freeform Reversible Embedding of Suspended Hydrogels," Science Advances, 1(9) .

[115] Structur3D Prining, 2017, "Https://www.structur3d.io/#discov3ry," .

[116] Comina, G., Suska, A., and Filippini, D., 2014, "PDMS Lab-on-a-Chip Fabrication using 3D Printed Templates," Lab on a Chip, 14(2) pp. 424-430.

[117] Schneider, F., Draheirn, J., Kamberger, R., 2009, "Process and Material Properties of Polydimethylsiloxane (PDMS) for Optical MEMS," Sensors and Actuators A-Physical, 151(2) pp. 95-99.

[118] Robinson, A., Minev, I., Graz, I., 2011, "Microstructured Silicone Substrate for Printable and Stretchable Metallic Films," Langmuir, 27(8) pp. 4279-4284.

3.6 Appendix A

A. 1: Analysis of Customer Need

To form a complete framework, we divided the printing process into four phases, organized existing knowledge of parts of the printing process, and bridged the gap of the parts that were not studied before. This appendix section is to show a step-by-step process of how to use our developed guiding framework to achieve successful printing under given conditions. An example in Table A.1 is used to illustrate how to determine if the target printing resolution can be successfully achieved with a set of user inputs.

Table A1: Definition of user requirement

Goal	Material	Target resolution
Evaluate if high resolution printing of a specific grade of PDMS is possible.	Polydimethylsiloxane (PDMS) with a given viscosity (μ)	100 nm

Inputs: Nozzle diameter (D), Nozzle length (L), Ink properties (e.g., viscosity μ, surface tension σ, and other properties that will be used in the equations below), applied pressure (P), and contact angle (θ).

Phase 1: Determine the flow rate exiting the nozzle

Step 1: Compute ink flow rate using the applicable equation (e.g., Eq. 3.4 for non-Newtonian inks). Since the feature resolution is largely dependent on the nozzle tip, printing should be performed using a nozzle diameter of around 100 nm.

$$Q = \left(\frac{n}{3n+1}\right)\pi\dot{\gamma}_o^{\frac{n-1}{n}}\left(\frac{\partial P/\partial z}{2\mu_o}\right)^{1/n} R^{\frac{3n+1}{n}} \qquad \text{Eq.3.4* (From the literature).}$$

Where $\partial P/\partial z$ is the pressure drop per unit length, n is the ink flow index, μ_o is the viscosity at a low shear rate, $\dot{\gamma}_o$ is the shear rate, which should be provided as user inputs.

Step 2: Is extrusion pressure enough to overcome surface tension force in order to produce cylindrical ink filament? The surface tension of the ink can be obtained from the literature.

$$\Delta P = \frac{4\sigma}{D}$$ Use Eq. 3.10* (From the literature)

Yes {Go to step 3}

No {This will make it difficult to perform successful printing. Consider modifying ink rheology or nozzle size (Go to step 1). However, the calculated pressure is not an absolute requirement and successful printing may still be achievable if the supplied pressure if not too far away from the calculated pressure. As shown in our research, the substrate movement can provide part of the required pressure by dragging the ink out of the nozzle if the nozzle tip is brought close to the substrate such that the ink meniscus directly contacts the substrate.}

Phase II: Determine whether the capillary rise will affect printing resolution and whether the ink will clog the nozzle due to evaporation

Step 3: Determine the ink flow velocity

$$v = \frac{Q}{A}$$ * (From the literature)

where Q was calculated from step 1 and A is the cross-sectional area of the nozzle.

Step 4: Compute the capillary number to determine if it is greater than 0.1 using Eq. 3.11.

$$Ca = \mu v/\sigma$$ *Use Eq. 3.11* (This research)

Use μ from step 1 and *v* from step 3.

Yes {Go to step 5)

No { Stop! Go to step 1. This will limit print resolution significantly. The user may consider increasing the flow rate or coating the nozzle surface with hydrophobic material to inhibit capillary rise effect or modify ink rheology.}

Step 5: Compute and compare if the flow time scale is less than evaporation timescale using Eq. 3.14 and Eq. 3.15.

$$t_{evap.} = \frac{V}{4\pi r_d} \frac{\rho}{J(c_o - c_\infty)}$$ *Use Eq. 3.14 (This research)

where V is the volume of ink droplet, J (mm^2/s) is the diffusivity of the vapor of the ink, and c (g/mm^3) is the concentration of the vapor per unit volume of air ($c = c_\infty$, at $r = \infty$; $c = c_o$ at $r = r_d$, where r_d is the radius of the liquid drop), and ρ is the density of the ink.

$$t_{flow} = \frac{D}{2v}$$ *Use Eq. 3.15 (This research)

Eq. 3.14 was defined by assuming the extruded ink forms into a spherical droplet with volume (V) which can be estimated from its radius r_d (note this value can be updated depending on the geometry of the extruded ink filament). J is the diffusivity of vapor of the ink into air which can be obtained from available literature, c_o can be estimated to equal to the saturation vapor concentration (c_v) of the ink at the interface between the ink and ambient air, c_∞ is the vapor concentration at far distance from the ink, which approaches the value of ambient air (given by Hc_v), H is the relative humidity of ambient air. The difference $c_o - c_\infty$ can therefore be expressed as $c_v(1 - H)$.

Yes {Go to step 6}

No {Stop! Go to step 1**.** This will cause clogging. Consider improving ink rheology or printing in a humid environment}

Phase III: Determine appropriate standoff distance and printing speed

Step 6: Estimate the appropriate standoff distance and printing speed using Eq. 3.17.

$$u_c = \frac{Q}{Dh}$$ *Use Eq. 3.17 (From the literature)

To compute the printing speed using Eq. 3.17, the user needs to assume the standoff distance. In general, a standoff distance of about the same size as the nozzle diameter is recommended as a starting point in order to achieve continuous ink filament. Since Q, D, and h are all experimental values, their values can be changed to yield different combinations of these variables, and the critical printing speed.

Phase IV: Determine appropriate substrate to print on

Step 7: Determine the surface energy of the ink, then print on a substrate having a lower surface energy than the ink in order to limit the tendency of spreading after deposition. Information regarding the contact (θ) between the material and the ink can be obtained from available literature. If the answer is YES to all the steps above, then Eq. 3. 20 can be used to estimate the final print resolution.

$$R_f = \sqrt{\frac{\pi v}{(4\theta - 2\sin 2\theta)u}}\, D_f$$ *Use Eq. 3.20 (From the literature)

where D_f is the initial filament diameter, of the extruded ink, and R_f describes the final radius of the cross section of the printed structure after wetting has taken place

with an equilibrium contact angle θ, between the ink and substrate, u is the printing speed of the substrate.

Outputs: **Yes** {The print resolution is estimated to have a width, W equal to $2* R_f$, computed from Eq. 3.20. For this equation to apply, the user must follow the 7-step process, with the "yes option" outlined above. Here we assume the extruded ink filament has a simple cylindrical profile, and evaporation and surface wetting do not affect the printing process} and a good starting point for fine-tuning the printing parameters for better printing results.

No { If the above conditions are not satisfied, then it will be very challenging to achieve the target print resolution.}

A.2 Non-Dimensional Analysis

From Eq. 3.1, we understand that the feature area (A) (i.e., having width (W) and thickness (H)) is a function of 8 important variables outlined in Table A2.

$$W = f(Q(P, \mu, L, \sigma, D), u, h, \theta) \quad (A.1)$$

$$H = g(Q(P, \mu, L, \sigma, D), u, h, \theta) \quad (A.2)$$

Table A2: List of variables that determine feature resolution

Parameter	Dimension	Explanation
Width (W)	L	Width of printed feature
Thickness (H)	L	Height of printed feature
Flow rate (Q)	L^3T	Ink flow rate
Pressure (P)	$ML^{-1}T^{-2}$	Applied pressure driving ink flow
Viscosity (μ)	$ML^{-1}T^{-1}$	Ink viscosity
Length (l)	L	Length of dispensing nozzle
Diameter (D)	L	Nozzle diameter
Surface tension (σ)	MT^{-2}	Surface tension of ink
Velocity	LT^{-1}	Substrate printing speed
Standoff distance (h)	L	Gap between nozzle tip and the substrate
Contact angle (θ)	1	Contact angel between ink filament and the substrate

Here, we seek to obtain a non-dimensional form of this equation. Hence, we perform dimensional analysis and apply Buckingham's π Theorem. There is a total of 9 variables (8 independent and 1 dependent variable). Number of primary dimensions is 3, giving 6 non-dimensional numbers. After careful a consideration, D, u and σ were chosen to form the set of repeating variables.

$$\pi_1 = (D, u, \sigma, W) \quad (A.3)$$

$$\pi_2 = (D, u, \sigma, P) \quad (A.4)$$

$$\pi_3 = (D, u, \sigma, \mu) \quad (A.5)$$

$$\pi_4 = (D, u, \sigma, l) \quad (A.6)$$

$$\pi_5 = (D, u, \sigma, h) \tag{A.7}$$

$$\pi_6 = \theta \tag{A.8}$$

Since θ is already dimensional.

Substituting the dimensions of the variable into the equations yield the following:

$$\pi_1 = [L]^a[LT^{-1}]^b[MT^{-2}]^c[L] \tag{A.9}$$

$$\pi_2 = [L]^d[LT^{-1}]^e[MT^{-2}]^f[ML^{-1}T^{-2}] \tag{A.10}$$

$$\pi_3 = [L]^g[LT^{-1}]^h[MT^{-2}]^i[ML^{-1}T^{-1}] \tag{A.11}$$

$$\pi_4 = [L]^j[LT^{-1}]^k[MT^{-2}]^l[L] \tag{A.12}$$

$$\pi_5 = [L]^m[LT^{-1}]^n[MT^{-2}]^p[L] \tag{A.13}$$

The non-dimensional numbers are:

$$\pi_1 = WD^{-1} = \frac{W}{D} \tag{A.14}$$

$$\pi_2 = D\sigma^{-1}P = \frac{DP}{\sigma} \tag{A.15}$$

$$\pi_3 = u\sigma^{-1}\mu = \frac{u\mu}{\sigma} \tag{A.16}$$

$$\pi_4 = lD^{-1} = \frac{l}{D} \tag{A.17}$$

$$\pi_5 = hD^{-1} = \frac{h}{D} \tag{A.18}$$

The functional relationship between the π's is:

$$\pi_1 = f(\pi_2, \pi_3, \pi_4, \pi_5, \pi_6) \rightarrow \frac{W}{D} = f\left(\frac{DP}{\sigma}, Ca, \frac{l}{D}, \frac{h,}{D}, \theta\right)$$

$$\pi_1 = g(\pi_2, \pi_3, \pi_4, \pi_5, \pi_6) \rightarrow \frac{H}{D} = \mathrm{g}\left(\frac{DP}{\sigma}, Ca, \frac{l}{D}, \frac{h,}{D}, \theta\right)$$

$$\mathrm{Ca} = \frac{u\mu}{\sigma}$$

CHAPTER 4

3D Printed Optics with a Soft and Stretchable Optical Material

Cost-efficient methods are needed for creating complex optical waveguides with materials possessing excellent optical properties. In this chapter, the mechanical and optical properties of a new soft and flexible gel is studied for making customizable optics. To accomplish waveguide fabrication, a novel printhead for continuous melt and extrusion of the gel is designed and developed. Next, the printhead is retrofitted to the microextrusion 3D printer discussed in chapter two, enabling printing of both 2D and 3D waveguide structures. Benefiting from this system, several optical applications are demonstrated.

4.0 Abstract

Waveguides are important optical elements for sensing, illumination, artistic displays, integrated optical circuits, as well as teaching aids for demonstrating important optical phenomena. However, despite the high demand, most optical materials are difficult to fabricate into desired shapes using state-of-the-art manufacturing technologies. This paper presents a novel method for 3D printing customizable optics with a soft and stretchable (over 100% elastic strains) thermoplastic polymer. To showcase the versatility of this approach, several applications were demonstrated, including unique artistic illumination, caustic patterns, beam splitter and combiner on both planar and 3D conformal surfaces, and optical encoder. The printed waveguides exhibit an outstanding optical transparency of more than 98% and an optical loss of less than 0.22 $dBcm^{-1}$. The simplicity of the fabrication process, low-cost, excellent optical properties, and flexibility provide an attractive pathway for fabricating integrated optical devices and new opportunities for controlling light.

Keywords: 3D printing, optical waveguides, transparent polymer, caustic patterns, optical encoder

4.1 Introduction

By exploiting known optical principles (e.g., transmittance, reflectance, fluorescence, luminescence, absorbance, etc.), photonics is gaining heightened interest in many areas including wearable strain sensors for human motion detection[1-3], chemical sensing (e.g., gases [4], local blood pH measurement [5], chemical species detection [6], etc.), artistic displays[7], illumination, in optomechanical systems for displacement measurement [8], as well as teaching aids for demonstrating important optical phenomena[9]. To successfully harness these opportunities, low-cost methods for creating complex optical structures with materials possessing excellent optical properties are required.

Herein we present a novel method that enables the creation of customizable optics in both 2D and 3D motifs, which consists of a custom-designed microextrusion 3D printing system for printing an optically clear ballistic gel. The clear ballistic gel offers outstanding optical and mechanical properties, such as excellent optical transparency (>98%), good refractive index, flexibility, lightweight (e.g., 0.91 gcm^{-3} compared to glass with 2.2 gcm^{-3}) [10, 11], and low cost. These properties make it very appealing for designing various optical elements, including artistic displays, caustic patterns, beam splitters and combiners, optical integrated circuits, and optical sensors. Unlike existing hard and rigid optical materials (mostly glass and polymers), the flexible nature of this gel offers large elastic strains (>100%), and may prove suitable for mechanically challenging applications, and strain sensitive sensors for human motion monitoring, and conformal optics.

Until recently, classical optical devices were routinely fabricated using glass. However, the harsh processing conditions (e.g., hazardous chemicals and high temperature in excess of 1000^{o}C), lengthy fabrication steps, and the resultant high overall cost for custom designs have limited some of its potential uses [11-14]. To overcome the challenge, many studies have been directed towards polymer and hybrid inorganic-organic materials, enabling near room temperature processing of optical components [15], and the use of state-of-the-art fabrication methods. With the adoption of 3D printing technique, waveguides with arbitrary geometries and near-circular cross-sectional profile (in contrast to the conventional planar cross-sections often obtained with photolithography technologies) were realized. Table 1 shows a comparison of the studies of 3D printed optics in the literature, including printing with fused glass [11], photocurable polymeric resins [16, 17], and biocompatible silk [18]. However, these methods have a number of drawbacks, such as only capable of making hard and rigid structures, inconvenient 3D printing methods due to the

requirements of either high post-sintering temperature or the need of carefully-designed support materials for the printing process, poor resolution, and non-ideal-circular cross-section profile (because the ink wets and spreads on the substrate during the printing process before polymerization), and limited capability for printing 3D geometries (mostly simple planar structures).

To address these issues, we developed a new method of 3D printing an optically clear ballistic gel (commercially available as Clear Ballistic gel) [10]. While this gel has proven to be successful in the ballistics testing due to its human flesh-like properties, its promise for other promising applications (e.g., optical) has yet to be tapped because the fabrication process relies on conventional molding methods, which limits the complexity of the structure that can be made and is time-consuming and expensive for iterative design processes. A new method to fabricate structures with Clear Ballistics gel is needed to enable these new applications. In this paper, we developed a microextrusion-based 3D printer that can print the gel in the open air without the need of a support bath or supporting materials and demonstrated its promise with a variety of optical applications, including unique artistic illumination, caustic patterns, beam splitter and combiner on both planar and 3D conformal surfaces, and optical encoder.

Table 4.1: Overview of different 3D printed waveguide materials, properties, and fabrication methods

Method	Material	Transmittance (%)	Minimum Feature resolution (μm)	Feature Dimension	Processing condition	Surface roughness (nm)	Optical loss ($dB.cm^{-1}$)	Ref. index	Ref.
Stereolithography	Fused glass	66	80	3D	Thermal debinding; vacuum sintering 1300°C	2	-	-	[11]
Extrusion 3DP	OrmoClear®	~98	382 ±19	2D	UV curing, encapsulated within a support material	10-20	0.1	1.555 @ 589 nm	[16, 19]
	Biocompatible silk	~95	5	2D	Printed into methanol-rich reservoir	Very smooth	0.25	1.54 @ 633nm	[18, 20]
This Study	**Clear ballistic gel**	**>98**	**150**	**2D/3D**	**Direct print in open atmosphere**	**Very smooth**	**0.22**	**1.537 @ 520 -574 nm**	**This paper**

4.2 Results and Discussion

4.2.1 Microextrusion-based Gel Printing

Although there are many commercial fused deposition modeling (FDM) printers for 3D printing of thermoplastic polymers, no existing printers are compatible for printing the ballistic gel due to its flexibility. To overcome this issue, we developed a low-cost syringe-based printhead for continuous melt and extrusion of the ballistic gel, which starts to melt at around 70 °C. We then mounted the printhead onto a custom-made 3D printer reported in our prior work [21] for 3D printing of the gel. The custom-designed printhead consists of a 30 mL glass syringe which functions as the ink reservoir, and a deposition nozzle. Both housed within a heated aluminum chamber to facilitate gel heating and extrusion as shown Figure 4.1. The gel is first melted and then pushed out of the nozzle by controlling the deposition pressure with a digital valve, which is connected to a pressure source. The key to successful gel printing is the ability to control ink rheology and optimize the printing parameters. The printhead was specifically designed to meet the following challenges: 1) uniformity of the heating to avoid clogging; 2) good heat insulation with other components; 3) capable of maintaining a constant temperature between 70 to 130 °C with minimal variation; 4) capable of printing with needle size smaller than 100 μm.

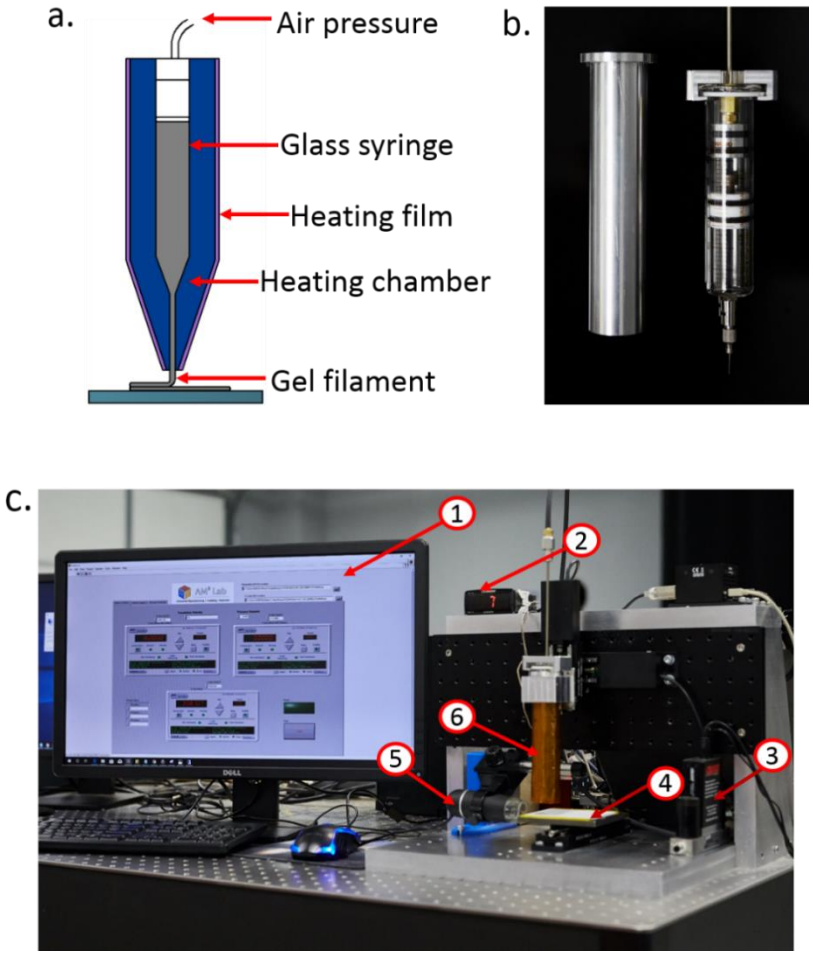

Figure 4.1: Microextrusion-based gel printing system. (a). Schematic illustration of the printhead design, (b). The fabricated heating chamber and nozzle assembly, c). Our in-house printing system with printhead - (1) Control software, (2) Temperature controller, (3) Pressure regulator, (4) substrate, ((5) Vision system, (6) Printhead with a heating film.

To optimize the process parameters, we characterized the ink viscosity as a function of shear rate at a temperature ranging from 80 to 130^{o}C. Figure 4.2 reveals that the gel exhibits a shear thickening behavior (only the results for gel grade #20 at 100, 110 and 130^{o}C are shown here). As an example, in Figure 4.2 we compare the results of the gel extrusion using a fixed nozzle diameter (D = 210 μm) and applied pressure (P = 100 psi). At a low heating temperature (80 to 100^{o}C), viscosity increases significantly, and the dispensing process requires very high pressure to sustain consistent flow rates. On the other hand, at higher heating temperature (≥110^{o}C) when viscosity

decreases, however, the gel oozes out of the nozzle tip even with no applied pressure and forms droplet that wets the nozzle surface. Consistent gel extrusion was achieved at a temperature of 110^{o}C with modest deposition pressures. It's worth to note that a temperature change of 30 °C (from 100 to 130 °C) results in a viscosity change of almost two orders of magnitude. With careful selection of the nozzle diameter, printing speed, temperature, and applied deposition pressure, the printing resolution and quality can be controlled, guided by a microextrusion printing framework developed in our prior work [21].

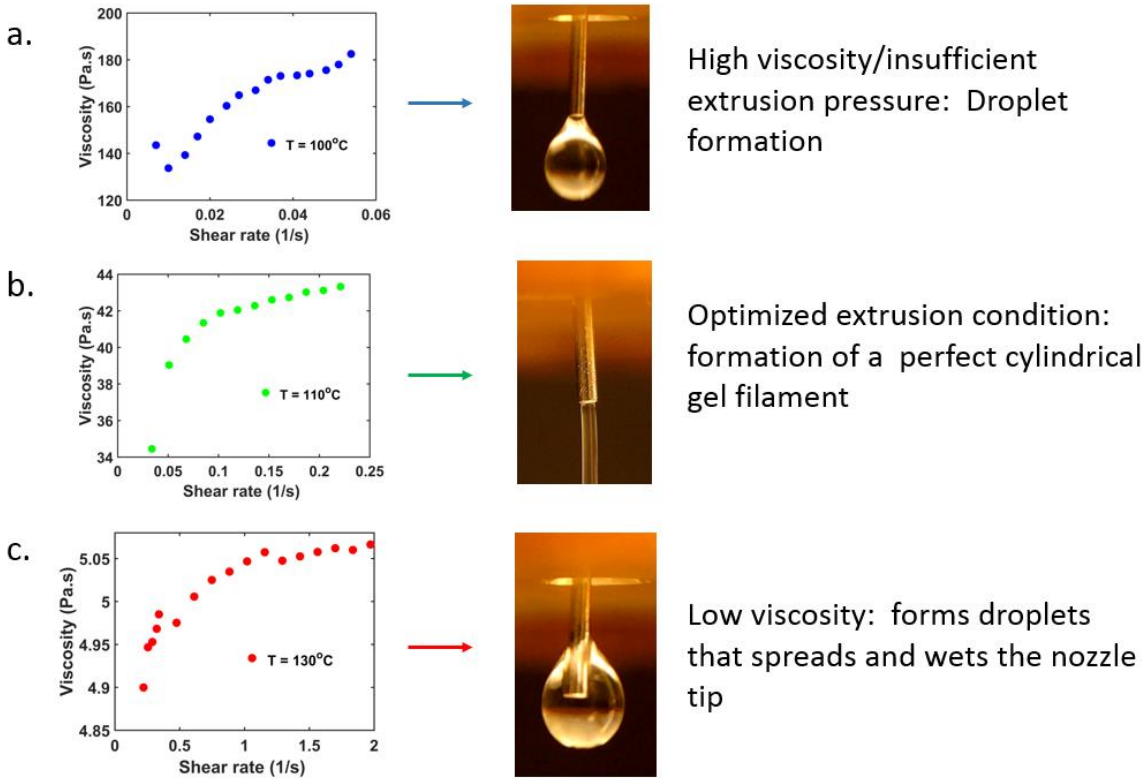

Figure 4.2: Overview of ink dispensing process. Rheological flow curves of Clear Ballistics gel (#20) indicates a shear thickening behavior. While an increase in the melting temperature results in lower viscosity it has a negative impact on the print resolution. Lower melting temperature enables the creation of high-resolution structures that retain cylindrical shape upon deposition but is limited by the requirement of high deposition pressure.

4.2.2 Characterization of Printed 2D and 3D Structures

Using this printing system, we demonstrated printing of a variety of straight and curved planar structures (Figure 4.3 and Video S1, Supporting Information). These structures highlight the ability to control filament geometry and size. For example, using a dispensing nozzle with a diameter of 210 μm, we were able to achieve a consistent printing resolution of 154 μm (Figure 4.3a). Because of the intended application for optics, it is necessary to obtain an estimate of the surface quality of the printed samples. In the literature, the surface roughness of optical materials is commonly measured by atomic force microscope (AFM)[16]. However, after several attempts, we found this approach not suitable due to the softness of the gel. Non-contact optical methods have also been reported for assessing surface quality of the printed PDMS [22]. Therefore, we used a high-resolution optical microscope (Keyence VHX-2000) with a resolution of 1 um to provide a visual inspection of the gel surface roughness. As verified by the optical image, no visual roughness is observed on the printed features (Figure 4.3d). We therefore expect the surface roughness to be in the sub-micrometer range, which is important to minimize scattering losses[16].

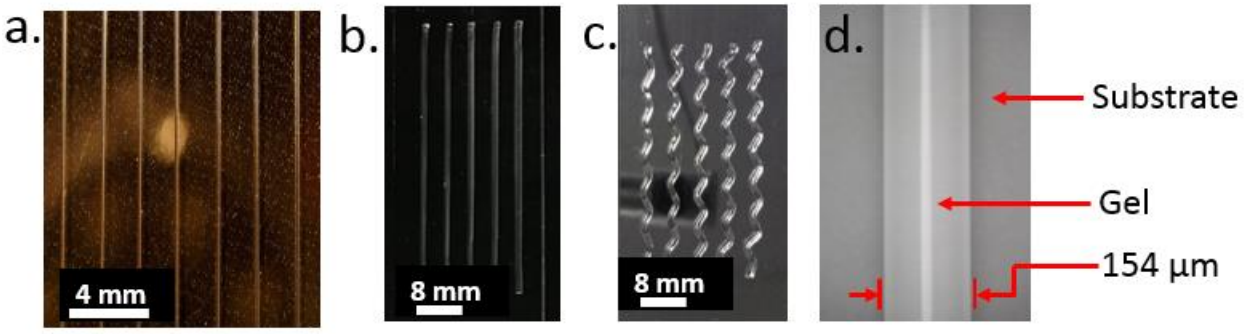

Figure 4.3: Optical images of (a) Straight waveguide printed from a 210 μm nozzle, (b) Straight, and (c) Curved waveguides printed using an 810μm nozzle, (d) High-resolution surface image of the printed gel filament using an optical microscope (VHX-2000, Keyence) shows a smooth surface of the gel.

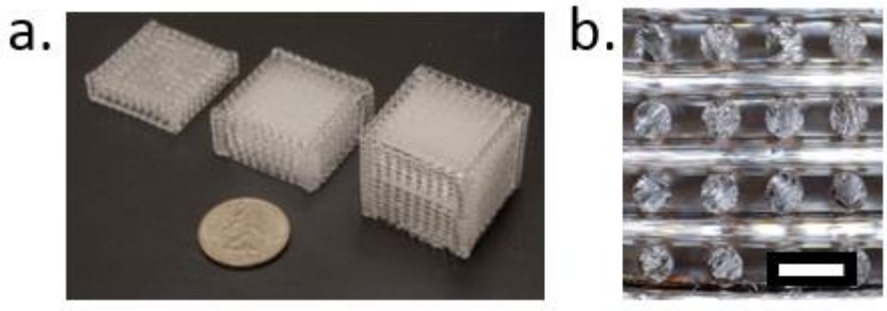

Figure 4.4: (a) Optical image of 8, 16 and 32 layers of woodpile structures, (b) Cross-sectional cut through (a) reveals that that gel filament maintained their cylindrical structure. Printing was carried out using an 810 μm nozzle with in-plane center-to-center filament spacing of 1.5 mm. Scale bar = 1600 μm.

Furthermore, we printed a broad range of 3D periodic woodpile structures, including 8, 16 and 32-layers covering an area of 30 mm x 30 mm (Figure 4.4). The cross-sectional cut through the printed structure reveals that the filaments maintained a good cylindrical shape with a diameter conforming to the nozzle diameter. To investigate the mechanical stretchability and elastic recovery, a uniaxial strain applied to the printed gel filament revealed the ability to be strained up to 100% and elastically recover (Figure S1a and Video S2, Supporting Information). The mechanical flexibility of the gel was confirmed by twisting around a cylindrical rod to form a helical profile ((Figure S1b, Supporting Information). In addition, to determine the ultimate strain and Young's modulus, a uniaxial tensile test was carried using molded dumb-bell test specimen (Figure S2 and S3, Supporting Information). The Young's modulus was determined to be 77.6 kPa (from the 5 – 20% linear strain) and a maximum (failure) strain of 292%. The test results are shown in Figure S4 (Supporting Information). The flexible nature of this material makes it an attractive candidate for optical based strain sensors[1, 2, 23].

4.2.3 Optical Properties

Toward our goal of 3D printed optics using a flexible optical grade gel, we evaluated the optical properties of the gel using three important metrics: refractive index, optical transmittance, and transmission losses. It is common knowledge that waveguides operate by the principle of total internal reflection (TIR), which requires the light-guiding medium to have a higher refractive index relative to the surrounding environments (Figure S5, Supporting Information). In order to estimate the refractive index of the gel grades, we measured the refractive indices of three grades of the gel using Snell's law (Figure S6, Supporting Information). As can be seen in Figure 4.5, gel grade #20 was found to have an average refractive index of 1.537 with as standard deviation of 0.0244 (obtained from the mean of four measurements), which shows minimal variation. This refractive index is slightly higher than that of fused silica glass with an average of 1.458 and therefore selected for the rest of this study.

In the realms of optics, high optical transmittance is important to ensure high efficiency of light transmission. To this end, we assessed the gel's optical transparency in the ultraviolet, visible and infrared regions of the spectrum. The spectral evaluation shown in Figure 4.6 reveals its superior transparency compared to commercially available fused silica glass and is on par with previously reported optical grade polymers (Figure 4.7) [11, 19, 20].

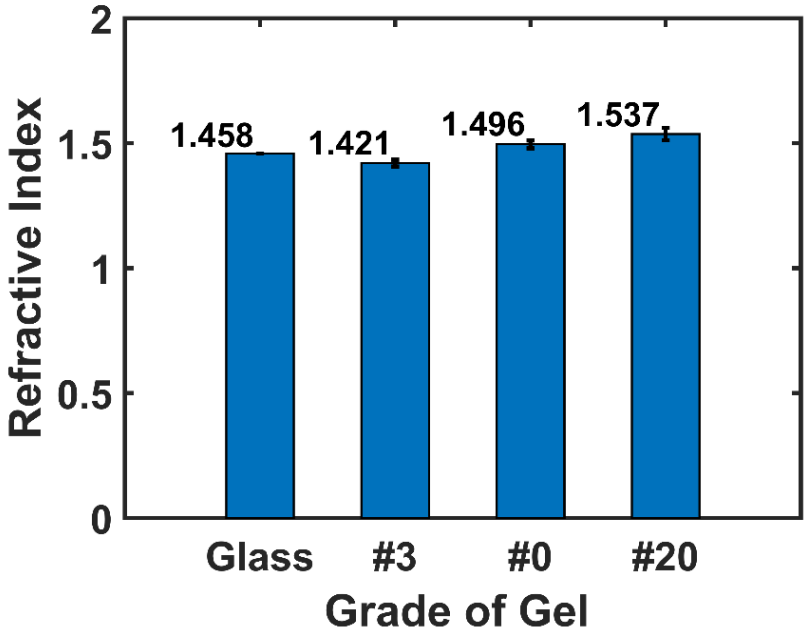

Figure 4.5: Refractive index of different gel grades compared to that of fused silica glass

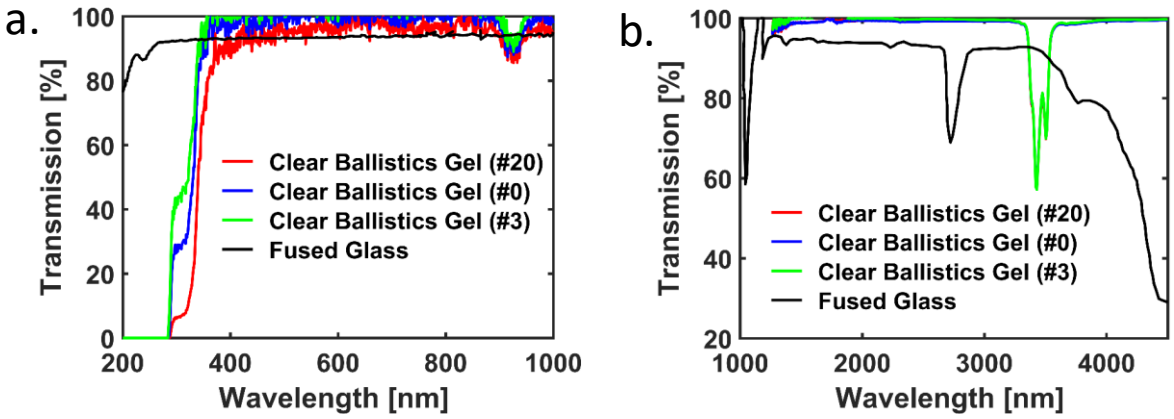

Figure 4.6: Optical characterization of different gel grades compared to commercial fused silica glass. Both the (a) UV–vis transmission spectra, and (b) Infrared spectroscopy data reveal that all the three gel grades have superior transparency than commercially available optical-grade fused silica glass [11].

Figure 4.8 showcases the light guiding ability of the gel with minimal optical losses. The transmission loss of straight waveguide was measured via the cutback method [16]. The coupled-output power as a function of the waveguide length is shown in Figure 4.8a. The measured

propagation loss is obtained from the slope of the line of best fit to be 0.22 $dBcm^{-1}$ using a green LED (520 - 574 nm), which is on par with other reported optical polymers (see Figure 4.8a). To qualitatively demonstrate its potential for guiding light, we printed a network of straight and curved waveguide and coupled them to four different colored LEDs to distribute colored lights (Figure 4.8 b, c). The emergence of the bright light at the end of the waveguides indicate good light guiding of by total internal reflection (TIR).

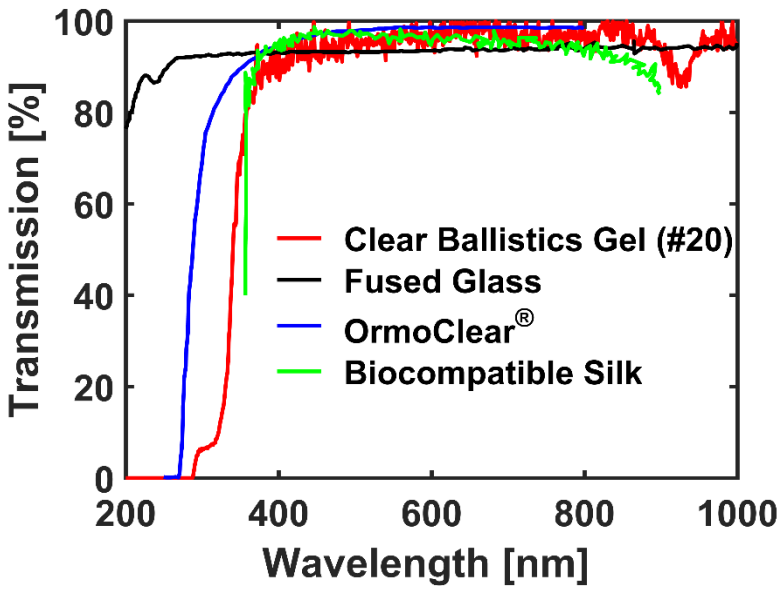

Figure 4.7: Comparison of UV–vis transmission spectra of the clear ballistics gel and commercial grade fused glass and other previously reported optical grade polymers (comparison data extracted from Ref. [11, 19, 20]).

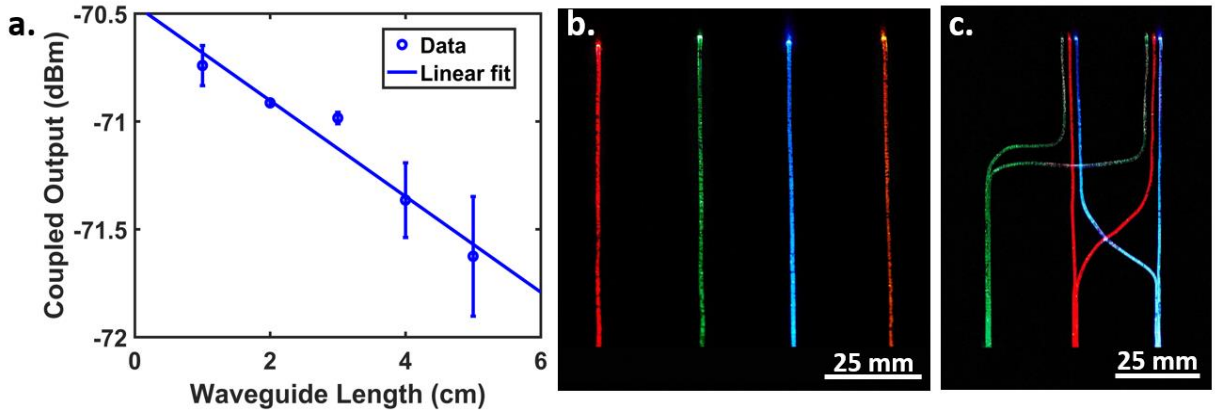

Figure 4.8: (a) Waveguide propagation loss determined by the cut-back method, (b) Images of straight optical waveguides coupled to four LEDs, and (c) A network of six optical waveguides coupled to three LEDs to distribute colored light.

To further demonstrate the high optical transparency of the gel, we printed a variety of 3D structures. In the first case, the printed shapes are illuminated along their central axis with an overhead green LED, creating interesting caustic patterns (Figure 4.9a-c) similar to those realized with glass structures [7]. The nature of the caustic patterns can be controlled by varying the shape and surface texture the printed shapes. Kiser et al. [24] showed that it is possible to use a computer algorithm to design the shape of the optical structure to generate any arbitrary caustic patterns. The 3D printing capability of the optical soft gel presented in our work offers exciting opportunities for enabling creation of arbitrary caustic patterns. In the second scenario, a printed square cup was filled with dyed water (Figure 4.9d). The liquid is clearly seen from the walls of the cup which shows the fusion of the layers, and do not affect the material transparency of the structure. This remarkable transparency and material flexibility make our system very attractive for fabricating integrated fluidic device [25].

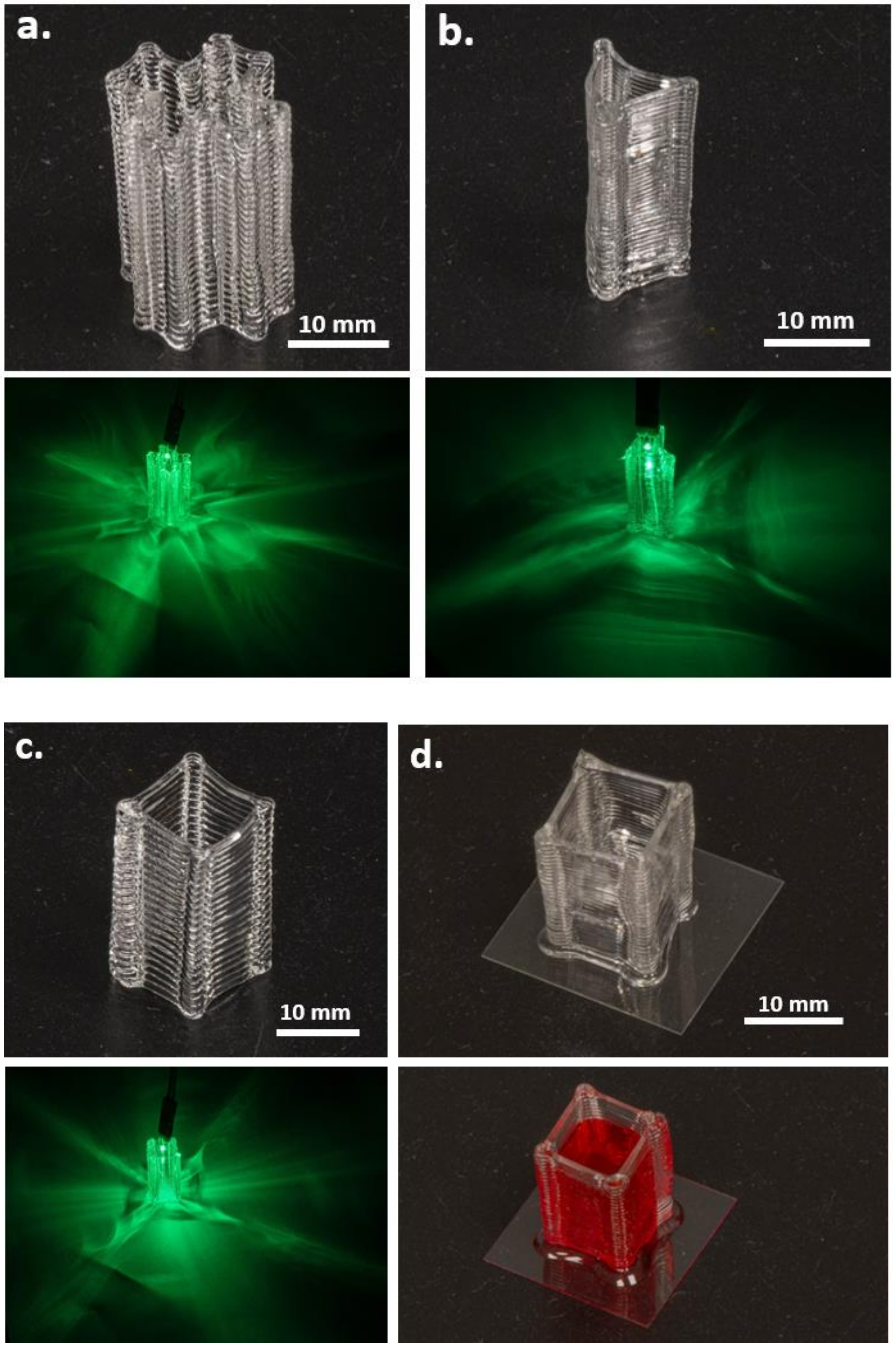

Figure 4.9: Optical properties and caustic patterns of printed shapes. (a-c) Top views show the high level of transparency of as-printed objects, with the caustic patterns produced by illumination from a suspended overhead green LED below. (d) Printed square cup containing dyed water and highlighting the high optical transparency of the structure.

4.3 Applications

Having obtained both qualitative and quantitative data on the mechanical and optical properties of the gel, in this section we demonstrate applications that may take advantage of the highlighted feaures. We here demonstrate versatility of our approach in three different applications, including unique artistic illumination, light wave splitter and combiner circuits on planar and 3D conformal surfaces, as well as an optical encoder. Artists often require certain arbitrary lighting geometry for creating desired rendering effects. While this is easily realized virtually using computer software [26], it is inconvenient and expensive to achieve in the real world because most optical materials are not flexible. Our work offers an easy and low-cost solution to creating stylized lighting manipulation on complex pathways (Figure 4.10). We verify this by producing unique lighting effects on planar, spiral, and conformal surfaces. For example, in Figure 4.10f,g we patterned the name of our group, "AM^3 Lab" on a paper substrate and lighted the letters by coupling them to different colored LEDs. This approach may, therefore, provide a way to easily prototype, iterate, and optimize various lighting effects.

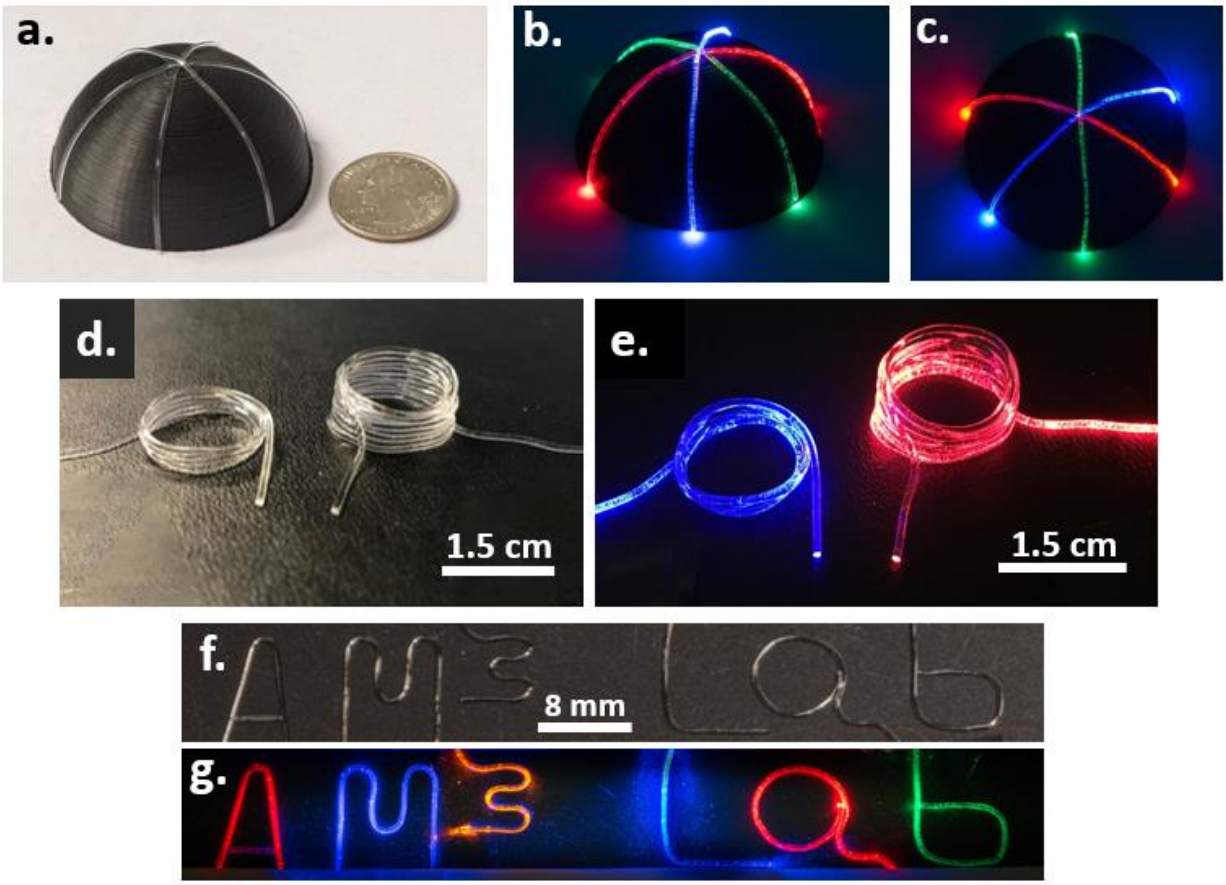

Figure 4.10: Photographs of various artistic patterns and illumination. TOP: (a) As-printed waveguide on a 3D printed dome, (b) Side and (c) Top views of the lighted waveguide. MIDDLE: (d) Spiral waveguides before, and (e) after coupling to LEDs. BOTTOM: (f) Pattern of our group name "AM^3 Lab" on a black paper substrate, and (g) Lighted with different LEDs.

In addition, because the possibility of creating integrated 3-D optical system could give rise to increased packing efficiency with minimal crosstalk [15, 27], we demonstrate printing of an integrated beam splitter and combiner on a 3D surface. As an example, in Figure 4.11a-d, we show that an integrated beam splitter and combiner coupled to three different LEDs (embedded within the hollow plastic hemisphere) could be created conformably on a dome-shaped substrate. Different color and light combinations are achieved. In addition, a planar 1x4 beam splitter was formed [28] (Figure 4.11e) and a planar beam combiner, producing magenta, and cyan by coupling

red, blue and green LEDs through the printed waveguides (Figure 4.11f). We measured the output split ratio of the power splitter (i.e., Figure 4.11e) between the right arm (C and D) to the left (A and B) to be 1: 0.95. This was obtained by measuring the output light intensity ratio between the two splits using luminosity sensors. The slight difference in the power output ratio may be attributed to the variations in the branching angle, the uniformity of the printed gel, and the length of the arms [29]. Nonetheless, the results are repeatable and consistent with less than 5% of variation.

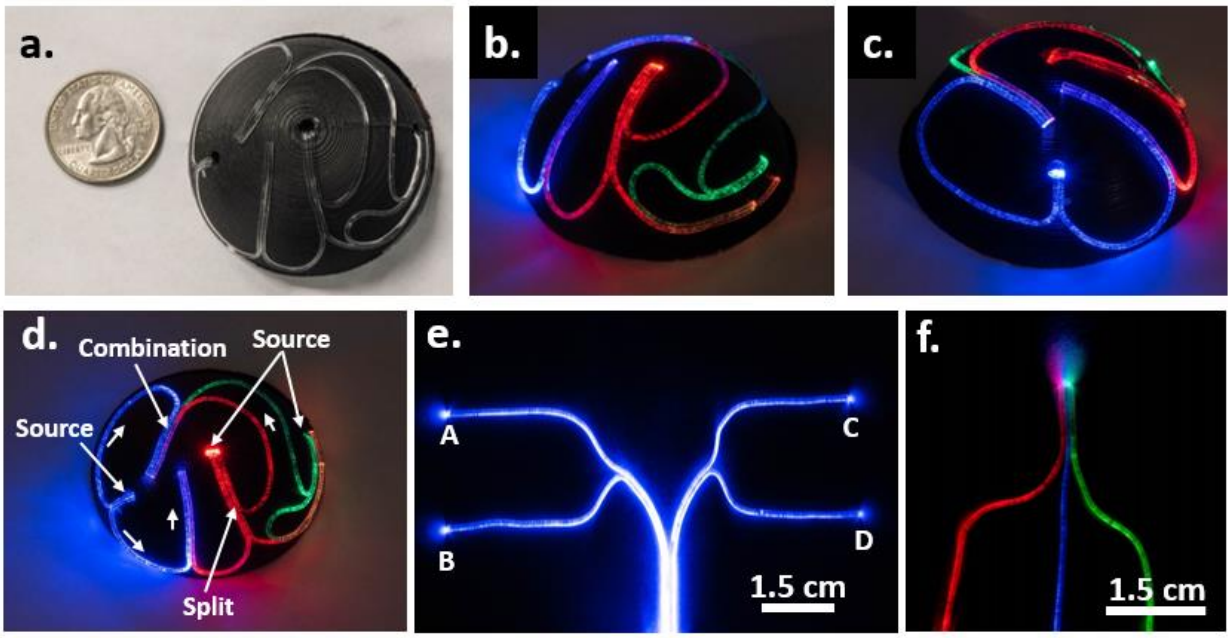

Figure 4.11: Photographs of the 3D printed beam splitter and combiner circuits. (a) As-printed waveguide splitter and combiner circuit on a 3D printed dome surface, (b) Right, (c) Left, and (d) Top views of the lighted waveguide. (e) A 1x4 planar beam splitter, and (f) Planar beam combiner.

As a final demonstration, an optical encoder that relies on the change of light intensity with the waveguide displacement from a light intensity sensor was designed and fabricated. Optical sensors rely on the transduction of optical signals to provide real-time information regarding the presence, absence, change of a target property [6]. In electromechanical systems, they are used for

sensing mechanical motion, being important elements in linear encoders to monitor linear movements, or switches[8]. Here, using the printed waveguide, we demonstrate its potential application for sensing linear displacements. Figure 4.12a provides an overview of the operating principle of the sensor. As the user slides the waveguide away from the luminosity sensor, the magnitude of the luminosity changes. Accordingly, a prototype linear encoder was designed and implemented to sense various light intensity based on the linear displacement of the waveguide (Figure 4.12b). An LED and luminosity sensor are mounted on the opposite ends of the slider. The plot of the illuminance as a function of displacement is shown in Figure 4.12c. The working principle of the sensor is based on increased intensity losses with distance further away from the light detector due to light having to travel a longer path. The results were repeatable for distance measurements within 0.6 mm, with careful management of light scattering, and coupling of the waveguide to the LED and detector [3].

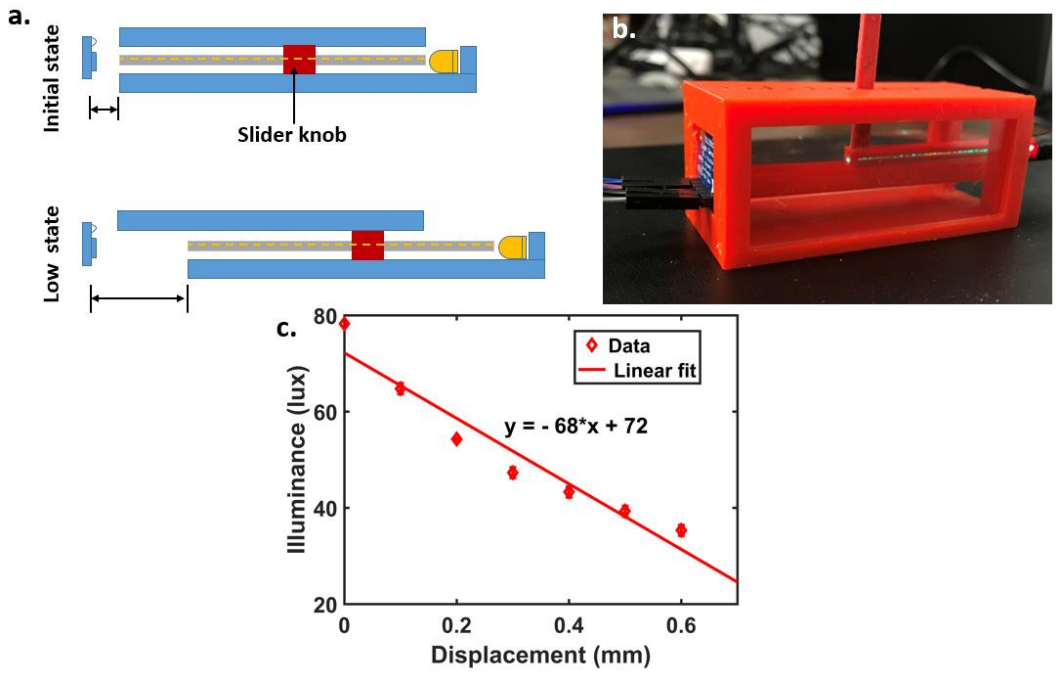

Figure 4.12: Optical Encoder. (a) Schematic illustration of the principle of the linear encoder, and (b) Photography of fabricated linear encoder, (c) Correlation between the measured illuminance as a function of displacement of the optical waveguide.

4.4 Conclusions

In summary, we reported a new method for 3D printing of optics with a flexible thermoplastic polymer. Unlike existing methods for fabricating optical devices with rigid glass or polymers, our method enables direct 3D printing of soft and stretchable optical devices at low cost. The printed waveguides show outstanding optical transparency (>98%) and low transmission losses (~0.22 $dBcm^{-1}$). In addition to the optical performance, we demonstrated direct printing in the open air, in contrast to existing methods of printing optics that requires either carefully-designed support materials during the printing process or extreme post-processing conditions, of soft and stretchable optics (with a ultimate strain of 238.92% and elastic strain of over 100%) in both 2D and 3D with a printing resolution of ~150 μm, which makes this approach very appealing for a wide variety of applications.

To demonstrate the versatility of this method for 3D printed optics, we presented several exemplary applications, including unique artistic illuminations, caustic patterns, beam splitter and combiner circuits on both planar and 3D conformal surfaces, as well as an optical encoder. The easiness in developing successful optical applications in short time at low cost with our approach offers new opportunities of creating integrated optical circuits, complex optical devices, and other innovative optical applications that were not possible before, which will potentially have a significant impact to the optical industry. Although the measured transmission loss is comparable to other reported optical grade polymers, this value can be improved to meet the criteria for high-quality optics by refining the purity of the printed waveguides (e.g., through careful washing and drying of the gel prior to printing in order to eliminate any debris). Optical relays can also be used for applications that require long-distance transmission of optical signals.

4.5 Methods

Gel Preparation: We investigated the properties of three different grades of Clear Ballistic gel (i.e., #3, #0, and #20) acquired from Clear Ballistics. To get them ready for printing, first, the gel is washed with water to remove any debris and allowed to dry for 12 hours to completely remove all moisture prior to cutting into small lumps for melting. Second, the moisture-free gels were placed into a glass beaker and heated on a hotplate maintained at a temperature between 100 - 125^{o}C. To avoid exceeding the recommended maximum temperature of ~135^{o}, the temperature during heating was monitored using an infrared thermometer. Once the gel was completely melted and free from air bubbles, it was ready to be loaded into the 3D printer.

3D printing: The printing process was carried out using our custom-made 3D microextrusion printer, which has a 50 nm resolution of motion in XYZ axis. The pre-melted gel was loaded onto

a 30 ml glass syringe. The ink dispensing process was driven by a pressure guided piston that was made of acrylic material capable of withstanding the high melting temperature.

Mechanical Testing: To obtain the mechanical properties of Clear Ballistics gel, a plastic mold was designed to make the tensile test specimens for the gel according to ISO 37:2011 standard (Rubber, vulcanized or thermoplastic – Determination of tensile stress-strain properties). The plastic mold was then 3D printed using Stratasys' UPrint SE Plus printer (Figure S1, Supporting Information) with ABS since ABS melts at 210^{o}C, and can withstand the gel's melting temperature of ~100^{o}C. For a successful molding process, a mold release agent (Frekote 398489 770-NC) is applied to the mold surface prior to pouring the gel. Without this step, the gel bonds to the mold and can be very difficult to detach. During pouring, care must be taken to avoid entrapment of air bubbles which could negatively impact on the gel's properties including optical clarity, and mechanical strength.

The standard dumb-bell bone specimens were obtained from the molding process. A total of four samples were made. Each sample was stretched at a 10.00 mm/min until failure using Tinus Olsen H50KS tensile testing machine. The setup for the testing process is presented in the supporting information. The elastic modulus was obtained from the slope of the linear region of the stress-strain curve.

Rheological characterization: The rheological measurement was carried out using a controlled-speed rheometer (Brookfield DV3T LV), which is equipped with a Thermosel accessory for heating and controlling the temperature. To reveal any shear rate dependence, ink viscosity was characterized at a controlled shear rate mode ranging from 0.03 to 1.972 s^{-1}. To reduce variability

in the measurement results, an averaged value for each set of condition was obtained over a 60 second period.

Optical characterization

Refractive index measurement: The refractive indices of three gel grades were measured using Snell's law. To achieve this, rectangular gel blocks (7.5 cm x 14.5 cm x 2 cm) were molded (Figure S5, Supporting Information). Four different measurement were taken from four incident (i.e., 50, 40, 30 and 20^{o}) and refracted (i.e., 31, 25, 18, and 13^{o}) angles. Gel grade #20 was found to have the highest average refractive index of 1.53.

Optical transmittance measurement**:** Cary® 50 Bio UV-Vis Spectrophotometer (Varian Inc., USA) was used in characterizing optical transmission in the ultraviolet and visible spectra. For this test, the melted gel was poured into a cuvette. Transmission in the infrared region was measured using a Fourier transform infrared (FTIR) spectrophotometer of the type IRAffinity-1S (Shimadzu Corporation, USA). The transmission spectrum was recorded for different thicknesses (210μm, and 800μm for the printed gels, and 2 mm, 3 mm, and 6 mm for the molded gels). Because the results did not show any significant dependence on the sample thicknesses, only the results for 2 mm-thick samples are presented.

Optical loss measurement: The optical loss experiment was performed using the cutback method. To achieve this, one end of the waveguide was coupled to green LED (in the wavelength range 520 -574 nm) and the other end to a luminosity sensor (Adafruit TSL2591). The measured lux from the sensor was converted to dBm. After each measurement, the waveguide was cut-back in length of about 1 cm and the test repeated. Due to the difficulty of aligning the LED to the

waveguide, a waveguide with a diameter ~800 μm was used for this test. The result presented here represents averages of 3 measurements from 3 different waveguides.

Optical waveguide network: To create the waveguide network of colored LED, we printed straight and curved waveguides and aligned their ends to four different LEDs (SMD 0805 LED, Kaifa): red (615 – 660 nm), green (520 -574 nm), blue (465-475 nm) and yellow (572 – 595 nm). We designed a custom mount circuit to hold the waveguide, and a circuit to control the power to the LED. The LEDs were powered by a 5 V DC input voltage from an Arduino board.

4.6 Supporting Information

Supporting Figures

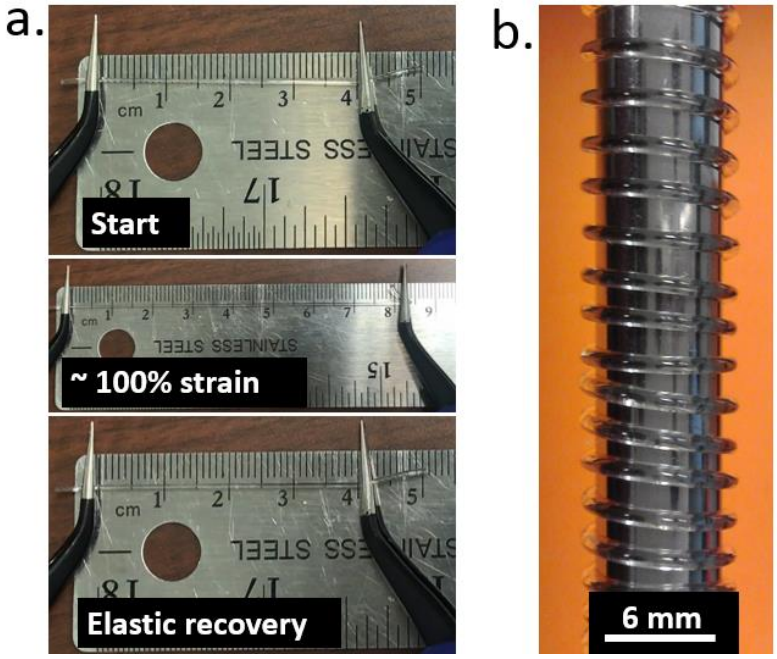

Figure S1: (a) Uniaxial tensile testing of the printed gel demonstrating the ability to be strained up to 100% and elastically recover, (b) Mechanical flexibility of printed gel filament

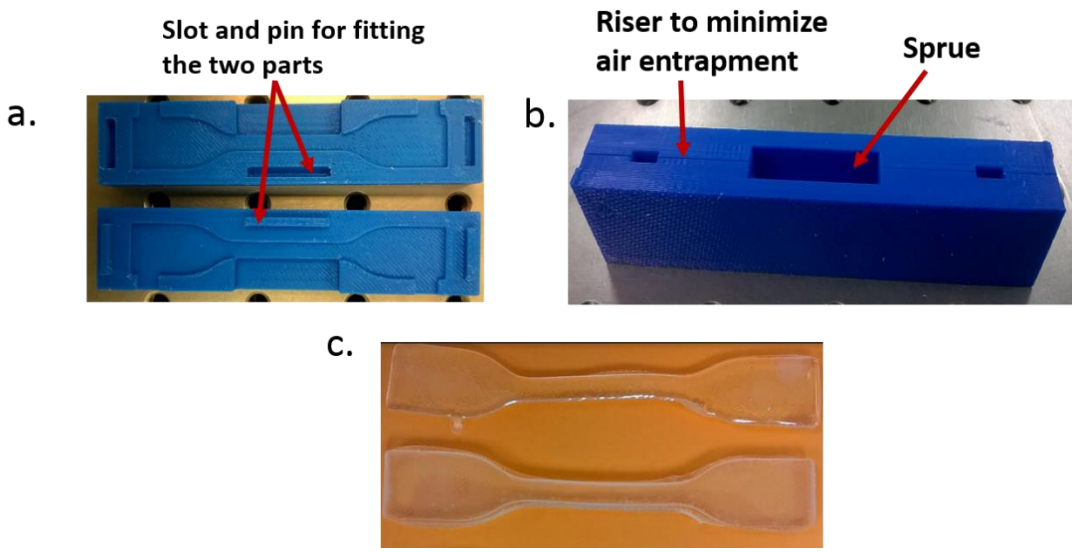

Figure S2: Process flow for molding dumb-bell test specimens. (a) A two- part mold; cope and drag format design to ensure uniform sample thickness, (b) Assembled mold, (c) Representative dumb-bell specimen of clear ballistic gel #20

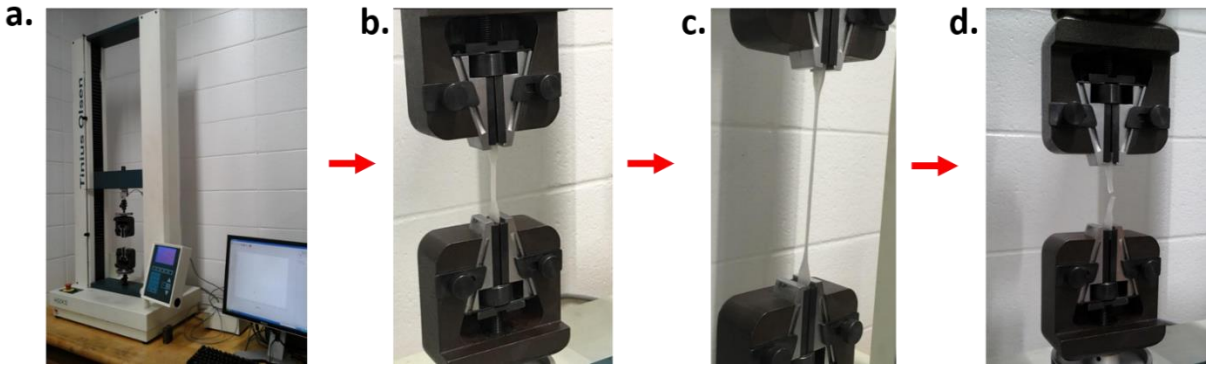

Figure S13: Images of experimental setup: (a) Tinus Olsen H50KS tensile testing machine use for the test, (b) Test piece clamped with no force applied (c) Test piece at maximum strain prior to failure (c) Sample returned to starting position after failure

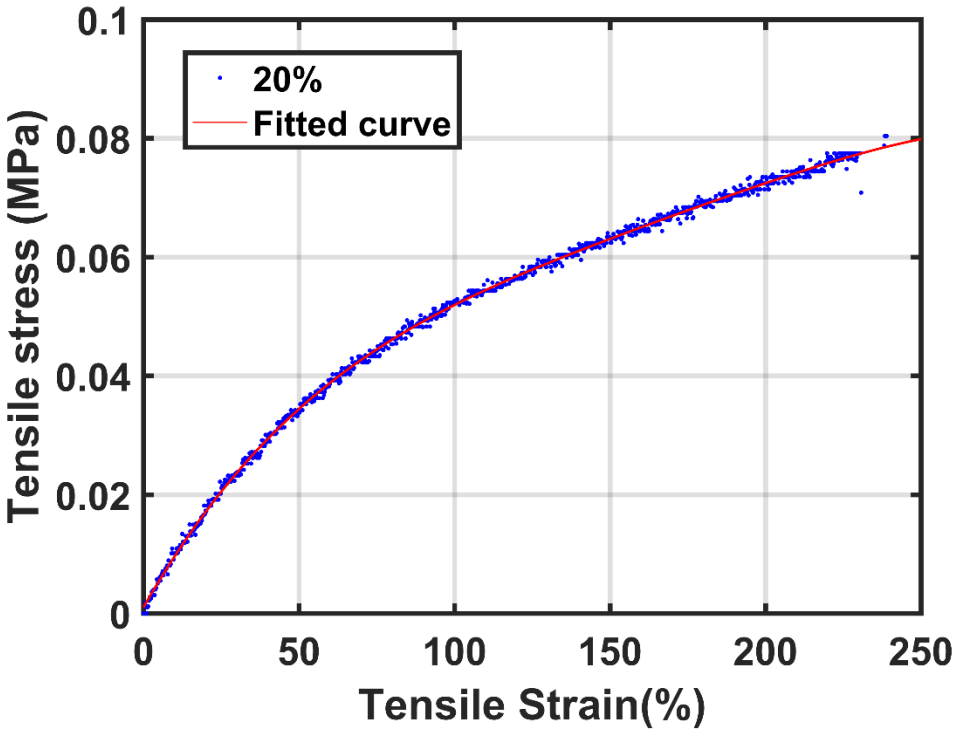

Figure S4: Engineering stress vs engineering strain curve for gel grade #20 at crosshead speed of 10mm/min resulting in strain rate of 0.0066s^{-1}

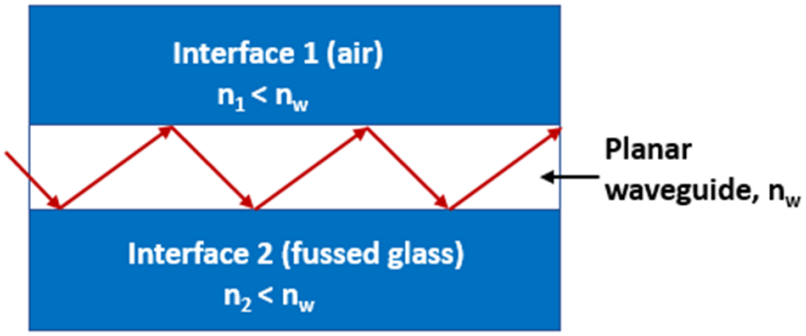

Figure S14: Illustration of the principle of waveguide

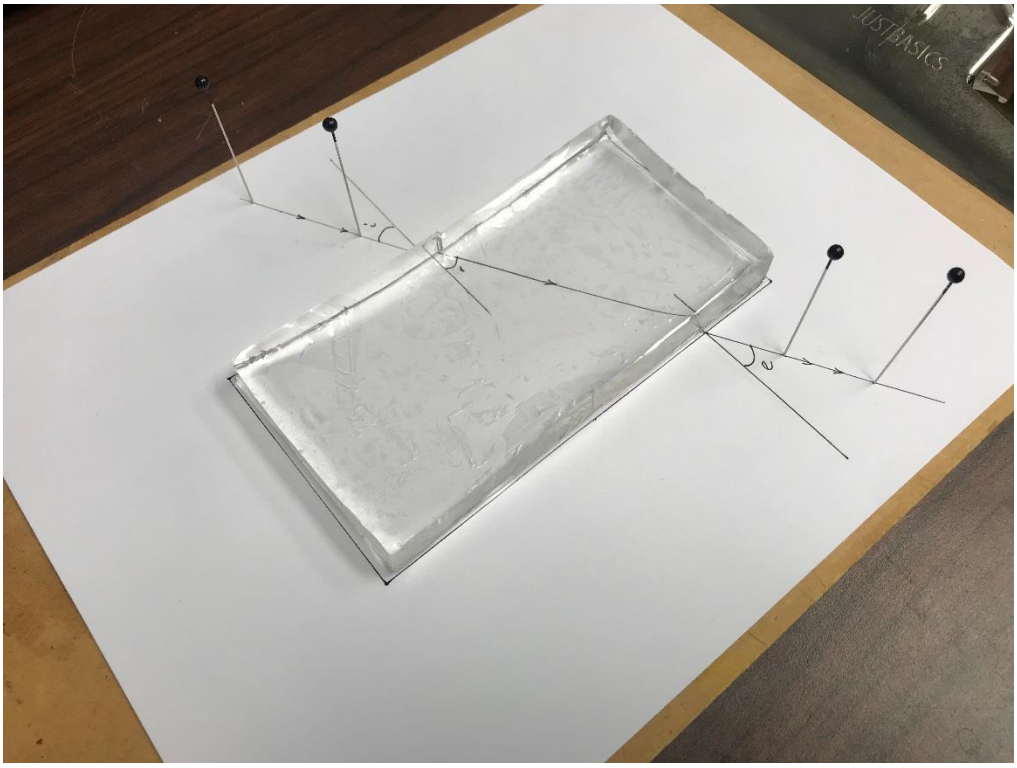

Figure S6: Experimental setup for measurement of refractive index by Snell's law

4.7 References

[1] Guo, J., Niu, M., and Yang, C., 2017, "Highly Flexible and Stretchable Optical Strain Sensing for Human Motion Detection," Optica, **4**(10) pp. 1285-1288.

[2] Leber, A., Cholst, B., Sandt, J., 2019, "Stretchable Thermoplastic Elastomer Optical Fibers for Sensing of Extreme Deformations," Advanced Functional Materials, **29**(5) pp. 1802629.

[3] Harnett, C. K., Zhao, H., and Shepherd, R. F., 2017, "Stretchable Optical Fibers: Threads for Strain-Sensitive Textiles," Advanced Materials Technologies, **2**(9) pp. 1700087-n/a.

[4] Butler, M., 1991, "Fiber Optic Sensor for Hydrogen Concentrations Near the Explosive Limit," Journal of the Electrochemical Society, 138(9) pp. L46-L47.

[5] Grant, S. A., and Glass, R. S., 1997, "A Sol–gel Based Fiber Optic Sensor for Local Blood pH Measurements," Sensors & Actuators: B. Chemical, 45(1) pp. 35-42.

[6] McDonagh, C., Burke, C., and MacCraith, B., 2008, "Optical Chemical Sensors," Chemical Reviews, 108(2) pp. 400-422.

[7] Klein, J., Stern, M., Franchin, G., 2015, "Additive Manufacturing of Optically Transparent Glass," 3d Printing and Additive Manufacturing, 2(3) pp. 92-105.

[8] Willis, K., Brockmeyer, E., Hudson, S., 2012, "rinted optics: 3D printing of embedded optical elements for interactive devices," Proceedings of the 25th annual ACM symposium on User interface software and technology, Anonymous pp. 589-598.

[9] Magnani, N., and Donnelly, J., ""Innovative Methods to Teach Optics in the Grade 5 Classroom," in Education and Training in Optics and Photonics, OSA Technical Digest Series (Optical Society of America, 2007), Paper ESD5.".

[10] Clear Ballistics, 2016, "Clear Ballistics: Synthetic Ballistic Gelatin," 2016(October 17).

[11] Kotz, F., Arnold, K., Bauer, W., 2017, "Three-Dimensional Printing of Transparent Fused Silica Glass," Nature, 544(7650) pp. 337-337.

[12] Clasen, R., and Schmidl, B., 1989, "Method of Manufacturing Glass Bodies by Means of Extrusion".

[13] Hülsenberg, D., Harnisch, A., and Bismarck, A., 2005, "Microstructuring of Glasses," Springer, 2005,

[14] Kotz, F., Schneider, N., Striegel, A., 2018, "Glassomer—Processing Fused Silica Glass Like a Polymer," Advanced Materials, 30(22) pp. e1707100-n/a.

[15] Ma, H., Jen, A., and Dalton, L., 2002, "Polymer-Based Optical Waveguides: Materials, Processing, and Devices," Advanced Materials, 14(19) pp. 1339-1365.

[16] Lorang, D., Tanaka, D., Spadaccini, C., 2011, "Photocurable Liquid Core-Fugitive Shell Printing of Optical Waveguides," Advanced Materials, 23(43) pp. 5055-5058.

[17] Hajj-Hassan, M., Gonzalez, T., Ghafar-Zadeh, E., 2008, "Direct-Dispense Polymeric Waveguides Platform for Optical Chemical Sensors," Sensors, 8(12) pp. 7636-7648.

[18] Parker, S., Domachuk, P., Amsden, J., 2009, "Biocompatible Silk Printed Optical Waveguides," Advanced Materials, 21(23) pp. 2411-2411.

[19] Micro Resist Technology, "OrmoClear® [Online] Https://Www.Microresist.De/En/Products/Hybrid-Polymers/Uv-Imprint-Uv-Moulding/ormoclear%C2%AE-Series [Accessed 19 March 2019],".

[20] Lawrence, B., Cronin-Golomb, M., Georgakoudi, I., 2008, "Bioactive Silk Protein Biomaterial Systems for Optical Devices," Biomacromolecules, 9(4) pp. 1214-1220.

[21] Udofia, E., and Zhou, W., 2019, "A Guiding Framework for Microextrusion Additive Manufacturing," Journal of Manufacturing Science and Engineering-Transactions of the Asme, 141(5) pp. 50801.

[22] Hinton, T. J., Hudson, A., Pusch, K., 2016, "3D Printing PDMS Elastomer in a Hydrophilic Support Bath Via Freeform Reversible Embedding," Acs Biomaterials Science & Engineering, 2(10) pp. 1781-1786.

[23] Muth, J. T., Vogt, D. M., Truby, R. L., 2014, "3D Printing: Embedded 3D Printing of Strain Sensors within Highly Stretchable Elastomers (Adv. Mater. 36/2014)," Advanced Materials, 26(36) pp. 6202-6202.

[24] Kiser, T., Eigensatz, M., Nguyen, M. M., 2013, "Architectural Caustics — Controlling Light with Geometry. in: Hesselgren L., Sharma S., Wallner J., Baldassini N., Bompas P., Raynaud J. (Eds) Advances in Architectural Geometry 2012. Springer, Vienna,".

[25] Wang, J., McMullen, C., Yao, P., 2017, "3D-Printed Peristaltic Microfluidic Systems Fabricated from Thermoplastic Elastomer," Microfluidics and Nanofluidics, 21(6) pp. 1.

[26] Kerr, W., Pellacini, F., and Denning, J., 2010, "BendyLights: Artistic Control of Direct Illumination by Curving Light Rays," Computer Graphics Forum, 29(4) pp. 1451-1459.

[27] CAMP, L., SHARMA, R., and FELDMAN, M., 1994, "Guided-Wave and Free-Space Optical Interconnects for Parallel-Processing Systems - a Comparison," Applied Optics, 33(26) pp. 6168-6180.

[28] Ecablemart Inc., ""Planar Lightwave Circuit Splitter", [Online]. Available: https://Docs.Google.Com/Viewer?url=http%3A%2F%2Fwww.Ecablemart.com%2Fpdf%2Ffbt-Splitter.Pdf [Accessed June 6, 2019]," .

[29] Garner, S. M., Lee, S., Chuyanov, V., 1999, "Three-Dimensional Integrated Optics using Polymers," IEEE Journal of Quantum Electronics, **35**(8) pp. 1146-1155.

CHAPTER 5

3D Printing of High-Temperature Microheater

New approaches are needed to enable design and fabrication of microheaters for high-temperature applicactions up to 1000^{o}C. While molybdenum disilicide ($MoSi_2$) is one of the primary high-performance materials used in commerical furncaces (with stable heating temperature up to 1800^{o}C) due to its high oxidation resistance, the fabrication process has proven inconvenient for the classical thin film depostion techniques. In this chapter, it is shown that the high-resolution printing capablilty and design freedom enabled by the microextrusion 3D printer makes it an appealing solution for creating low-cost customizable heaters from this material. Here, we provide a general overview of the current challenges including materials, fabrication, sintering, testing of the microheater and a simple prototype as a proof-of-concept demonstration of this method.

5.1 Introduction

Thermal related microdevices require corresponding heating platforms that can achieve with precision, high-temperature control in time and space. There are a variety of ways to accomplish this including laser beam, electron beam, as well as microheater[1, 2]. However, of all these, microheater stands out for its low energy consumption. A microheater is a small electro-mechanical device that emits heat in response to electrical current by Joule heating [3], and has been employed for several applications such as thermal inkjet printing[4], selective heat sintering [5], micro-ignition for micro-propulsion systems, gas sensors, micro-explosive boiling[6], microfluidic devices[7].

Using this technology, our group recently developed a new 3D printing method, referred to as Microheater Array Powder Sintering (MAPS) which employs an array of microheaters to

selectively sinter electronic materials [1]. However, the typical maximum heating temperature of the platinum microheaters is about 600^{o}C which is inadequate for many high-temperature applications (e.g., metal sintering) [6, 8, 9]. The ability to fabricate microheaters that can attend a 1000^{o}C target temperature may extend its range of applications, and this is the driving motivation for this work.

While molybdenum disilicide ($MoSi_2$) has attractive properties for making high temperature microheater, it is challenging to achieve a working microheater using the conventional thin film deposition process due to the formation of film with crystal structure that is different from that of the bulk material. In addition, this approach is burdened by extensive manual labor, usage of expensive equipment, material wastage, and long process cycle. These challenges have fueled the development and adoption of microextrusion 3D printing as an alternative fabrication method. It is the goal of this research to take advantage of the multi-material printing and rapid patterning ability of microextrusion printing to prototype a low-cost $MoSi_2$ based microheater.

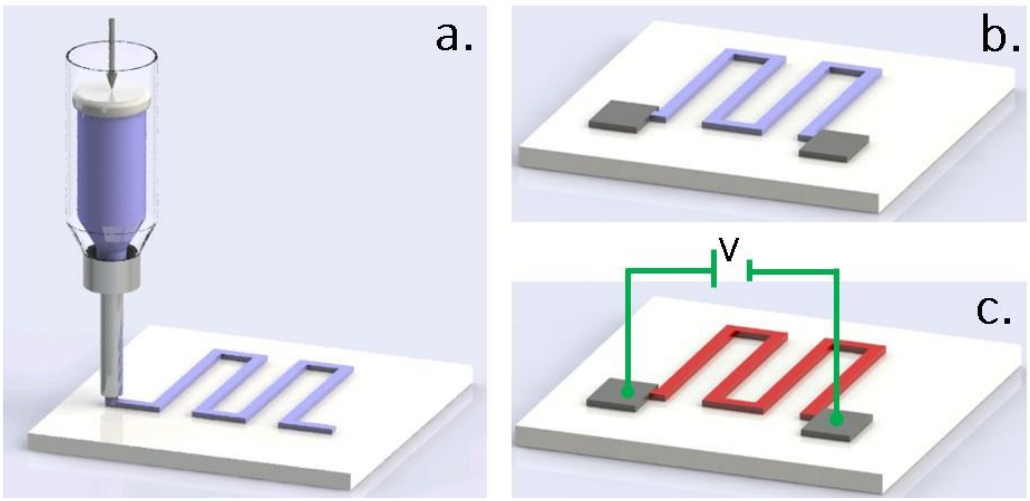

Figure 5.1: Overview of Microheater Fabrication process. (a) Schematic illustration of the microextrusion printing of concentrated MoSi2 ink. Operating principle of microheater – (b) non-activated state, (c) Activated state showing Joule heating.

In the microextrusion printing technique, a viscous $MoSi_2$ aqueous solution is first synthesized and dispensed through fine nozzles carried by an XYZ motion stage to pattern a predesigned heater geometry. To achieve electrical conductivity, the printed profile must be sintered in a non-oxidizing atmosphere. The performance of the heater is then evaluated by establishing electrical connection to a power source to achieve Joule heating. Figure 5.1 provides an overview of the μEP printing procedure and operating principle of a microheater.

5.2 Overview of Molybdenum Disilicide ($MoSi_2$) Microheater Fabrication

In this section, an overview of the process flow for fabricating a microheater with $MoSi_2$ is presented. We highlight some of the issues against successful microheater fabrication with $MoSi_2$ and corresponding approaches to address them.

5.2.1 Material Choice

In the simplest case, a microheater usually consists of three primary elements[10]:

(1) The resistive element,

(2) Substrate, and

(3) Conducive electrodes

Since the resistive element and substrate are the most crucial materials, it is necessary to provide a literature review on them. In the final analysis, the configuration, and material choice is predicated on the objective of achieving low power consumption, fast thermal response time, favorable heat confinement, good mechanical stability, and ease of fabrication.

5.2.1.1 Resistive Material – Molybdenum Disilicide ($MoSi_2$)

Among the resistive materials, molybdenum disilicide ($MoSi_2$) has demonstrated an attractive combination of excellent high-temperature oxidation resist ance and stability up to 1800^oC which

makes it a promising candidate material for microheaters [11-13]. The typical properties are presented in Table 5.1. However, at intermediate temperatures (370-700^{o}C) in air, especially at 500^{o}C, it suffers from accelerated deterioration into powdery mass (consisting mainly of MoO_3, SiO_2, and $MoSi_2$ residue), in a process widely referred to as "pesting", which limits its application. Yet, in an oxygen-rich environment and temperature above 1200^{o}C it forms a stable protective film of silica (through passive oxidation), which prohibits further oxidation upon subsequent exposure at the oxidizing temperature range [14].

The phenomenon of "$MoSi_2$ pesting" is understood to be catalyzed by structural and surface defects (e.g., pores, voids, and cracks), temperature, and formation of the non-volatile MoO_3 oxide product through the reaction:

$$2MoSi_2(s) + 7O_2(g) \rightarrow 2MoO_3(s) + 4SiO_2(s) \quad (5.1)$$

At temperatures above 1000^{o}C, the MoO_3 vaporizes, leaving a vitreous SiO_2 coating which seals and protects the surface from further oxidation. In contrast, "pesting" is attributed to the large volume expansion that results in conversion from $MoSi_2$ to MoO_3. This generates internal compressive stress that pushes the sample apart [15-19].

To obviate the pesting effect, different strategies such as alloying and protective film coating have been studied by several researchers. For instance, Yanagihara et al.[20] proposed alloying with aluminum due to its superior affinity for oxygen than silicon. This resulted in a lowering of the residual stress by the preferential formation of Al_2O_3 with lower volume expansion (~4.9%) than SiO_2 (~85%). In another study, it was revealed that the addition of 30-50% Si_3N_4 to $MoSi_2$ completely eliminated pesting by forming a protective scale of silicon oxynitride (Si_2ON_2) instead of MoS_3 [21], as well as long-term oxidation resistance at 1500^{o}C[22]. Nyutu et al.[23] studied the isothermal and cyclic oxidation behavior of $MoSi_2$-SiO_2 coating on molybdenum substrate.

The SiO_2 coating was found to give a four-fold increase in cyclic oxidation resistance at 1000^oC as opposed to $MoSi_2$ alone. The observed increase in oxidation resistance was credited to the excess silicon from silica which resulted in the formation of Mo_5Si_3 interlayers at high temperatures[24]. A similar observation was reported by another group [24, 25]. In their work, they reported that oxidation resistance of molybdenum silicate-based heaters (i.e., Mo_3Si, Mo_5Si_3, and $MoSi_2$) increased as the compositional ratio of Si to Mo increased. Furthermore, $MoSi_2$-SiC composite coating was reported to yield superior cyclic oxidation (~1492 cycles) than monolithic $MoSi_2$ coating due to the formation of relatively dense SiO_2 and Mo_9O_{26} composite oxide scale through the preferential oxidation of SiC particles followed by oxidation of $MoSi_2$ phase[26].

Different from oxidation, $MoSi_2$ presents several fabrication challenges. Magnetron sputtering remains one of the prevailing methods for depositing thin $MoSi_2$ films. However, there exist several variants of this technique including sputtering from $MoSi_2$ target[27, 28], co-sputtering of Mo and Si[29], and sputtering Mo on a Si substrate [30, 31]. Bulk molybdenum disilicide has a tetragonal structure. However, sputtered film properties often deviate from those of the bulk form, typically acquiring the less stable hexagonal phase, and require post-annealing at high temperature (~900^oC) to transform from hexagonal to tetragonal structure [25, 32, 33]. This means the crystal structure of the deposited film is altered by the sputtering technique.

Table 5.1: Material properties for MoSi2 Microheater

Properties	Materials		
	$MoSi_2$	Alumina	Silicon Nitride
Resistivity (Ω*m) @20ºC	$21x10^{-8}$	$>10^{18}$	10^{12} - 10^{13}
Thermal Conductivity (W/m*K)	60-70	25.12	15-20
Temperature Coefficient α per °C	$7.489x10^{-4}$	-	>3-3.9x10^11
Melting Temp. (°C)	2230	2040	1900
Specific Heat (J/kg*K)	403-430	800	691
Thermal Expansion (1/K)	5.1 x 10^{-6}	$7.5x10^{-6}$	$2.5x10^{-6}$
Density (kg/m^3)	6300	3970	3260
Young's Modulus (Pa)	430-$450x10^{12}$	$4x10^{11}$	$310x10^{9}$
Poison's Ratio	0.16-0.17	0.21	0.25
Shock resistance (ºC)	-	200	550
Purpose	Resistor	Substrate	Substrate
References	[11, 25, 34]	[35, 36]	[37, 38]

5.2.1.2 Substrate

The interest in high temperature microheaters places a demand for suitable high temperature substrates. Substrate provides the mechanical foundation upon which the heater is patterned, sintered and tested. Ideally, the substrate should have good mechanical robustness, chemical compatibility/inertness with the resistive material, thermal stability over a broad range of temperature, high electrical resistivity, low thermal conductivity, moderate expansion, and cost-effectiveness. On this note, different compatible high-temperature substrates were considered for potentially printing $MoSi_2$ heater as summarized in Table 5.1.

Considering chemical inertness to $MoSi_2$[13], and good substrate-film adhesion [27], alumina substrate became an excellent choice. The excellent bond strength obviates the need for the usual adhesion layer[6]. But alumina is poor in thermal shock resistance due to inherent brittleness and tensile thermal stresses. Thermal shock resistance is commonly measured as the maximum temperature difference that a material can withstand without cracking, and for alumina it is ~200ºC and 550ºC for Si_3N_4 determined from a quenching test [37]. The thermal resistance of material

depends on several factors including tensile strength, Young's modulus, Poisson's ratio, coefficient of thermal expansion, and thermal conductivity. Therefore, fast response time which is a desirable characteristic in a microheater is known to cause thermally induced cracking of substrates [39, 40]. For this reason, silicon composite substrates having superior resistance to shock in comparison to alumina was also considered as a possible alternative[37]. For example, Si_3N_4 possesses exceptionally high thermal shock resistance which makes it a promising candidate substrate. Although a previous work has reported $MoSi_2$ heater on Si_3N_4 substrate [24], Si_3N_4 is known to react with $MoSi_2$ at elevated temperature forming MoS_2-Si3N_4 composite matrix [21, 22].

5.3 Results and Discussion

The goal of this section is to introduce the reader to some of the significant results of this work, towards the realization of a functional $MoSi_2$ microheater. Discussion on materials selection, fabrication, sintering and testing are presented. Since the objective is to provide a demonstrative example of the viability of this technology, little attention is given to geometry optimization of the microheater. Hence, a simple design shown in Figure 5.1 was adopted. First, a preliminary study was conducted to test the feasibility of microextruion printing of a microheater using silver conductive ink as the resistive material (see appendix B for the results and discussion).

5.3.1 Ink Formulation

Successful microextrusion printing of the microheater depends strongly on the ability to formulate viscous $MoSi_2$ ink with appropriate rheology. Guided by the framework in Chapter 2, highly viscous $MoSi_2$ suspension was designed to meet the following constraints: 1). The ink must flow easily through fine needles when subjected to a shear force, 2). To minimize drying at the

nozzle tip during printing, appropriate solvent with low evaporation rate, should be selected for dispersing the $MoSi_2$ powder, 3). The ratio of the nozzle diameter (D)-to-the mean $MoSi_2$ particle diameter (a) (i.e., D/2a) should be greater than 100 to prevent nozzle clogging [41].

With these requirements in mind, appropriate ink rheology was realized from a mixture of $MoSi_2$ nanoparticle, ethylene glycol, and glycerol as humectants to promote bonding of the powder particles and adhesion to the substrate, while hydroxypropyl cellulose was added as a low-level binder, viscosifier and stabilizer [42, 43]. However, it should be noted that the organic content of the ink should be kept low because high organic content can trigger delamination of the ink from the substrate at fast sintering rates [44]. Furthermore, knowing that the starting properties of $MoSi_2$ powder plays a significant role in the pesting process, we evaluated pure (sample A) and a proprietary composite (sample B) $MoSi_2$ powders for making the ink (Table 5.2)

Table 5.2: Samples of $MoSi_2$ used for the test

Sample	Supplier	Particle size (nm)
A	US Research Nanomaterials, Inc.	300
B	I Squared Element, Co., Inc.	600

Sample A is commercially available while sample B is a proprietary $MoSi_2$ powder used in bulk furnaces and was kindly provided by the supplier for this research. The detailed protocol of ink formulation is presented in the experimental section.

5.3.2 Substrate

Having discussed the common limiting factors in substrate selection for high-temperature applications in section 5.2.1.2, alumina (Al_2O_3) and silicon nitride (Si_3N_4) substrates were chosen and evaluated for their suitability for making the microheater. Alumina was chosen due to its chemical inertness, good bond strength with $MoSi_2$, low thermal conductivity, and high melting temperature. However, as was revealed in the preliminary test (see appendix B), alumina is poor

in thermal shock, and for this reason, other candidates were considered. A careful evaluation of other commercially available alumina materials was done, and we selected a propriety NanoFractalAlumina™ substrate because of its superior shock resistance [45] to pure alumina. In addition, a Si_3N_4 substrate (10×10 mm^2, thickness: 1mm), one-sided polished was used for its excellent shock resistance and low thermal conductivity[38].

5.3.3 Microextrusion 3D printing

Printing of the microheater was carried out using the microextrusion printer described in Chapter 3. The heater pattern (Figure 5.1b) was predesigned in SolidWorks to generate the printing pathway. Guided by the microextrusion printing framework detailed in Chapter 3, a printed profile with width of 196 μm was achieved using a 160 μm dispensing nozzle. The effective heating area consists of a serpentine filament having a width of ~200 μm, and the length of the folds are 500μm and a total area of 1500 x 2000 μm as shown in Figure 5.2.

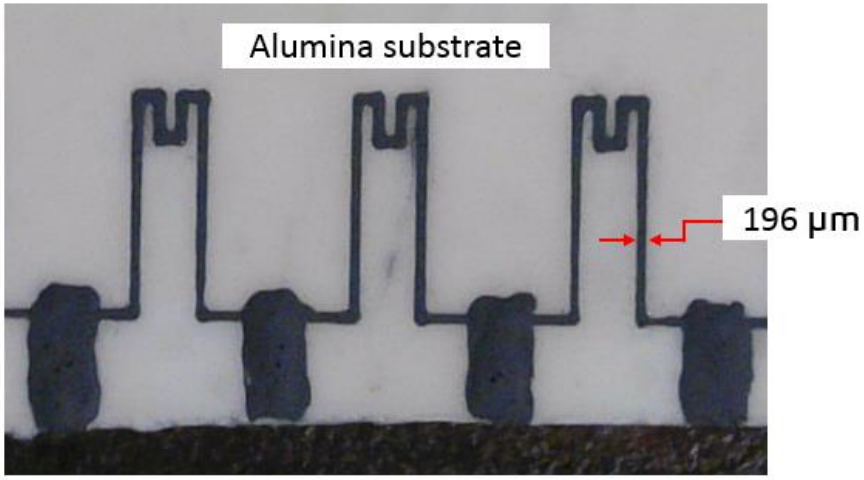

Figure 5.2: As printed $MoSi_2$ heater profile using uEP.

The current print resolution was limited by several factors including particle sizes of the $MoSi_2$ powder used in preparing the ink. For example, according to our framework, the 300 nm particle size limits the minimum usable nozzle to about 70 μm. Several attempts to print with smaller

nozzles were not successful due to ink coagulation and clogging of the nozzle tip. This difficulty was further aggravated by the fact that the substrate was not perfectly flat and relatively rough leading to damage to the glass nozzle. For instance, printing with a ~30 μm requires a standoff distance of about 30 μm. Therefore, the surface roughness of the substrate can be detrimental to the printing process. Because of these constraints, it became necessary to carefully examine each factor and it was determined that 160 μm was the minimum nozzle to obtain consistent and repeatable prints. Theoretically, this spatial resolution could be significantly improved through careful optimization of ink design (e.g., ball milling the powder size to a few nanometer), use of smaller nozzles, and finely polished substrates. Nevertheless, simplicity of the fabrication process renders this approach very competitive in cost for creating customizable heaters.

5.3.4 Sintering

Generally, sintering can be accomplished at temperatures above one-half of the bulk material melting temperature (T_m). However, with micro and nanoparticles, the story is different since they are known to sinter at much lower temperatures. For example, with nanoparticles, sintering can be initiated between 0.2 - 0.3 of the melting temperatures [46]. Buffat and Borel provided an equation to estimate the appropriate sintering temperature (Eq. 5.2).

$$T_s = T_m * \left(1 - \frac{2}{\rho_s L r}\left[\gamma_s - \gamma_l \left(\frac{\rho_s}{\rho_l}\right)^{2/3}\right]\right) \quad (5.2)$$

Where γ is the surface tension, ρ is the density, T_0 is the melting temperature of bulk metal, L is the latent heat of fusion, and r is the radius of the nanoparticle. The subscripts s and l denote solid and liquid, respectively. Lowering of the sintering temperature can be beneficial for extending the range of usable substrates and energy requirements.

In this work, sintering was accomplished by first drying the printed samples at room temperature for 5 hours, followed by mild heating in an oven at 150^{o}C to drive out the solvents and other organic components. A second and final sintering step was performed at temperatures above 1000^{o}C (i.e., one-half of the bulk melting temperature of the material) due to the microscale particle size, either in air or hydrogen atmospheres. Using the ink prepared from commercially available $MoSi_2$, an initial sintering experiments in atmospheric condition verified the pesting phenomenon (Figure 5.3). For this test, the ink was manually applied on an alumina substrate.

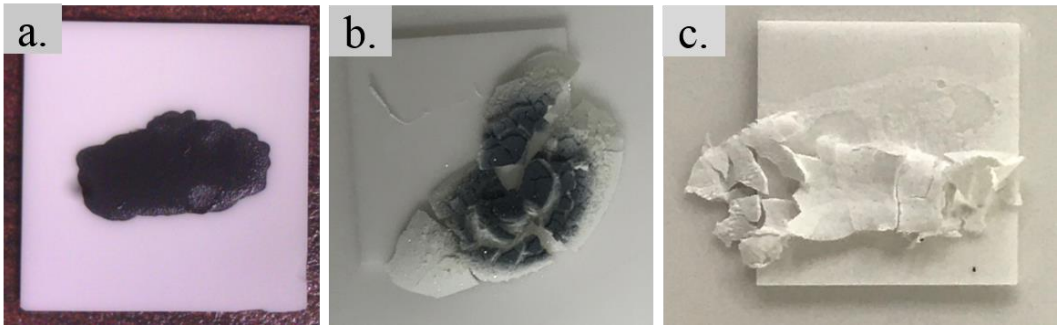

Figure 5.3: Observation of Pesting in $MoSi_2$ films. (a) MoSi2 film after drying at 150^{o}C for 5 mins.; (b) sample after sintering at 600^{o}C for 30 mins.; (c) Sample after sintering at 1100^{o}C for 30 mins. @ a rate of 5^{o}C/min.

Although no actual analysis of the resulting films was carried out to determine the compositions, a visual examination of Figure 5.3 agrees with the general trend reported in the literature[25, 27]. That is, sintering in an oxidizing atmosphere results in oxidization, and debonding of the printed ink is from the substrate. In order to make definite conclusions on the products of the reaction, further testing and analysis of the samples will be required. By comparing Figure 5.3(b) and (c), we believe the longer sintering time provided ample time for complete oxidation of the films. It is known that $MoSi_2$ heaters are susceptible to time dependent deteriorating when used in an oxidizing atmosphere[24].

In another test, and to explore the possibility of overcoming the oxidation issue (and achieve sintering in air), sample B with superior oxidation resistance, consisting of molybdenum disilicide and a glassy phase of silicon dioxide (SiO_2) was evaluated. A similar test procedure applied for sample A was followed. Interestingly, no visible oxidation was observed for this sample. Nevertheless, no electrical conductivity was recorded over a range of sintering temperatures (1000-1600^{o}C). Following this outcome and the results from the literature, we concluded that the heater must be sintered in a non-oxidizing atmosphere to achieve electrical conductivity. Therefore, successful sintering of both samples were accomplished at 1500^{o}C in hydrogen atmosphere at a ramp rate of 3^{o}C min^{-1} and left to soak for 1 hr. to achieve full sintering (Figure 5.4).

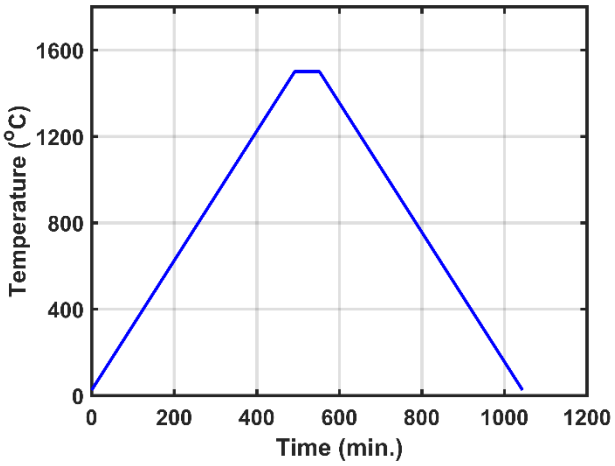

Figure 5.4: Final sintering profile for $MoSi_2$ heater in hydrogen

It was hypothesized that the sintering process is controlled by the particle size, temperature and dwell time. In this test, only a single firing temperature was studied, and was therefore not optimized. This resulted in one common problem, while all the tested samples (both the commercially available $MoSi_2$ powder and the proprietary $MoSi_2$) were conductive, only one sample in each case of NanoFractalAlumina™ substrate (Figure 5.5), alumina substrate (Figure

5.6) and silicon nitride substrate, (Figure 5.7) was found to be continuous. The discontinuity was observed in the patterns around the effective heating area while the larger electrode portion (with much thicker film) were continuous. It was speculated that the discontinuity resulted from the long soak time (1 hour), giving rise to evaporation or combustion of some of the films. The percentage binder content could also be responsible for this observation. This reasoning was reinforced by the presence of voids, possibly due to the combustion of the organic binders. Further testing will be needed to arrive at appropriate ink design and sintering condition.

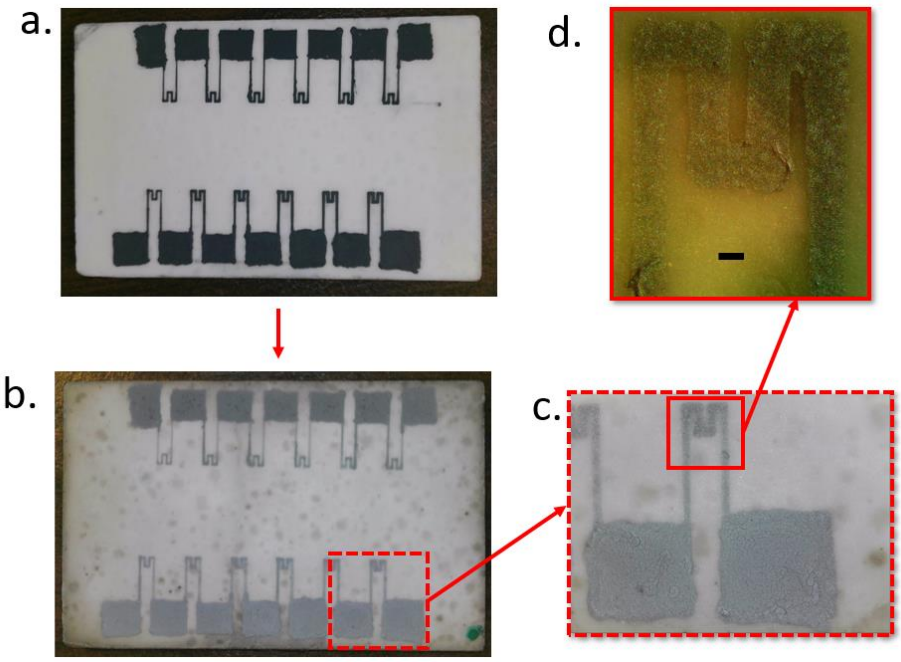

Figure 5.5: Photomicrographs of (a) as-printed $MoSi_2$ heater array on NanoFractalAlumina™ substrate, (b) sintered patterns at 1500°C for 60 min, and (c) magnified image of sintered samples; (d) optical image of sintered samples. Scale bar = 200μm.

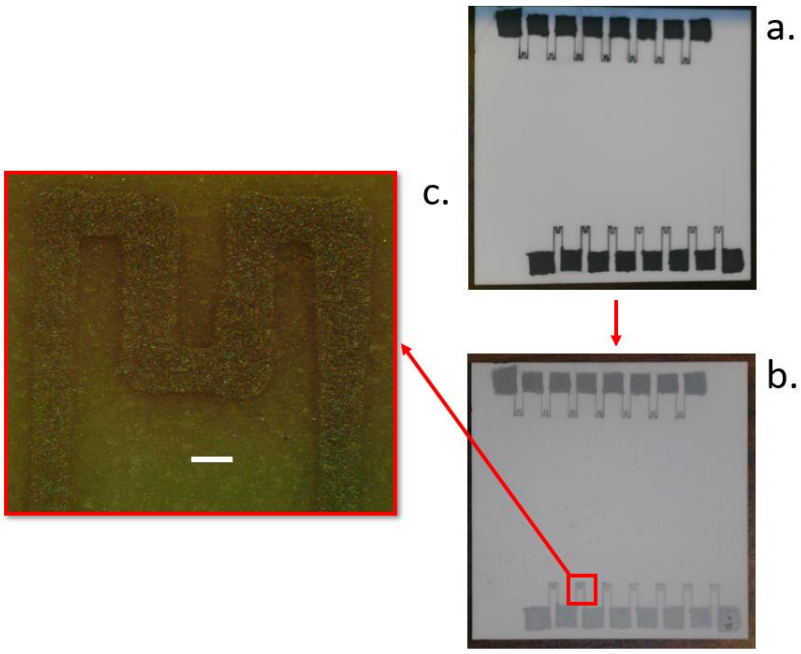

Figure 5.6: Photomicrographs of (a) as-printed $MoSi_2$ heater array on an alumina substrate, (b) sintered patterns at 1500^{o}C for 60 min., (c) optical image of the sintered sample. Scale bar = 200μm.

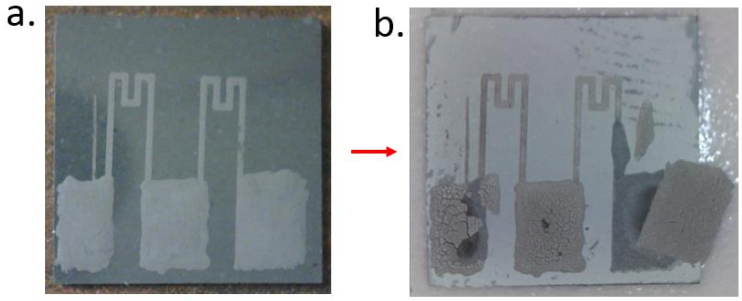

Figure 5.7: Photomicrographs of (a) as-printed $MoSi_2$ heater array on silicon nitride substrate, (b) sintered patterns at 1500^{o}C for 60 min.

The heaters showed good adhesion on the two types of alumina substrate. Meanwhile, delamination was observed for silicon nitride substrate. While $MoSi_2$ is known to have good adhesion to alumina substrate [27], the superior adhesion to alumina could also be due to the roughness of the substrates since Si_3N_4 substrate was polished.

5.3.5 Testing

After sintering in the furnace, electrical connection to the external circuitry was achieved by bonding copper conductive tape directly to the extended using silver epoxy (see experimental section). A representative of a completed heater with the necessary electrical connection is shown in Figure 5.8.

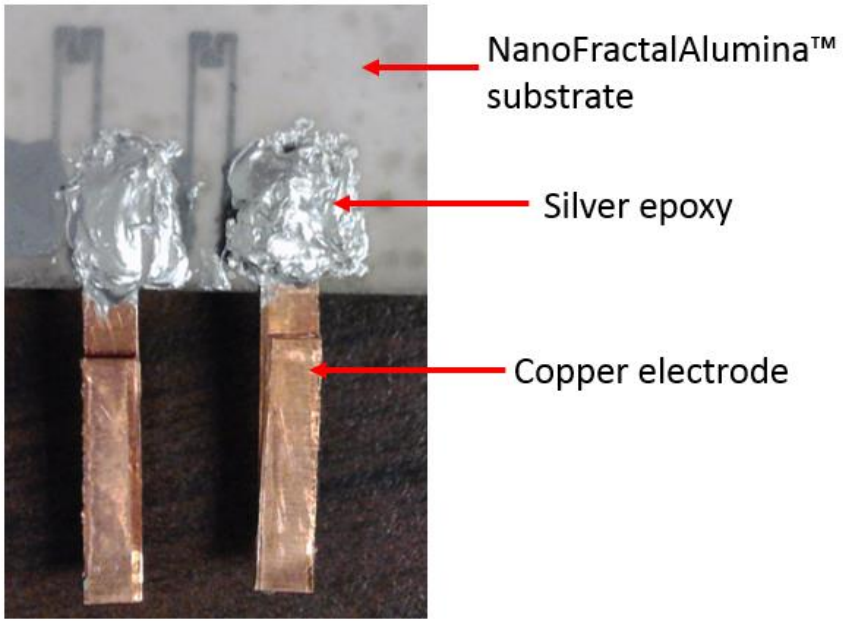

Figure 5.8: Fabricated $MoSi_2$ heater on NanoFractalAlumina™ substrate with electrical connection accomplished with a silver epoxy

The power supply was provided through a variable linear DC supply (Tekpower, TP3005T). To study the relationship between the power input and temperature of the microheater, two methods were employed to measure the surface temperature of the microheater (see appendix B). First, the temperature at the center of the heater was measured using a K-type thermocouple (with a tip diameter ~200μm), having direct contact with the substrate surface. Second, to compare the performance of the temperature measured by the thermocouple, an IR camera which has a 0.05°C

thermal sensitivity and 320 x 240-pixel resolution (FLIR T300, FLIR, USA) was also used. The initial resistances of the heaters measured at room temperature before connection to the power source were 139 Ω (on NanoFractalAlumina™ substrate) and 249 Ω (on alumina substrate). NanoFractalAlumina™ substrate had a high surface roughness, which made it difficult to achieve uniform feature width. The average print resolution on NanoFractalAlumina™ was ~230μm compared to ~200 μm on alumina with better smoothness.

The heater was turned on for roughly 60 seconds for different voltage values (0 – 30 V). A temperature increase of ~2^{o}C was recorded for both 5V and 10V. When the voltage was 15V, electrical continuity was lost in the circuit. To verify this, the electrical resistance of the heater was measured with a digital multimeter (Fluke 199 True RMS Digital multimeter). The resistance values were in the range of MΩ. We believe evaporation of organic binders left gaps between the $MoSi_2$ which resulted in the loss of electrical contact.

5.4 Conclusions

In this chapter, we presented a study on the feasibility of 3D printing of a high temperature microheater using molybdenum disilicide as the resistive element, with the goal of achieving a target temperature of 1000^{o}C. The preliminary results demonstrated through the printed microheater prototype shows that microextrusion printing of the microheater is indeed possible. While the performance of the heater has not been characterized at this time, mainly due to resource limitation, significant progress has been made towards the realization of our goal of printing a functional high temperature microheater.

The primary findings of this work can be summarized as follows.

1). We evaluated two commercially available $MoSi_2$ for making the microheater and developed a protocol for formulating printable ink from this material. Although the printed resolution was limited to about 200μm, using this protocol the print resolution can further be improved by using powder with nanoparticle size.

2). Although ceramic materials can withstand high temperature, they are prone to cracking when subjected to rapid changes in temperature. Therefore, issues such as cracking, and delamination of printed features are some of the common challenges that could potentially stand in the way of achieving a high-temperature application. On this front, we researched and identified a commercially available composite alumina substrate and Si_3N_4 as good candidate materials with good shock resistance.

3). Regarding sintering, while the present work was limited in establishing an optimized sintering temperature, it did identify a baseline temperature and atmosphere needed to achieve conductive feature and overcome pesting. This is a big step in achieving a working microheater. Building on this success, further optimization of the sintering profile will be required in the future to achieve improved electrical conductivity.

4). Despite unsuccessful testing and characterization of the microheater, we have demonstrated a simple, yet low-cost method to test and characterize the microheater using a thermocouple and thermal camera before a more robust control and feedback system is implemented. The preliminary results from the silver microheater verified the effectiveness of the experimental setup.

To our knowledge, this is the first reported effort towards making a microheater from $MoSi_2$ using microextrusion 3D printing. There, having demonstrated the feasibility of this approach, this work provides the necessary scientific foundation upon which future work can be based.

5.5 Experimental Methods

Ink preparation: Molybdenum Disilicide inks were synthesized directly from $MoSi_2$ nanopowder with a mean diameter of 300 nm, 99.9% purity, and α-type crystal structure (US-Nano) and a propriety $MoSi_2$ powder with mean diameter ~6.0 μm.

(1) The ink was prepared by first dissolving 10g of $MoSi_2$ in 110 mL of deionized water and 40 mL of ethylene glycol.

(2) The resulting suspension was centrifuged at 2500 rpm for 4 hours to collect fine particles.

(3) The collected nanoparticle was then re-dispersed with the appropriate addition of glycerol, 3.5 wt% aqueous hydroxyethyl cellulose solution, 3.0 wt% aqueous hydroxyethyl cellulose solution, followed by stirring at 2000 rpm for 5 minutes using a homogenization mixer to enhance homogenization of the ink.

Packaging: After sintering in the furnace, electrical connection to external circuitry was achieved through the following step:

(1) A copper electrode of ~2 mm in width and 0.5 mm thick was appended to the extended part of the $MoSi_2$ film;

(2) A silver epoxy [47], which was applied manually using a 150 μm dispensing needle was used to bond the electrode to the heater;

(3) This was followed by baking in an oven at 120^{o}C for 2 hours to cure the epoxy. A representative of a completed heater with the necessary electrical connections is shown in Figure 5.8.

5.6 References

[1] Holt, N., Van Horn, A., Montazeri, M., 2018, "Microheater Array Powder Sintering: A Novel Additive Manufacturing Process," Journal of Manufacturing Processes, 31pp. 536-551.

[2] Ming, L., and Bassett, W. A., 1974, "Laser Heating in the Diamond Anvil Press Up to 2000°C Sustained and 3000°C Pulsed at Pressures Up to 260 Kilobars," Review of Scientific Instruments, 45(9) pp. 1115-1118.

[3] Hwang, W., Shin, K., Roh, J., 2011, "Development of Micro-Heaters with Optimized Temperature Compensation Design for Gas Sensors," Sensors, 11(3) pp. 2580-2591.

[4] Setti, L., Piana, C., Bonazzi, S., 2004, "Thermal Inkjet Technology for the Microdeposition of Biological Molecules as a Viable Route for the Realization of Biosensors," Analytical Letters, 37(8) pp. 1559-1570.

[5] Baumers, M., Tuck, C., and Hague, R., "Selective Heat Sintering Versus Laser Sintering: Comparison of Deposition Rate, Process Energy Consumption and Cost Performance".

[6] Zhang, K. L., Chou, S. K., and Ang, S. S., 2007, "Fabrication, Modeling and Testing of a Thin Film Au/Ti Microheater," International Journal of Thermal Sciences, 46(6) pp. 580-588.

[7] Son, J., Lee, J., Kim, J., 2015, "Temperature Distribution Measurement of Au Micro-Heater in Microfluidic Channel using IR Microscope," International Journal of Precision Engineering and Manufacturing, 16(2) pp. 367-372.

[8] Holt, N., Marques, L., Van Horn, A., 2018, "Fabrication and Control of a Microheater Array for Microheater Array Powder Sintering," International Journal of Advanced Manufacturing Technology, 95(1-4) pp. 1369-1376.

[9] Ali, S. Z., Udrea, F., Milne, W. I., 2008, "Tungsten-Based SOI Microhotplates for Smart Gas Sensors," Journal of Microelectromechanical Systems, 17(6) pp. 1408-1417.

[10] VanHorn, A., and Zhou, W., 2016, "Design and Optimization of a High Temperature Microheater for Inkjet Deposition," International Journal of Advanced Manufacturing Technology, 86(9-12) pp. 3101-3111.

[11] Azo Materials, "Properties of Molydenum Disilicide.
Available: Https://Www.Azom.Com/Properties.Aspx?ArticleID=512".

[12] Shah, D. M., 1992, "MoSi2 and other Silicides as High Temperature Structural Materials".

[13] Wirkus, C. D., and Wilder, D. R., 1966, "High-Temperature Oxidation of Molybdenum Disilicide," Journal of the American Ceramic Society, 49(4) pp. 173-177.

[14] Meschter, P., 1992, "Low-Temperature Oxidation of Molybdenum Disilicide," Metallurgical Transactions a-Physical Metallurgy and Materials Science, 23(6) pp. 1763-1772.

[15] Chou, T., and Nieh, T., 1993, "Mechanism of Mosi2 Pest during Low-Temperature Oxidation," Journal of Materials Research, 8(1) pp. 214-226.

[16] Xu, J., Li, Z., Munroe, P., 2014, "Oxidation Resistance of Mo(Si1−xAlx)2 Nanocrystalline Films and Characterization of their Oxide Scales by Electrochemical Impedance Spectroscopy," RSC Adv, 4(99) pp. 55696-5578.

[17] Mitra, R., 2017, "Intermetallic Matrix Composites: Properties and Applications," Elsevier.

[18] Mckamey, C., Tortorelli, P., Devan, J., 1992, "A Study of Pest Oxidation in Polycrystalline Mosi2," Journal of Materials Research, 7(10) pp. 2747-2755.

[19] Peizhong, F., Xuanhui, Q., Islam, S. H., 2007, "Low-Temperature Oxidation Behavior of MoSi2 Powders," Journal of University of Science and Technology Beijing, Mineral, Metallurgy, Material, 14(6) pp. 558-561.

[20] Yanagihara, K., Maruyama, T., and Nagata, K., 1996, "Effect of Third Elements on the Pesting Suppression of Mo-Si-X Intermetallics (X=Al, Ta, Ti, Zr and Y)," Intermetallics, 4pp. S133-S139.

[21] Hebsur, M.G., and NASA Glenn Research Center, 2001, "Development of tough, strong, and pest-resistant $MoSi_2$-ÝSi_3N_4 composites for high-temperature structural applications," National Aeronautics and Space Administration, Glenn Research Center, 210807; NASA/TM-2001-210807, Hanover, MD; Cleveland, Ohio.

[22] Klemm, H., and Schubert, C., 2001, "Silicon Nitride/Molybdenum Disilicide Composite with Superior Long-Term Oxidation Resistance at 1500°C," Journal of the American Ceramic Society, 84(10) pp. 2430-2432.

[23] Nyutu, E., Kmetz, M., and Suib, S., 2006, "Formation of MoSi2-SiO2 Coatings on Molybdenum Substrates by CVD/MOCVD," Surface & Coatings Technology, 200(12-13) pp. 3980-3986.

[24] Hayashi, T., Sato, Y., and Yoshikado, S., 2010, "Evaluation of the Structures and Oxidation Resistances of MoSi2-Si Composite Thin Films," Key Engineering Materials, Vol. 445pp. 148-151.

[25] Itoh, Y., Satoh, M., Wakisaka, K., 2009, "Improvement of Heating Characteristics of Molydenum Silicide Thin Film Electric Heaters," Electrical Engineering in Japan, 168(2) pp. 452-458.

[26] Yoon, J., Lee, K., Kim, G., 2004, "Low-Temperature Cyclic Oxidation Behavior of MoSi2/SiC Nanocomposite Coating Formed on Mo Substrate," Materials Transactions, 45(7) pp. 2435-2442.

[27] Itoh, Y., Wakisaka, K., Satoh, M., 2006, "Fabrication and Application of MOSi2 Thin-Film Electric Heaters," Electroceramics in Japan Ix, 320pp. 95-98.

[28] Chou, T., and Nieh, T., 1994, "Pest Disintegration of Thin Mosi2 Films by Oxidation at 500-Degrees-C," Journal of Materials Science, 29(11) pp. 2963-2967.

[29] Murarka, S. P., Fraser, D. B., Retajczyk, T. F., 1980, "Cosputtered Molybdenum Silicides on Thermal SiO2," Journal of Applied Physics, 51(10) pp. 5380-5385.

[30] Pantel, R., 1984, "Low Resistivity Thin Film Refractory Silicides Grown in Ultrahigh Vacuum at Low Temperature," Journal of the Electrochemical Society, 131(10) pp. 2426.

[31] Doland, C. M., 1988, "Molybdenum Silicide Formation on Single Crystal, Polycrystalline and Amorphous Silicon: Growth, Structure and Electrical Properties".

[32] Dheurle, F., Petersson, C., and Tsai, M., 1980, "Observations on the Hexagonal Form of Mosi2 and Wsi2 Films Produced by Ion-Implantation and on Related Snowplow Effects," Journal of Applied Physics, 51(11) pp. 5976-5980.

[33] Qiao, Y., Zhang, H., Hong, C., 2009, "Phase Stability, Electronic Structure and Mechanical Properties of Molybdenum Disilicide: A First-Principles Investigation," Journal of Physics D: Applied Physics, 42(10) pp. 105413.

[34] US Reasearch Nanomaterials, 2018, "Molybdenum Disilicide (MoSi2) Nanopowder. Available: Http://Www.Us-Nano.Com/Inc/Sdetail/38604 ".

[35] MTI Corporation, 2018, "Properties of Al2O3 Wafer. Available: Http://Www.Mtixtl.Com/AL-R-101005S1.Aspx,".

[36] Toskov, S., Glatz, R., Miskovic, G., 2013, "Modeling and fabrication of Pt micro-heaters built on alumina Substrate," 2013 36th International Spring Seminar on Electronics Technology, ISSE 2013, May 8, 2013 - May 12, Anonymous IEEE Computer Society, Alba Iulia, Romania, pp. 47-52.

[37] Kyocera Group, "Heat to Withstand Extreme Temperatures: Https://Global.Kyocera.Com/Fcworld/Charact/Heat/Heatresist.Html. [Accessed 12 December 2018]".

[38] MTI Corporation, ""Silicon Nitride Ceramic Substrat", [Online]. Available: https://Www.Mtixtl.Com/Si3N4-101010S1.Aspx . [Accessed 14 January 2019]".

[39] Cai, Z. X., Zeng, X. Y., and Duan, J., 2011, "Fabrication of Platinum Microheater on Alumina Substrate by Micro-Pen and Laser Sintering," Thin Solid Films, 519(11) pp. 3893-3896.

[40] Prudenziati, M., and Hormadaly, J., 2012, "Printed Films: Materials Science and Applications in Sensors, Electronics and Photonics," NewsRX LLC, pp. 290.

[41] Lewis, J. A., and Gratson, G. M., 2004, "Direct Writing in Three Dimensions," Materials Today, 7(7) pp. 32-39.

[42] Sun, K., Wei, T., Ahn, B. Y., 2013, "3D Printing of Interdigitated Li-Ion Microbattery Architectures," Advanced Materials, 25(33) pp. 4539-4543.

[43] Liang, Y. T., and Hersam, M. C., 2010, "Highly Concentrated Graphene Solutions Via Polymer Enhanced Solvent Exfoliation and Iterative Solvent Exchange," Journal of the American Chemical Society, 132(50) pp. 17661-17663.

[44] Ermak, O., Zenou, M., Toker, G. B., 2016, "Rapid Laser Sintering of Metal Nano-Particles Inks," Nanotechnology, 27(38) pp. 385201.

[45] Micropyretics Heaters International, "NanoFractalAlumina™: https://Mhi-Inc.Com/Store/Ceramic-Products/Nanofractalalumina/Rectangular-Plates/Alumina-Rectangular-Plate-45mm-X-28mm-X-4mm. [Accessed 14 January, 2019]".

[46] Groza, J., 1999, "Nanosintering," Nanostructured Materials, 12(5-8) pp. 987-992.

[47] ConductiveX, ""Electrically & Thermally Conductive 1 Part Silver Epoxy Heat Cure High Temp 325F", [Online]. Https://Conductivex.Com/Electrically-Conductive-Epoxies/Silver%20Electrically%20Conductive%20Epoxy/Electrically-Thermally-Conductive-1-Part-Silver-Epoxy-Heat-Cure-High-Temp-325F. [Accessed 14 January 2019]".

5.7 Appendix B

Printing of Silver Microheater

The purpose of this experiment was to explore the potential of fabricating a microheater using microextrusion printing technology. Silver based microheaters have been fabricated for various heating applications requiring low-medium operating temperatures (typically in the range of 60 to 400^{o}C), such as transparent & flexible heaters[1, 2], thermal regulation in microfluidic device[3, 4]. Here, silver paste was chosen due to its relatively low cost and was available at our lab. Since the objective was to demonstrate the feasibility of printing a functional microheater, no attention was given to the aesthetics of the fabricated product, and as a result the device demonstrated here may appear crude.

B.1 Ink

Commercially available silver nanoparticles ink, PFI-600 Conductive Flexo (NovaCentrix, USA) [5] was used for this test. This was chosen because it was readily available in our lab. However, because PFI-600 is a flexographic/ gravure ink, it is designed for fast drying, and as detailed in chapter 2, fast drying prevented successful printing with fine nozzles.

B.2 Fabrication Procedure

The fabrication of the silver microheater followed the same procedure outlined in Chapter 4 of this dissertation. Since microextrusion printing does not place any restrictions on the usable substrate, different substrates were investigated for this study including PTE, glass, and silicon. However, because this preliminary experiment was conducted to determine a potential substrate for high temperature and fast response heater, an alumina substrate was chosen due to its chemical inertness, and high melting temperature. The alumina substrate had an area of 20mm x 20mm, and

~1mm in thickness. For this experiment, a 100μm nozzle was used with printing speed 1-2mm/s and pressure range of 1-10 psi. Several attempts at using finer nozzles were unsuccessful due to fast drying that triggered nozzle clogging. As per the manufacturer's instruction, after printing, the microheater was sintered at 80^{o}C for 5 minutes. Thereafter, electrical connection to external circuitry was achieved through the following steps:

(4) A copper electrode of ~2mm in width and 0.5mm thick was appended to the extended part of the silver film;

(5) A Kapton tape was used to bond the copper electrode to the resistive material.

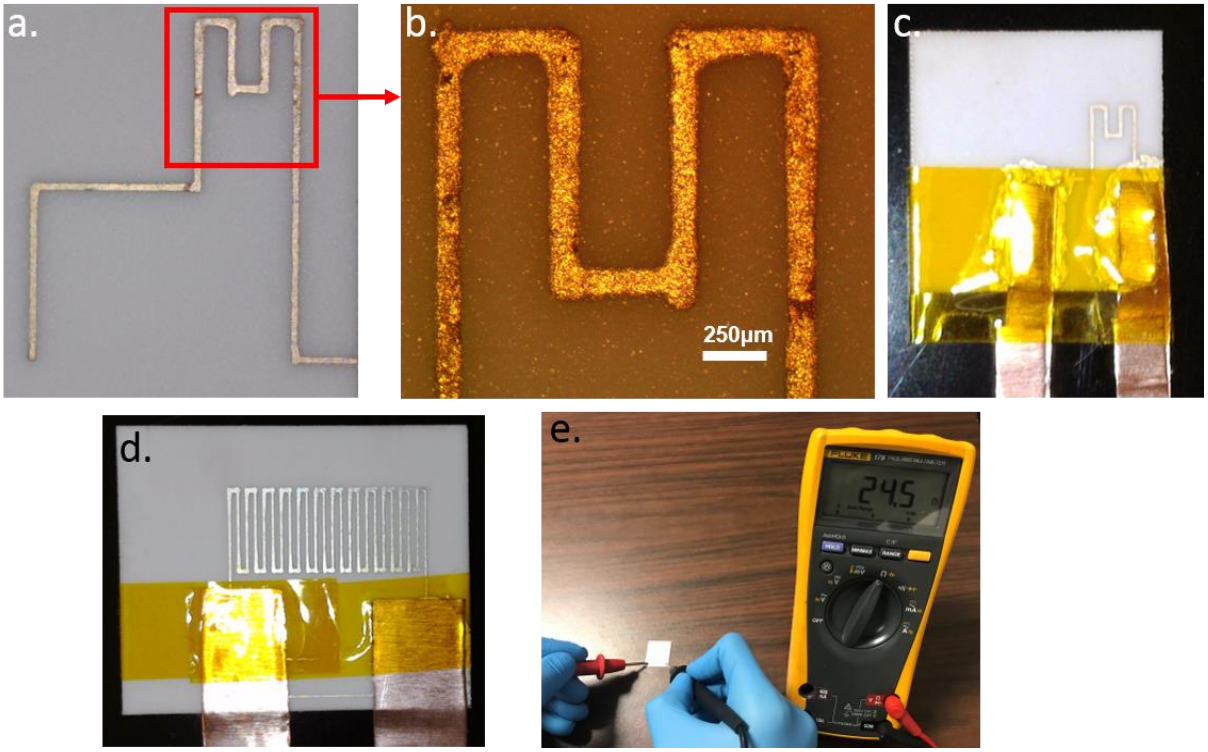

Figure B.1: Fabricated Ag microheater. (a) Photomicrograph of first-generation Ag resister filament on alumina substrate, (b) Optical micrograph of (a), (c) Completed first-generation heater, (d) Completed second-generation heater, with electrical connections accomplished with copper electrode and Kapton tape, (e) Measured resistance of second-generation heater at room temperature.

B.3 Results and Discussion

The printed heater and method of electrical connection are documented in Figure B1. Two different generations of the heater were printed. The first generation (Figure B1a) had an effective heating area of 1500 μm x 1500 μm, and an average filament width of ~110 μm. The initial resistance of first-generation heaters, measured at room temperature with a digital multimeter (Fluke 199 True RMS Digital multimeter) ranged from 1 - 1.6 Ω. This low electrical resistance resulted in high power consumption (e.g., 62.5 W at 10 V), which defeated one of the main advantages of microheater, low power consumption. For this reason, a second-generation heater was printed, as shown in Figure B1. This set of heaters had resistance ranging from 23 -26Ω (Figure B1d) but covering larger area (11.5 mm x 5 mm).

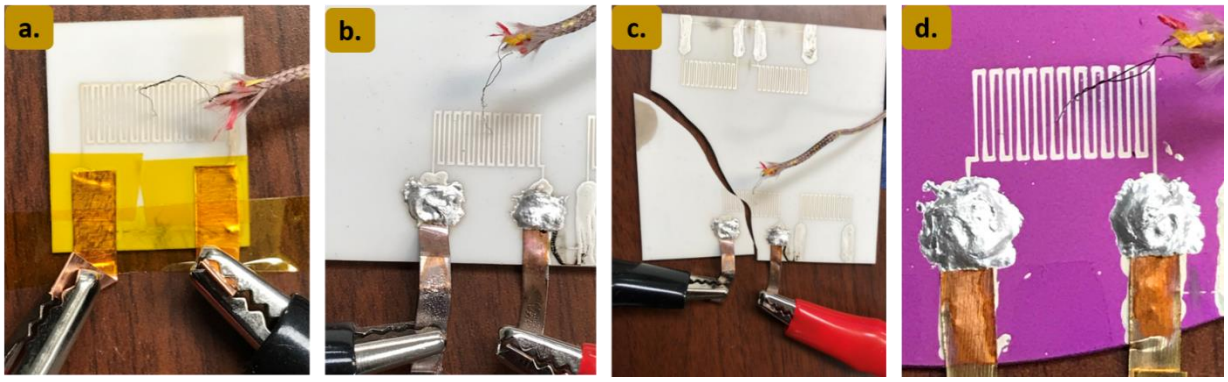

Figure B.2: Experimental setup for testing of the second-generation heaters. (a) Heater on alumina substrate with electrical connection accomplished with a Kapton tape, (b) Heater on alumina substrate with electrical connection accomplished with a silver epoxy, (c) Cracking of alumina substrate due to thermal shock, (d) Heater printed on a silicon substrate with electrical connection accomplished with a silver epoxy.

To determine the thermal characteristics of the heaters, electrical power input was supplied by a variable linear DC supply (Tekpower, TP3005T). In order to study the relationship between the power input and temperature of the microheater, two methods were employed to measure the surface temperature of the microheater, a K-type thermocouple and thermal camera (FLIR T300, FLIR, USA). The experimental setup for the test is depicted in Figure B2. In the first method, the

temperature at the center of the heater was measured using a K-type thermocouple (with a tip diameter ~200 μm), mechanically pressed against the surface of the substrate. In the second method, the thermal camera was place right over the center of the microheater. The thermal characteristics of the heater, presented in Figure B3, was determined by measuring the temperature at different values of the power input. In this test, the heater was turned on for ~60 seconds to give enough time for the temperature to equilibrate. As revealed in the figure, the average maximum temperature of 185^{o}C was achieved at a power of ~6.5 W. We compared the temperature measured by the two methods and it appears the temperature from the IR camera was generally higher than that of the thermocouple. This difference may be explained as follows. For example, the time response of the thermocouple is affected by several factors including its diameter, requiring several seconds to read the equilibrium temperature of the heater. Furthermore, thermal losses through radiation and conduction through the probe is another plausible explanation for the lower readings from the thermocouple [6, 7].

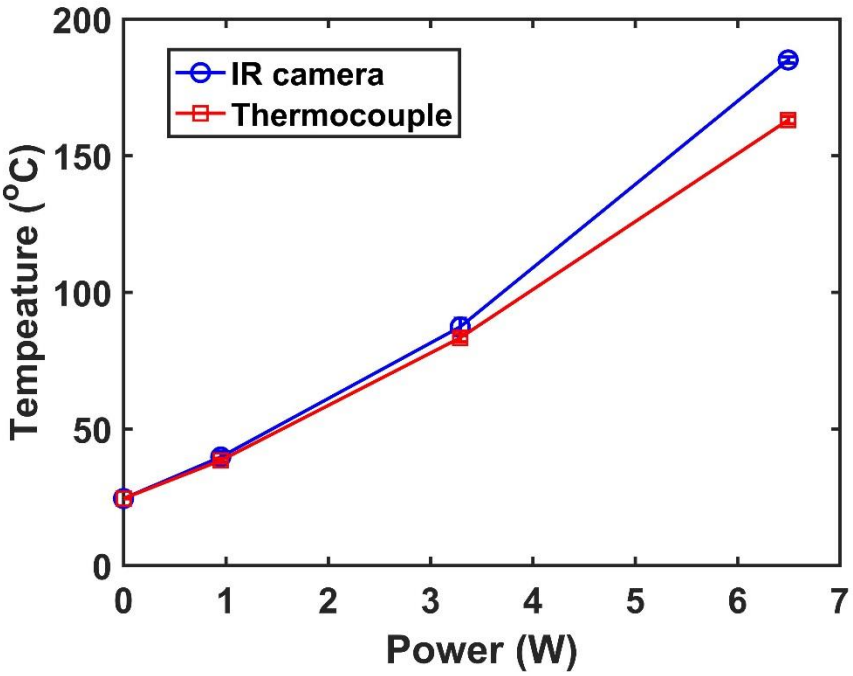

Figure B.3: Temperature of the Ag microheater as a function of input power

On the other hand, for the IR camera, uncertainty in determining emissivity of the surface and its variation with temperature, as well as focusing distance are some factors that may explain the sharp differences at higher temperature, particularly as the temperature of the heater increased [8]. In addition, electrical contacts between the copper electrodes and resistive filament was lost during heating. We realized this happened because of the loss of the adhesive material on the Kapton tape due to heating effect (Figure B2a). To overcome this challenge, we used silver epoxy as an alternative material for bonding the electrode and resistive filament as shown in Figure B2b.

The goal was to test the heater until failure in order to determine its operating limits, however, this was not possible due to thermal cracking of the of the alumina substrate (Figure B2b). Failure of alumina substrate at heating temperatures over 400^{o}C have previously been reported in the literature due to thermal shock[9], and thermal stress arising from a mismatch in coefficient of thermal expansion between the filament the substrate [8, 10]. In the present case, the observed failure is likely due to thermal shock resulting from the sudden temperature changes. To investigate other avenues for testing the operating limits, the microheater was printed on a silicon substrate (Figure B2d). A similar test procedure, as previously described was followed in testing the heater. The applied voltage was only limited by the dc power source and ranged from 0-25 V, equivalent to a power of ~1-15.6 W. While no failure of any kind was observed in this set of heaters, more power was required to achieve a given temperature compared to those printed on alumina substrate. This difference may be explained in terms of the differences in the thermal conductivities of the both substrates. In general, a substrate with moderate thermal conductivity is desired for temperature uniformity of the microheater. A high temperature thermal conductivity leads to high power consumption, and heat loss. For example, silicon has a thermal conductivity of 130 W/m*K compared to alumina with 25 W/m*K. In addition, the silicon substrate had a

much larger area (with a diameter 100mm) compared the alumina substrate (20mm x 20mm). This value indicates heat is lost through silicon substrate at a faster rate than in alumina.

B.4 References

[1] Li, J., Liang, J., Jian, X., 2014, "A Flexible and Transparent Thin Film Heater Based on a Silver Nanowire/Heat-Resistant Polymer Composite," Macromolecular Materials and Engineering, 299(11) pp. 1403-1409.

[2] Celle, C., Mayousse, C., Moreau, E., 2012, "Highly Flexible Transparent Film Heaters Based on Random Networks of Silver Nanowires," Nano Research, 5(6) pp. 427-433.

[3] Liu, L., Niu, X., Wen, W., 2006, "Microheaters Fabricated from a Conducting Composite," Applied Physics Letters, 89(22) pp. 223521-223521-3.

[4] Wu, J., Cao, W., Wen, W., 2009, "Polydimethylsiloxane Microfluidic Chip with Integrated Microheater and Thermal Sensor," Biomicrofluidics, 3(1) pp. 012005-012005-7.

[5] Novacentrix, 2017, "PFI-600 Conductive Flexo Ink, [Online]'. Available: Https://Store.Novacentrix.Com/Product-P/Pfi.Htm. [Accesed 18 January 2019]".

[6] Omega, 2019, ""Fine Gage Bare Wire Thermocouple Elements", [Online]. Available: Https://Www.Omega.Com/Pptst/IRCO_CHAL_P13R_P10R.Html. [Accessed 21 January 2019]".

[7] VanHorn, A., and Zhou, W., 2016, "Design and Optimization of a High Temperature Microheater for Inkjet Deposition," International Journal of Advanced Manufacturing Technology, 86(9-12) pp. 3101-3111.

[8] Tong, T., Li, J., Chen, Q., 2004, "Ultrafast Laser Micromachining of Thermal Sprayed Coatings for Microheaters: Design, Fabrication and Characterization," Sensors & Actuators: A.Physical, 114(1) pp. 102-111.

[9] Prudenziati, M., and Hormadaly, J., 2012, "Printed Films: Materials Science and Applications in Sensors, Electronics and Photonics," NewsRX LLC, pp. 290.

[10] Cai, Z. X., Zeng, X. Y., and Duan, J., 2011, "Fabrication of Platinum Microheater on Alumina Substrate by Micro-Pen and Laser Sintering," Thin Solid Films, 519(11) pp. 3893-3896.

CHAPTER 6

CONCLUSIONS AND OUTLOOK

In this chapter, the major findings of this work are summarized and some possible directions for future research are offered.

6.1 Conclusions

This PhD dissertation chronicles research efforts aimed at advancing the fundamental understanding of microextrusion 3D printing, and its adoption as a cost-effective method for creating customizable microscale devices and structures. As the market for customizable microscale devices increases, microextrusion 3D printing promises a simple and low-cost route for rapid prototyping and fabrication. The significant contributions of this research fall under three categories: development of the underlying understanding of microextrusion 3D printing, design and development of a manufacturing system, and applications showcasing the viability of this approach, and are discussed below.

6.1.1 Development of the Underlying Understanding of μEP

This research established a guiding framework for successful microextruion 3D printing. While there are numerous literatures on the subject, the approach employed here is unique in that, it provides a systematic roadmap to guide users for successful microextrusion 3D printing. It further streamlines the critical processing parameters and metrics that should be considered for successful printing. The developed framework serves as a quick and reliable way of predicting desired output parameters from input variables, and if the desired feature output is possible given a set of printing condition.

The broader impact of this contribution to the society lies in the fact the developed framework provides a theoretical foundation for the extrusion-based manufacturing process at microscale. Industrial utilization of this knowledge may expand the range of 3D printable devices, and potentially enable low-cost customer-oriented product designs ranging from microelectronics, microfluidics, and optical devices.

6.1.2 Manufacturing System Development

Two approaches of extrusion-based printing were demonstrated in this work. First, the microextrusion printhead presented in Chapter 2 depends on a chemical change to accomplish solidification of liquid ink upon extrusion. As a room temperature process, solidification is routinely achieved through reaction with air or addition of curing agents. This method permits the use of a wide range of material that could be prepared in a liquid form. Second, the gel extrusion printhead (Chapter 4) relies on temperature to control material and flow properties in the molten state. This method is common with the fused deposition modelling (FDM) printers, in which the material hardens immediately after being extruded through the nozzle and bonds to the preceding layer to create 3D structures.

With the objective of being economically efficient, these systems show how a high-resolution microextrusion printer can be developed from commercially available components and applied for microfabrication processes. Given suitable materials and design inputs, these printing platforms were utilized to create structural, electronic and optical devices. For instance, the gel extrusion printhead provides an inexpensive system for printing ballistics gel for the first time. In addition to printing Clear Ballistic gel, it can theoretically enable the printing of other material that can be melted into liquid form at a relatively low temperature such as chocolate, wax, etc. Compared to the traditional molding of the gel, this printing method enables complex models to be made at low

cost, fast turnaround time, and in a simple step. Being able to 3D print ballistics gel will provide a significant boost for its applications in its traditional ballistics market, the new medical market (e.g., for pre-surgical planning, medical education, medical equipment testing, etc.), 3D printing materials market for its capability to provide unparallel flexibility to existing flexible 3D printing materials, and potential optics market as revealed in this work.

6.1.3 Applications

Guided by the developed framework and the enabling printing systems, several novel applications were demonstrated including 2D and 3D structures, microheater, and optical devices. These are divided into three areas and are summarized below.

1. Printing of PDMS

The optical transparency, biocompatibility, and low Young's modulus of Polydimethylsiloxane (PDMS) has made it the choice material for creating microfluidic, optical and biocompatible devices. This has led to increased demand for high-resolution, and low-cost patterning methods for fabricating PDMS based structures. In Chapter 2, it was demonstrated for the first time, high-resolution 3D printing of PDMS features in ambient condition with resolution down to ~10μm (compared to 250 μm which is routinely achieved using commercial printers). To achieve this, an empirical model to predict viscosity-time relationship was developed and used to adjust the printing process parameters in order to overcome the capillary rise effect and surface wetting issues. While the resolution is much lower than that reported for soft lithography, this printing method provides a cost-effective route for patterning high-resolution PDMS structures.

2. Printed Optics Using a Soft and Stretchable Material

This research recorded the development of 3D printing of ballistic gel for the first time. The mechanical and optical properties of this soft and stretchable polymer gel were investigated, and by combining the advantages of μEP, we reported a new method for 3D printed optics using a flexible thermoplastic polymer. The rheological properties and printing parameters were optimized to determine appropriate printing conditions for repeatable and high-quality features. Unlike existing methods for fabricating optical devices with rigid glass or polymers, this method enables direct 3D printing of soft and stretchable optical devices at low cost. The printed waveguides show outstanding optical transparency (>98%), very good surface finish, and low transmission losses (~0.22 $dBcm^{-1}$). In addition to the optical performance, we demonstrated direct printing in the open air, in contrast to existing methods of printing optics that requires either carefully-designed support materials during the printing process or extreme post-processing conditions, of soft and stretchable optics (with a ultimate strain of 238.92% and elastic strain of over 100%) in both 2D and 3D with a printing resolution of ~150 μm, which makes this approach very appealing for a wide variety of applications. The easiness in developing successful optical applications in short time at low cost with our approach offers new opportunities of creating integrated optical circuits, complex optical devices, and other innovative optical applications that were not possible before, which will potentially have a significant impact to the optical industry.

3. High Temperature Microheater Fabrication

Chapter 5 explored the feasibility of using μEP and $MoSi_2$ as a simple and cost-effective strategy for making a high temperature microheater. To our knowledge, this is the first reported effort towards making a microheater using $MoSi_2$ with microextrusion 3D printing. We evaluated the suitability of $MoSi_2$ as a functional material for high temperature microheater, to be used in

high temperature sintering of materials. The results were encouraging, with respect to $MoSi_2$ properties, ink formulation and printing, substrate compatibility, sintering, and testing of the microheater, as verified by the printed microheater prototype. While the performance of the heater was not characterized at this time, mainly due to the limitation in available resources, significant progress was made towards the realization of our goal of printing a functional high temperature microheater. The primary findings can be summarized as follows.

1). Molybdenum disilicide is an appealing material with stable heating temperature up to 1000^{o}C which makes it suitable for high-temperature microheaters.

2). A protocol for formulating aqueous MoSi suspension and microextrusion printing of $MoSi_2$ microheater was successfully demonstrated. While the reported print resolution was about 200 μm, in the future it can be improved by using powder with nanoparticle size.

3). Although during sintering, $MoSi_2$ suffered from accelerated deterioration at a temperature ranging from 370-700^{o}C in air due to the pesting phenomenon, this can be easily prevented by sintering in a vacuum or non-oxidizing atmosphere.

4). Alumina was identified as a compatible substrate for fabricating the microheater because of its good adhesion properties and chemical inertness to $MoSi_2$. Yet, it suffers from thermal cracking due to inherent brittleness and thermal stress, but this can be overcome by using composite alumina substrate. Silicon nitride is another good alternative but concerns with adhesion prompts the needs for further verification.

6.2 Recommendations for Future Works

The microextrusion 3D printing framework and printing system described in this dissertation has laid the foundation, and provided an attractive pathway exploring new applications. Below, the author has identified many important ideas that are worth considering for future research.

1. Printing of Flexible Polymer Gel

Currently, the proof of concept demonstration of the gel printing was successfully accomplished, and the printing mechanism is working as expected. In the future, improvement and further testing may be needed to optimize the printing process. For example , an adjustment in the slicing software to generate toolpath based on the different temperature and gel property to ensure consistent flow rate, and high-quality printing. Further testing may be necessary to reveal any unnoticed issue and redesign as may be necessary to adapt the printhead to different printing platforms.

Different from optical applications shown in this work, the measured properties of the gel reveal other important areas for exploration. First, the high compliant nature of the gel, and the digital manufacturing tool provides a convenient way for making complex structures to simulate human body for different applications in defense and medical industries. For instance, studies have shown that medical diagnosis, surgical procedures, responses of human organs to mechanical forces to understand the effect of trauma can be effectively evaluated in the presence of patient-specific physical models, and 3D printing is a clinically relevant manufacturing tool for creating them compared with traditional molding [1-3].

A second area for consideration is as a fugitive ink, which serves as a sacrificial material in a 3D structure. Due to the low melting temperature of Clear Ballistic gel (~100 °C), it can be used a sacrificial material in creating microchannels, as it can easily be melted and removed to leave

microchannel in a 3D structure. Such structures can be constructed into a microvascular network inside a 3D matrix structure and used to deliver "nutritional materials", which enables the creation of self-healing materials [4], microfluidic devices [5, 6], and biomedical devices [7-11]. Finally, the excellent optical transparency, and flexibility of the gel, in addition to the printing capability of the system makes it very attractive for fabricating integrated microfluidic devices [12]. To realized active fluid pumping and mixing, mechanical actuation is an important requirement. Therefore, it is beneficial to fabricate these devices using soft materials with relatively low elastic modulus, so that thin deformable diaphragms can be actuated with minimal force inputs.

2. High Temperature Microheater

The proof of concept demonstration of the microheater was shown. The long-term goal of printing a high performance microheater was to incorporate it into the Microheater Array Powder Sintering (MAPS) printer for printing of high temperature material. Some aspects still need to be addressed to make this happen, including optimization of the sintering process, testing and packaging of the microheater. For example, the effects of sintering condition on the properties of the sintered films should be studied to arrive at appropriate properties. Once the heater has been tested, further steps may be required to optimize the heater design for effective and uniform heat transfer. The effects of the different substrates should be quantitively analyzed to identify any form of reactions that may affect the heater performance. There is also a wide-open design space for formulating inks with smaller $MoSi_2$ powder sizes and different solvents and in different proportions to achieve different rheological, adhesion, and electrical properties.

Ultimately, it is hoped that the developed framework, printing systems and the array of applications showcased in this dissertation will spur interests in adapting microextrusion printing for yet to be printed materials and applications.

6.3 References

[1] Intech, 2018, "3D Printing Cardiovascular Anatomy: A Single-Centre Experience. Available: Https://Www.Intechopen.Com/Books/New-Trends-in-3d-Printing/3d-Printing-Cardiovascular-Anatomy-a-Single-Centre-Experience".

[2] Ionita, C. N., Mokin, M., Varble, N., 2014, "Challenges and limitations of patient-specific vascular phantom fabrication using 3D Polyjet printing," Medical Imaging 2014: Biomedical Applications in Molecular, Structural, and Functional Imaging, February 16, 2014 - February 18, Anonymous SPIE, San Diego, CA, United states, 9038, pp. Intrace Medical; Modus Medical Devices Inc.; The Society of Photo-Optical Instrumentation Engineers (SPIE); Ventana Medical Systems Inc.; XIFIN, Inc.

[3] Armillotta, A., Bonhoeffer, P., Dubini, G., 2007, "Use of Rapid Prototyping Models in the Planning of Percutaneous Pulmonary Valved Stent Implantation," Proceedings of the Institution of Mechanical Engineers Part H-Journal of Engineering in Medicine, 221(H4) pp. 407-416.

[4] Hansen, C. J., Wu, W., Toohey, K. S., 2009, "Self-Healing Materials with Interpenetrating wMicrovascular Networks," Advanced Materials, 21(41) pp. 4143-4147.w

[5] Anderson, J. R., Chiu, D. T., Jackman, R. J., 2000, "Fabrication of Topologically Complex Three-Dimensional Microfluidic Systems in PDMS by Rapid Prototyping," Analytical Chemistry, 72(14) pp. 3158-3164.

[6] Ikuta, K., Hirowatari, K., and Ogata, T., 1994, "Three-dimensional micro integrated fluid systems (MIFS) fabricated by stereo lithography," Micro Electromechanical Systems, 1994, MEMS'94, Proceedings, IEEE Workshop on, Anonymous IEEE, pp. 1-6.

[7] Dario, P., Carrozza, M. C., Benvenuto, A., 2000, "Micro-Systems in Biomedical Applications," Journal of Micromechanics and Microengineering, 10(2) pp. 235.

[8] Ziaie, B., Baldi, A., Lei, M., 2004, "Hard and Soft Micromachining for BioMEMS: Review of Techniques and Examples of Applications in Microfluidics and Drug Delivery," Advanced Drug Delivery Reviews, 56(2) pp. 145-172.

[9] Chou, H. P., Spence, C., Scherer, A., 1999, "A Microfabricated Device for Sizing and Sorting DNA Molecules," Proceedings of the National Academy of Sciences of the United States of America, 96(1) pp. 11-13.

[10] Strömberg, A., Karlsson, A., Ryttsén, F., 2001, "Microfluidic Device for Combinatorial Fusion of Liposomes and Cells," Analytical Chemistry, 73(1) pp. 126-130.

[11] Massa, S., Sakr, M. A., Seo, J., 2017, "Bioprinted 3D Vascularized Tissue Model for Drug Toxicity Analysis," Biomicrofluidics, 11(4) pp. 044109.

[12] Wang, J., McMullen, C., Yao, P., 2017, "3D-Printed Peristaltic Microfluidic Systems Fabricated from Thermoplastic Elastomer," Microfluidics and Nanofluidics, 21(6) pp. 1.